Propagation of Molecular Outflows Into Inhomogeneous Media.

Seán Corkery

B.Sc.

A thesis submitted to

Dublin City University

for the degree of

Master of Philosophy

Thesis Supervisor:

Dr. Turlough Downes

School of Mathematical Sciences

Dublin City University

July 2008

Declaration

I hereby certify that this material, which I now submit for assessment on the programme of study leading to the award of *Master of Philosophy* is entirely my own work, that I have exercised reasonable care to ensure that the work is original, and does not to the best of my knowledge breach any law of copyright, and has not been taken from the work of others save and to the extent that such work has been cited and acknowledged within the text of my work.

Signed: _____

ID Number: 99453444

Date: 21 July 2008

Acknowledgements

There are numerous people I would like to thank for helping me to complete this work. Each helped in their own way and as such deserve special praise.

First and foremost I would like to thank my supervisor, Dr. Turlough Downes, whose support never wavered and who provided the scientific guidance, insight and enthusiasm that made it possible for this work to come to fruition.

I am indebted to all those who took an interest in this material. Those who, when I found myself challenged with particular questions, were there to give me some of their valuable time in order to discuss these difficulties. I am particularily grateful to the following people for their helpful comments and suggestions: Dr. Chris Davis from the Joint Astronomy Centre, Hawaii; Professor Tom Ray from the School of Cosmic Physics, DIAS, Dublin; and Dr. Sylvie Cabrit from l'Observatoire de Paris.

Thanks also to the entire School of Maths in DCU especially Huizhong and her friend for help with the printing, to IRCSET (Irish Research Council for Science, Engineering and Technology) for awarding me a scholarship, to the CosmoGrid project who provided the valuable cpu-time necessary for the simulations carried out in this work and partly funded this work, to ICHEC (Irish Centre for High-End Computing) who also provided cpu-time, to the JETSET Network for organising informative conferences and to the NCPST, Natinal Centre for Plasma Science and Technology.

A very special thanks to my girlfriend, Anne-Sophie, who got me through the worst days and provided invaluable emotional support and motivation. It wouldn't have happened without you. Merci beaucoup ma petite poule!

Many thanks also to my family and friends, in DCU and elsewhere for helping to keep me sane. Especially my mother, Noelle Corkery, who has provided a lot of support and patience over the years.

Finally, this thesis is dedicated to the memory of my father, James Corkery.

Contents

Abstract

Molecular clouds have inhomogeneous density profiles and have been observed to be 'clumpy' in nature, containing dense cores, rarefied filaments and cocoons. Energetic mass-ejection phenomena created during the gravitational collapse of dense cores are thought to be responsible for the molecular outflows that are observed in molecular clouds. Interactions between these molecular outflows and the inhomogeneous molecular clouds they encounter may cause changes in the observable characteristics of the outflows by affecting their velocity structure and morphology.

Consequently, in this work, we aim to gain an understanding of the consequences of a relaxation of the usual assumption of a homogeneous molecular cloud or ambient medium, that is normally made in numerical simulations of molecular outflows. In particular, we simulate outflows propagating into inhomogeneous molecular clouds of decreasing density, i.e. outflows in the process of leaving their parent molecular clouds. We would expect such flows to appear severely truncated in CO emission maps, in comparison to their full flow extents.

Using various prescriptions for inhomogeneous media to create more realistic density profiles, long duration numerical simulations are run. The simulations include the use of an improved cooling function the effects of which we describe. Standard observational methods are used for inferring the average outflow velocity and outflow age from the simulations. We examine the effects of the different density profiles on these key parameters and on the density structure, mass-velocity relations and length-to-width ratios that characterise the outflows.

List of Figures

List of Tables

Chapter 1

Introduction

Stars form inside relatively dense concentrations of interstellar gas and dust known as molecular clouds. The closest region of massive star formation to Earth is the Orion Nebula, shown in great detail in Figure 1.1, which is even visible to the naked eye in the night sky. This nebula or molecular cloud is generally credited as being first discovered by Nicolas-Claude Fabri de Peiresc as far back as 1610. Since then large numbers of molecular clouds have been found, William Herschel published a catalogue containing 1000 nebulae, in Herschel (1786), the observations for which were begun in 1783 with the help of his sister Caroline. This was the first in a series of three catalogues that in total contained 2500 nebulous objects. While many of the nebulae discovered by the Herschels turned out to be planetary nebulae and galaxies, some were found to be star formation regions or stellar clusters. Some nebulae are so dense that they obscure the light from stars and reflection nebula emitting in the background, and can be seen as dark patches on the sky. This extinction of light is caused by dust grains located in the densest parts of the molecular clouds and also by molecules and atoms.

Molecular clouds range in size from isolated globules, perhaps a parsec across, up to giant molecular clouds several tens of parsecs across. Isolated small dark nebulae are called Bok globules. Bok globules bear the name of the astronomer, Bart Bok, who observed these small dark clouds in the 1940s, near HII regions and published his findings in Bok & Reilly (1947). In their paper Bok and Reilly refer to work by Whipple (1946) in which a process is suggested "for the origin of stars by the

Figure 1.1: The Orion Nebula in visible light captured by the Hubble Space Telescope (HST). (Credit: M. Robberto (STScI/ESA), the HST Team, and NASA/ESA)

concentration of interstellar dust particles". Whipple's work was heavily based on studies of the dynamics of the interstellar medium in gravitational systems carried out by Spitzer (1941). Bok and Reilly theorised that the globules they observed were collapsing to form stars and thus their work has formed part of the basis upon which our current understanding has been built.

1.1 Molecular Clouds

Molecular clouds are typically found in the spiral arm segments of galaxies although small molecular clouds can be found outside these regions. These spiral arm segments can have sizes of up to several tens of parsecs across and masses, if only inter stellar material is counted, of up to 10^7 solar masses, $M_\odot$. They can contain numerous giant molecular clouds with sizes and masses of up to 100 parsecs and $10^6 M_\odot$ respectively (Sanders et al., 1985), which in turn can contain much smaller scale structures. The structure of these clouds has been observed to be 'clumpy' in nature containing dense cores and rarefied filaments and cocoons that form an almost hierarchical arrangement of smaller scale structures contained within larger ones (Myers et al., 1978). There are some obvious exceptions to this rule, for example the Bok globules discussed above show that small dense cores can exist in isolation. This self-similarity of molecular clouds suggests a fractal structure which is thought to be caused by turbulence in the clouds. Falgarone et al. (1991) found evidence for this fractal structure on all scales down to an angular resolution of 0.02 pc using their observations of molecular clouds in several transitions of carbon monoxide (CO).

Turbulence is characterised by chaotic changes in a fluid's properties including momentum, pressure and velocity which appear to occur randomly. Chaotic changes in velocity have been found in molecular clouds on a variety of different scales via measurements of velocity dispersion inferred from line width increases (Crutcher et al., 1978). The velocities are found to be supersonic in all but the smallest regions, with velocity increasing along with region size in a manner resembling the Kolmogoroff law (Larson, 1981). The Kolmogoroff law predicts a "cascade" of en-

ergy from large scale structures to smaller scale structures. It predicts this process to continue, creating smaller and smaller structure, until eventually structures are created that are small enough for molecular diffusion to become important and viscous dissipation of energy finally takes place. The scale at which this happens is called the Kolmogorov length scale. Supersonic motions can generate shocks that produce large density fluctuations and in particular Elmegreen (1993) discussed the possibility of ram pressure from supersonic turbulence producing regions or layers of compressed gas on several different scales and studied the possibility of gravitational-instabilities causing these regions to collapse into dense cores.

While the term "molecular cloud" originates from the fact that such clouds were originally discovered mainly through their CO and NH_3 emission, these regions are mostly made up of molecular hydrogen. These clouds are also surrounded by less dense regions of atomic gas. They are extremely cold, as long as they remain optically thin to thermal emission from CO, with temperatures in the range of between about 6 K and 12 K. Once a cloud is optically thin, below a number density of approximately $2 \times 10^{10}\,\mathrm{cm}^{-3}$, the densest regions will generally be the coldest (Larson, 1973). There are two main reasons why the densest regions are colder. The first reason arises from the fact that the dust and gas absorbs the radiation from nearby heat sources. Due to this absorption the innermost components of a dense molecular cloud are shielded from a certain amount of ultraviolet radiation and hence achieve lower temperatures. The second reason for lower temperatures is a higher rate of thermal emission and hence cooling. The atoms, molecules and dust collide more often in dense regions and therefore emit more photons, thereby increasing the rate of cooling. See Section 2.5.1 for more details on molecular cooling.

Self-gravity becomes important at these low temperatures and relatively high densities. It is thought that, on large scales in molecular clouds, self-gravity is counteracted by the supersonic turbulence discussed above and also by magnetic fields but that at smaller scales thermal pressure becomes the decisive force counteracting self-gravity. At these smaller scales in regions of low temperature and therefore low thermal pressure, and assuming that self-gravity dominates the other forces, the

Jeans instability (Jeans, 1902, 1928; Hoyle, 1953) will cause the collapse of a cloud clump since the internal gas pressure is not strong enough to prevent gravitational collapse. For an isothermal cloud with a uniform density, ρ, and a constant temperature, T, the Jeans length, R_J, is the critical cloud radius at which the thermal energy per particle equals the gravitational work per particle and can be expressed as

$$R_J \simeq c_s \sqrt{\frac{15}{4\pi G\rho}} \tag{1.1}$$

where

$$c_s = \sqrt{\frac{k_B T}{\mu}} \tag{1.2}$$

is the isothermal sound speed, G is the gravitational constant, μ is the average mass per particle and k_B is Boltzmann's constant. At this critical length the cloud neither expands nor contracts but when the cloud's radius is larger than this critical length gravity dominates the thermal pressure and the cloud collapses.

The Jeans criterion can also be expressed in terms of a critical mass above which the cloud will collapse. This mass is called the Jeans mass, M_J, and can be expressed as

$$M_J \simeq c_s^3 \left(\frac{5}{G}\right)^{3/2} \left(\frac{3}{4\pi\rho}\right)^{1/2}. \tag{1.3}$$

As discussed above, in regions with number densities of below about $2 \times 10^{10}\,\mathrm{cm}^{-3}$ the cloud will remain optically thin and the assumption of a constant temperature of approximately 10 K is reasonable.

On the other hand the assumption of constant density is not so reasonable. A more realistic approach is to consider a sphere in hydrostatic equilibrium that is surrounded and confined by a pressurised external medium. Such a sphere is called a Bonnor-Ebert sphere (Bonnor, 1956; Ebert, 1957). In a Bonnor-Ebert sphere the density decreases with distance from the central source according to the following formula, $\rho \propto r^{-2}$, where r is the distance from the source. This results in a more

reasonable density profile that has equal masses in shells of equal thickness, which is consistent with observations of the envelopes that surround protostars. Ladd et al. (1991) observed these envelopes to be highly centrally concentrated, with radial density profiles consistent with $\rho \propto r^p$, where p was found to be between -1.5 and -2. In this model, the above density profile arises as a consequence of dense inner regions collapsing faster than the less dense outer regions due to a pressure gradient caused when the interior pressure rises. The critical radius and mass above which an isothermal sphere of this nature will collapse are given by

$$R_{BE} = 0.48\, c_s^2 \sqrt{\frac{1}{GP}}, \tag{1.4}$$

$$M_{BE} = 1.18\, c_s^4 \left(\frac{1}{G}\right)^{3/2} \left(\frac{1}{P}\right)^{1/2}, \tag{1.5}$$

where P is the external pressure (see Larson, 2003). These equations can be compared to the corresponding Jeans Equations (1.1) and (1.3) through the equation of state for an isothermal gas, $P = \rho c_s^2$. One notices that the coefficient for the Bonnor-Ebert critical mass is smaller than the coefficient for the Jeans critical mass. This is as a result of the higher densities in a Bonnor-Ebert sphere. If we assume that the external pressure, acting on a dense clump, is a result of the ram pressure from supersonic turbulence and that the temperature in the clump is 10 K, then the Bonnor-Ebert criterion gives a minimum unstable radius of 0.03 pc and mass of 0.7 $M_\odot$. This is in agreement with the typical observed masses of pre-stellar cloud cores.

Shu et al. (1987) proposed a slower model of collapse in which the cloud core is initially in gravitational equilibrium and supported by a magnetic field. The collapse is slowed because the neutral molecules are collisionally coupled to the plasma which is in turn tied to the magnetic field and therefore resists collapse. Unlike the previous model collapse begins in the centre and travels outward.

In either case, star formation begins when the gases combine together into molecules and dust and form clumps of high density which begin to collapse under their own gravity. Cooling by thermal emission from CO keeps the temperature

close to 10 K while the density increases by many orders of magnitude. So, the dense clumps can contain smaller, even higher density, self-gravitating cloud cores which in turn collapse under gravity. This runaway collapse forms a central density peak in which a protostar or even systems of multiple protostars are predicted to form. Each protostar has a very small initial mass predicted to be less than 0.01 $M_{\odot}$.

Only a small fraction of the mass of a collapsing cloud core attains densities high enough to form a star. The rest of the material remains behind in an extended infalling cloud, or envelope as it's sometimes called. In the presence of rotation or magnetic fields, the innermost part of the envelope may become strongly flattened forming a massive, opaque, circumstellar disk that surrounds the forming star. The disk continues to grow in mass by accumulating material from the surrounding envelope. This disk gradually transfers mass onto the stellar surface in a process called accretion. Eventually the central region becomes dense enough so as to be opaque to thermal emission from CO and other species, at a density of about $10^{-13}\,\mathrm{g\,cm^{-3}}$. When this occurs it's temperature begins to rise quickly and when the density reaches around $10^{-12}\,\mathrm{g\,cm^{-3}}$ the gas becomes completely adiabatically insulated to heat transfer. The increased thermal pressure begins to slow the collapse until eventually it totally counteracts gravity and resists further collapse. This occurs at a density of approximately $2 \times 10^{-10}\,\mathrm{g\,cm^{-3}}$ and a hydrostatic core forms which is almost in hydrostatic equilibrium and has a mass of less than 0.01 $M_{\odot}$.

This first hydrostatic core phase doesn't last very long and a second phase of collapse begins when the temperature at the centre rises above 2000 K. At this temperature hydrogen molecules begin to be dissociated and the value of the heat capacity ratio, γ, is reduced. This causes the core to become unstable again and it continues to collapse until the hydrogen at the centre becomes ionised and the value of γ rises above it's critical stability value again. A second even smaller hydrostatic core is formed which continues to accrete material from the surrounding envelope.

When an accreting protostar reaches a mass of about 0.2 $M_{\odot}$, deuterium burning begins which increases the temperature further and causes the protostar to expand

in radius to about 4 $R_{\odot}$ as its mass continues to increase. The accretion rate is predicted to be initially very high but to decrease rapidly as the infalling envelope is accreted. When the accretion rate becomes negligible the star becomes visible as a T-Tauri star.

Associated with the early stages of star formation is an energetic mass-ejection phenomenon. This mass-ejection phenomenon is thought to be responsible for the molecular outflows that are observed in molecular clouds. A fraction of the material accreted onto the star is ejected along the axis of rotation and perpendicular to the disk plane in a highly collimated stellar jet. Since the early stages of star formation are heavily obscured deep within cloud cores, these highly collimated jets may be the first sign that an accreting protostar is forming. The material accreting onto the young stellar object (YSO), from the circumstellar disk surrounding it, requires angular momentum to be removed or transported outward. It is believed that these jets act to drain away this excess angular momentum. Another important point of note is that magnetic fields may be involved in both the accretion phase of YSOs and in the launching of these bipolar jets (see Section 1.9) as well as their collimation.

1.2 Herbig-Haro Objects

The discovery of molecular outflows dates back to the independent discovery of Herbig-Haro objects by Herbig (1951) and Haro (1952), hereafter referred to as HH objects. Herbig found "several peculiar nebulous object" one of which "resembles a slightly diffuse star with a very short, curved, nebulous tail". In the spectra the strongest emission observed was in the lines of Hα at λ=6562 and in the low-excitation lines of [OI] at λ=6300, 6363 and [SII] at λ=6717, 6731 (all wavelength are given in ångströms, Å, unless otherwise stated). The spectra were noted as being odd for several reasons, firstly because of the great strength of the [SII] emission, secondly because of the large range in the excitation energy between the different lines that were observed and thirdly because the spectra didn't resemble the spectra of T-Tauri stars in the same dark nebula. Haro (1952) noted that these objects weren't visible in infrared light and that "if any star is associated with these nebulous objects, it

must be a faint, very blue, hot star". So although both authors linked their finds to stars they suspected that this wasn't the full story.

Ambartsumian (1957) gave Herbig-Haro objects their name and, based on their occurrence near T-Tauri stars, suggested that they might represent an early stage in the formation of T-Tauri stars. Osterbrock (1958) compared their emission with the emission from around T-Tauri, the prototypical T-Tauri star, He suggested that T-Tauri "is losing mass because of it's rotation, and that at least some of this mass is streaming out with velocities larger than $100\,\mathrm{km\,s^{-1}}$" and also suggested that this mass loss mechanism was responsible for the observed ionisation around HH objects. An important breakthrough occurred when Schwartz (1975) suggested that radiating shocks may form where supersonic mass outflow interfaced with the interstellar medium and compared the emission spectra to those predicted by the shock-wave models of Cox (1972). The spectra from these models had already been compared to those of a supernova remnant and were based on calculations that took into account the emission from the cooling of hot gas in the post-shock region. The calculations were done assuming plane-parallel flow.

Subsequently Schwartz (1978) proposed a shocked cloudlet model for HH objects which elaborated upon his previous paper and considered a strong stellar wind that produced shock waves upon interaction with small ambient clouds. This model could not properly explain the well-known variability in the individual objects as described by Herbig (1969, 1973). In order to help explain this variability Boehm (1978) proposed a model of non-stationary shocks, similar to blast waves. Extensive spectrophotometry of HH objects was carried out by Dopita (1978). He found in the case of HH 46/47 that their spectra could only be fitted by low-velocity shocks, a result of the low level of [OIII] emission observed. He concluded "that the shocks in these objects are moving into an inhomogeneous material that was already moving out from the stellar object with appreciable velocity" and suggested that this could be taking place if repeated eruptions were occurring.

A dramatic discovery by Cudworth & Herbig (1979) was that HH 28/29 were observed to have very large proper motions of around $145\,\mathrm{km\,s^{-1}}$. Cudworth &

Herbig (1979); Herbig & Jones (1981) observed similar large proper motions for HH 1 (155-351 $\mathrm{km\,s^{-1}}$) and HH 2 (100-294 $\mathrm{km\,s^{-1}}$) which were in opposite directions to one another and also directed away from the nearby forming star. This established the bipolar nature of some HH objects.

1.3 Molecular Outflows and Jets

CO observations by Snell et al. (1980) revealed the presence of a double-lobed structure in the molecular cloud L1551 with both lobes extending in opposite directions away from an infrared source L1551 IRS 5. This discovery of a bipolar molecular outflow was all the more interesting because one of its lobes was associated with HH 28, HH 29 and HH 102. It was suggested that the CO emission arose from a dense shell of material which had been swept up by a strong stellar wind from the infrared source. This model for the creation of molecular outflows remains, to this day, one of the most popular models, perhaps with the exception of the jet-driven molecular bow shock model (see Section 1.4 below).

One of the earliest uses of the word jet to describe mass outflows from YSOs was by Königl (1982) when he proposed a model to describe how an "outflow becomes channeled into two oppositely directed, supersonic jets" by a medium with an anisotropic density and pressure distribution. The main assumption of a spherically symmetric stellar wind with an anisotropic confining medium was the same as in the model of Barral & Canto (1981) but the interpretation was different, particularly in relation to the origin of HH objects as emission knots in jets. Dopita et al. (1982b) also used this model to describe how "instabilities in the jets or interaction of the jets with ambient cloudlets could hence be implicated with the production of HH nebulae". They also presented the discovery of a new HH object HH 47C in the system HH 46/47 travelling in the opposite direction to the existing object HH 47A which established the HH 46/47 objects as forming parts of a bipolar jet (see Figure 1.2).

Four more HH jets were discovered by Mundt & Fried (1983) who described them as being due to highly collimated mass outflows with small opening angles of

5°-10°. This important paper led people to think that most HH objects were the result of highly collimated jets, and that they traced shocks occurring along the jets. Raga et al. (1990) explained the complex position-velocity diagrams and multiple bow shock structures observed in some stellar jets in terms of a model in which jets are ejected from their sources with variable velocities. According to this model, HH object trace shocks produced when fast moving jet material collides with slower moving jet material (internal working surfaces), and also shocks produced when jets ram into the ambient cloud (terminal working surfaces). Masson & Chernin (1993) proposed that HH jets, in their episodic outbursts, transfer enough momentum to drive molecular outflows and presented a theoretical mechanism for the transfer of momentum from the jet to its ambient medium (see also Raga & Cabrit, 1993).

1.4 Outflow Models

It is still debatable what the mechanism is through which a molecular outflow is produced. Although it is known to involve a jet/wind, originating in the region around a YSO, that accelerates material in the ambient medium, the exact mechanism through which this occurs is still a mystery. Several dynamical models have been proposed to provide a suitable mechanism and to attempt to explain the molecular outflows and their properties. Three of the most popular dynamical models are outlined below. They are the wide-angle-wind model, the turbulent jet model and the bow shock model.

1.4.1 Wide-Angle-Wind Model

In the wide-angle-wind model, a momentum-conserving wide-angle wind is generated from the surface of the circumstellar disk surrounding a YSO and interacts with the ambient medium, sweeping it up into a thin shell (Snell et al., 1980; Shu et al., 1991; Li & Shu, 1996; Lee et al., 2000, 2001). Shu et al. (1991) assumed that the shocked wind and ambient material instantaneously mix inside the shell resulting in the radial expansion of the shell. Higher velocities in more distant parts of the outflow are the result of variations in the density and wind strength with polar angle.

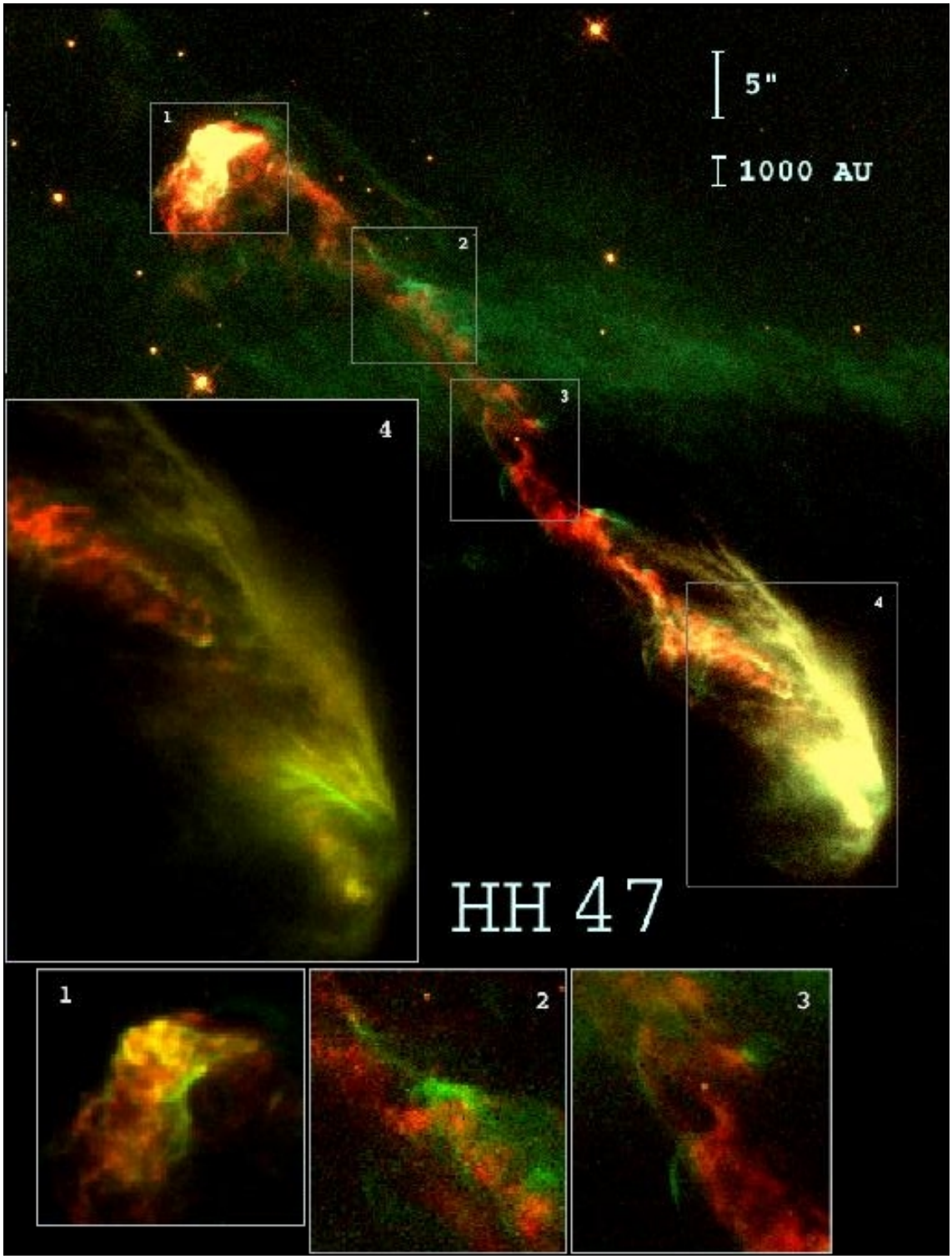

Figure 1.2: Stellar jet system HH 46/47 in which [SII] emission in red comes mainly from the core of the jet while Hα emission in green comes mainly from shocks being driven into the surrounding material. The yellow regions, therefore, denote regions in which both types of emission are present. The insets provide a close up view of a number of specific regions as discussed in Heathcote et al. (1996): (1) the HH 47A working surface; (2) the region near knot A16 located at a substantial bend in the jet; (3) the Hα filaments associated with knots A22 and A26; (4) the base of the jet including HH 46 along with a reflection nebula that has been illuminated by the source. (Credit: Heathcote et al. (1996), the WFPC 2 Team, and NASA/ESA)

The density in the ambient medium varies with distance from the source, r, and is proportional to $1/r^2$. In this model, the molecular outflow corresponds to the swept-up molecular material found in the thin shell. Numerical simulations were carried out by Lee et al. (2001) and were compared to the observational features of several outflows. They concluded that the wide-angle-wind model could best produce the parabolic PV structure seen in some outflows such as VLA 05487, which is not associated with any bow shocks, while the jet-driven bow shock model could best produce the velocity spur structure seen in other outflows such as HH 212. Other examples of outflows that might be explained by the wide-angle-wind model are L1551 (Moriarty-Schieven & Snell, 1988), Mon R2 (Meyers-Rice & Lada, 1991) and L43 (Bence et al., 1998).

1.4.2 Turbulent Jet Model

In the turbulent jet model, Kelvin-Helmholtz instabilities lead to the formation of a turbulent viscous mixing layer along the jet/ambient boundary resulting in the entrainment of ambient molecular material along the sides of the jet/wind (Canto & Raga, 1991; Stahler, 1994; Lizano & Giovanardi, 1995). The turbulent mixing layer grows into both the ambient medium and the jet causing large portions of the flow to become turbulent. Early models were found to produce too narrow a layer and resulted in outflows with length-to-width ratios that were much larger than those observed. Raga et al. (1993) proposed a method that would widen the outflows. In their method, a large number of internal working surfaces or velocity discontinuities intercept material from the jet beam and eject it sideways, due to the pressurised expansion of the jet. Another problem with this model, as pointed out in Arce et al. (2007), is that it produces decreasing molecular outflow momentum and velocity with distance from the powering source, which is in disagreement with one of the main properties of molecular outflows as determined from observations (see Section 1.8).

1.4.3 Bow Shock Model

In the bow shock model, a highly supersonic collimated wind or jet propagates into the ambient medium, forming a bow shock surface at its head (Raga & Cabrit, 1993; Masson & Chernin, 1993; Stone & Norman, 1993a,b, 1994; Chernin et al., 1994; Smith et al., 1997; Downes & Ray, 1999; Lee et al., 2001; Downes & Cabrit, 2003; Keegan & Downes, 2005; Downes & Cabrit, 2007; Arce et al., 2007). The jet carves into the cloud and forms a working surface that consits of two shocks, one in which jet material is decelerated (mach disk) and another in which ambient material is accelerated (bow shock). High pressure gas between the shocks is ejected sideways out of the jet beam, thereby shocking more of the unperturbed ambient gas and sweeping it up. The swept-up ambient gas continues to shock more ambient gas, at an oblique angle, and continues to force material sideways, parallel to the shock surface, thus creating the characteristic bow-shaped surface that is observed. It is this bow shock that produces the molecular outflow around the jet as it moves away from the YSO and sweeps up more and more molecular material.

A low-pressure region called the cocoon is formed between the jet and the bow-shock. Some post-shock gas re-expands into this low-pressure region, thus creating a low-density cocoon of mixed ambient and jet material. Velocity variations in the jet, due to the episodic nature of the outflow at the source, produce shocks or internal working surfaces along the body of the jet (Raga et al., 1990; Cantó et al., 2000). These shocks are thought to be responsible for ejecting material into the surrounding cocoon, through a similar mechanism as the one described above for bow shocks.

Smith et al. (1997) and Suttner et al. (1997) carried out jet simulations that were able to reproduce many of the observational characteristics of molecular outflows, which are outlined in Section 1.8, including the "Hubble law" and strong forward, as opposed to sideways, motion. One of the remaining problems with this model is the difficulty it has in producing the parabolic PV structure seen in some outflows (Lee et al., 2001).

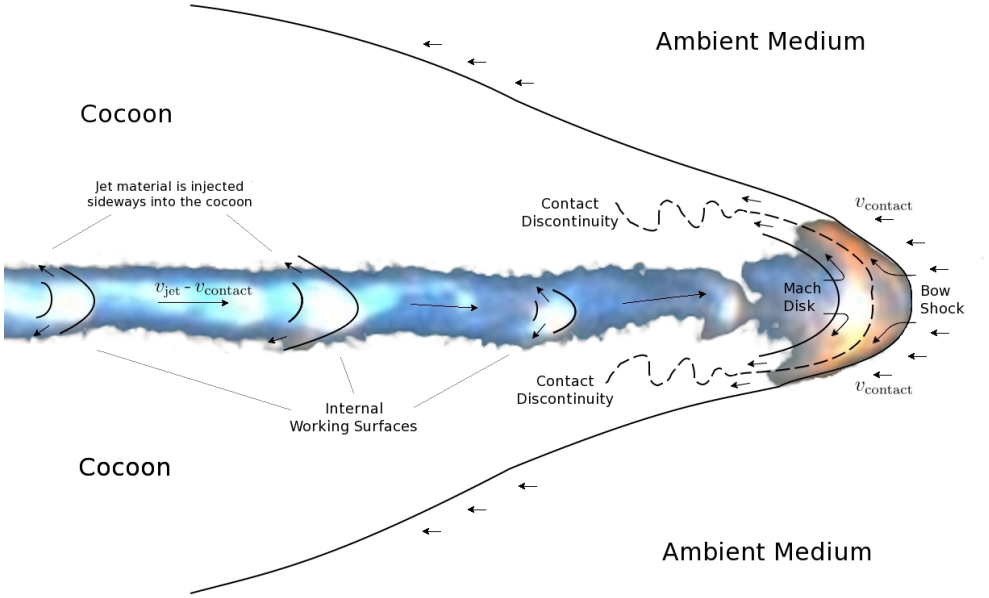

Figure 1.3: Graphical representation of the bow shock model superimposed on observations of HH 111 from Figure 1.6. A well collimated jet forms a bow shock at its head and a low-pressure cocoon is created between the jet and the bow-shock. Internal working surfaces are created by velocity variations in the jet. All velocity arrows are given in the frame of reference of the contact discontinuity.

1.5 Radiative Shocks

Shocks occur when material moves at velocities greater than the local sound speed, i.e. moves faster than information about it can be propagated via sound waves, which means that downstream material cannot react or "get out of the way" before high velocity material arrives. Sound waves travelling against the flow cannot travel upstream and so upstream material cannot respond dynamically to the material it is about to move into until it does so. As a result pressure progressively builds up and a high pressure shock wave rapidly forms, across which there is an almost instantaneous rise in the temperature and density of the flow as well as the pressure. A shock is called "radiative" if it cools due to radiative emission on a timescale that's short when compared with the cooling timescale associated with adiabatic expansion.

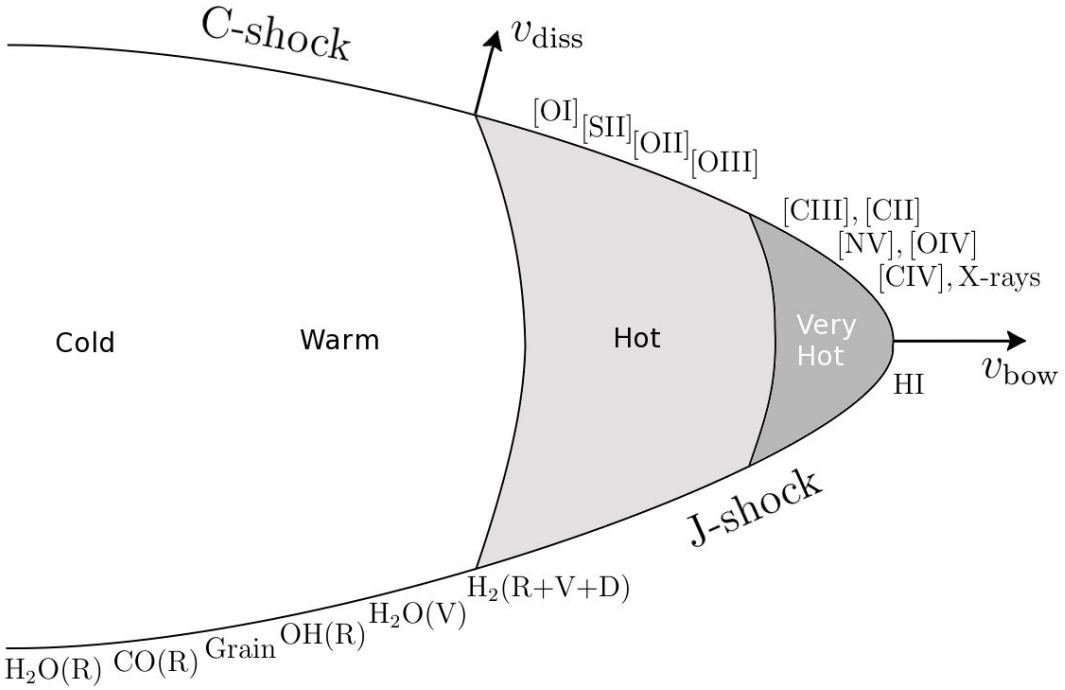

Figure 1.4: The locations of the different cooling zones discussed in the text. R, V and D respectively indicate emission that is associated with the rotation, vibration and dissociation of the above molecules.

1.5.1 J-shocks

In a non-magnetised fluid there is one type of shock that interests us, the jump-shock (J-shock), several properties of which we now outline:

- In a J-shock there is a sudden jump or discontinuity in the temperature, density and velocity.

- The thickness of the shock is very small compared to the hydrodynamical length scales, typically an order of magnitude greater than the mean free path of the gas.

- Within the frame of reference of the shock, material enters the shock at a velocity $v_{\rm shock}$ (or $v_{\rm bow}$ for a bow shock) and with a density n_0. See Figure 1.3 for an illustration showing the velocity structure in the frame of reference of the contact discontinuity. By balancing the flux of momentum, energy and mass across the shock one can define "jump" conditions called the Rankine-Hugoniot jump conditions that relate the pre-shock and post-shock temperature, density

and velocity to each other. For strong, adiabatic, hydrodynamic shocks with heat capacity ratios of $\gamma \simeq 5/3$, the Rankine-Hugoniot jump conditions tell us that the density increases by a factor of 4 across each shock and that the post-shock velocity drops to $v_{\rm shock}/4$, in the reference frame of the shock. Kinetic energy is converted to heat and the temperature in the postshock regions increases dramatically.

- Immediately behind a J-shock, pre-shock gas that was initially in a low ionisation state suddenly enters a very hot environment and its level of ionisation rises rapidly. Some of the neutral hydrogen present will become collisionally excited before it is ionised and so, will subsequently emit Hα emission. It is for this reason that the positions of shock fronts are well detected in Hα emission.

- The fluid does not have enough time to reach collisional ionisation equilibrium (CIE) before radiative losses become important. The gas begins to radiate emission and it gradually cools and recombines, while the density increases.

- If the post-shock gas is hot enough it emits extreme ultraviolet emission (EUV) and sometimes even X-rays. When that gas cools to below approximately $10^4\,$K, it usually becomes opaque to EUV emission and begins to absorb EUV photons from the hotter post-shock gas, thus some of the fluid re-ionises. The stronger the shock the larger the fraction of gas that will become re-ionised.

- When the EUV emission from the hot post-shock gas radiates downstream and emerges from the shock, it ionises the preshock gas ahead of the shock. This is called a radiative precursor (Sutherland et al., 1993). When this ionised pre-shock gas enters the shock, energy that would have gone into ionising the gas now goes into generating heat energy instead, thereby increasing the postshock temperature even further. For shock velocities in excess of $120\,{\rm km\,s^{-1}}$, the hydrogen entering the shock is almost fully ionised.

- The strongest shock velocities occur at the apex of the bow-shock with systematically lower velocities as you move further out along the bow. Behind the fastest shocks ($>300\,{\rm km\,s^{-1}}$), HI emission is followed by the UV emission

Line ratio	HH 47A	HH 47D
[OI](λ=6300)/Hβ	3.2	3
[SII](λ=6717)/Hβ	4.8	8
[OII](λ=3727)/Hβ	0.8	16
[OIII](λ=5007)/Hβ	<0.1	1.8

Table 1.1: Line ratios for HH 47A and HH 47D which are typical low and high excitation HH objects, respectively. The data is from Dopita et al. (1982b).

of species such as [CIV], [NV], [OVI], [CIII] and [CII] and also X-ray emission. As mentioned previously, some of the emission from these species will re-ionise material further upstream. In the meantime radiative emission and cooling continues, and as these species radiate, cool and recombine they are followed by species such as [OIII], [OII], [SII] and [OI] in other well defined cooling zones behind the shock. Lower velocity shocks may only be hot enough to emit via some of the latter species (See Figure 1.4).

- J-shock models predict that molecular hydrogen is dissociated if the shock speed exceeds about $v_{\rm shock} \geqslant 25\,{\rm km\,s^{-1}}$ (McKee & Hollenbach, 1980). This explains the lack of molecular cooling in high velocity shocks.

HH objects correspond to shocked regions and can be classified as low or high excitation, and hence as containing low or high velocity shocks, on the basis of their line ratios. [OIII] lines only occur in shocks with a velocity exceeding $\sim$90 km s^{-1}, so HH objects in which [OIII] emission can be observed are of high excitation and can usually be associated with the "termination" region of a jet. Intermediate excitation (60-90 km s^{-1}) and low excitation (30-60 km s^{-1}) objects can be identified by comparing the ratio of the [OII]/HI emission lines to the ratio of [OI]/HI. Table 1.1 shows various line ratios for HH 47A (low excitation) and HH 47D (high excitation) as taken from Dopita et al. (1982b). The illustration in Figure 1.4 gives an outline of the locations of the different cooling zones discussed above.

1.5.2 C-shocks

In a magnetised fluid, the J-shock scenario still holds when shock velocities are greater than the ion Alfvén velocity. For shock velocities lower than this critical ve-

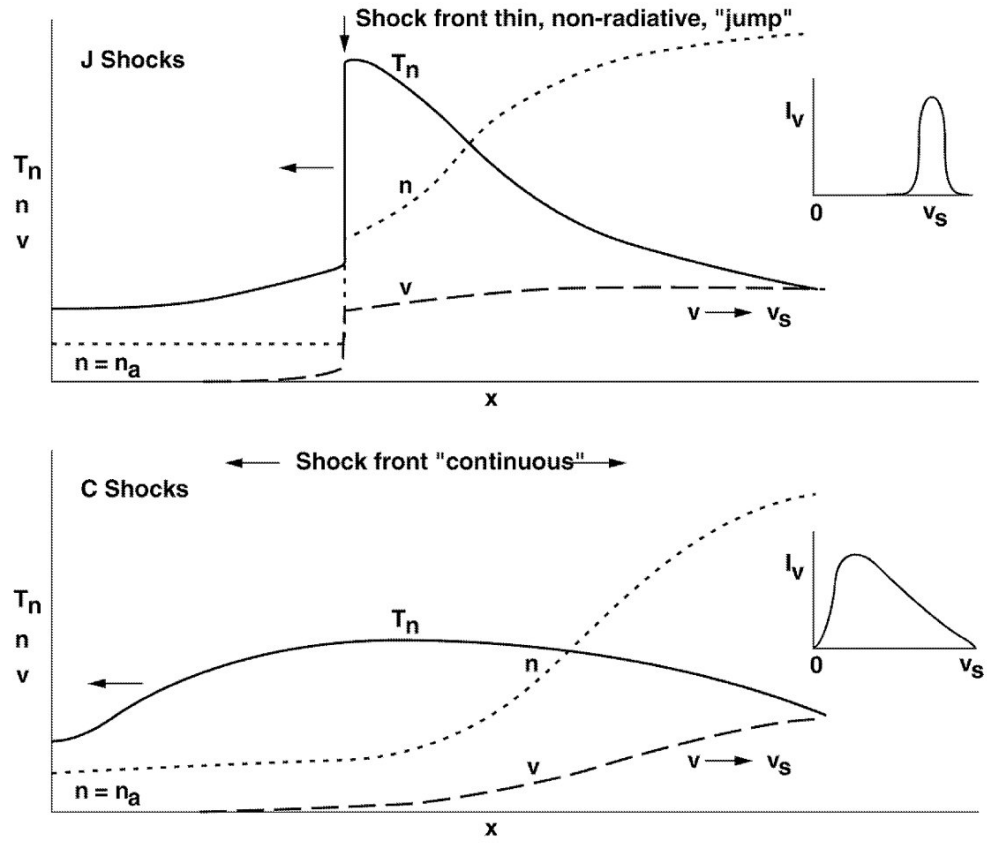

Figure 1.5: The structure of J-shocks and C-shocks (from Hollenbach, 1997).

locity, magnetic waves propagate ahead of the shock and excite ions in the preshock gas, which then collide with and gradually heat the neutral molecular species before they encounter the shock. This is called a magnetic precursor and in this way information about the approaching shock is communicated ahead of the shock (Draine, 1980). If the shock is weak enough and the ion Alfvén velocity is strong enough, i.e. if the magnetic field is sufficiently strong and the fluid is weakly ionised, the J-shock may be eliminated altogether leaving a smooth increase of density and temperature known as a continuous-shock (C-shock).

Further out along a bow-shaped J-shock, the shock velocity may become lower than the ion Alfvén velocity and the J-shock may make a transition toward C-shock structure (Smith & Mac Low, 1997). Although J-shock models predict that molecular hydrogen is dissociated for shock speeds in exceeds of $v_{\rm shock} \geqslant 25\,{\rm km\,s^{-1}}$, the effects of magnetic fields in C-shocks are thought to allow molecular hydrogen to survive in shocks with velocities of below $v_{\rm shock} \leqslant 45\,{\rm km\,s^{-1}}$ (Draine et al., 1983). This is due to the lower temperature shocks that are predicted for C-shocks as

compared to J-shocks and the dependence of the dissociation rate on temperature. Figure 1.5 shows some of the main differences between J-shock and C-shock structures. For a C-shock of velocity, $v_{\rm shock} \sim 40\,{\rm km\,s^{-1}}$, the temperature of the ions and neutrals are thought to be about 30000 K and 3000 K respectively. The relatively low temperatures of the neutrals establishes emission from the molecular cooling of species such as H_2, H_2O, CO, OH and cooling from collisions with dust grains as the dominant forms of cooling. The importance of the different species to cooling depends on the density and the velocity of the shock. Once again the illustration in Figure 1.4 gives an outline of the locations of the different cooling zones.

1.6 Observations

Bipolar outflows from YSOs contain molecular, ionized, and atomic material in a wide range of excitation conditions. Assuming the jet-driven bow-shock model discussed above in Section 1.4, we can break the flow down into several components. These components are: the highly collimated optical and/or molecular jet; the HH objects that are created at shocks along the length of the jet; the collimated extremely high velocity (EHV) atomic and molecular flow that is driven by the momentum from the jet; and the less well collimated and much slower CO outflow consisting of ambient gas swept up by the underlying flow. Each of these components can be observed using different techniques and species transitions. Higher energy, lower wavelength emission tends to trace high velocity material, e.g. X-rays are observed coming from shocks with speeds higher than $300\,{\rm km\,s^{-1}}$. Also, when comparing the emission lines of a particular species, higher excitation lines tend to trace higher velocity regions. Good examples of this are the ro-vibrational lines of molecular H_2 that trace higher velocities than its purely rotational lines and the optical emission of the [OIII] line when compared to the emission of the [OII] and [OI] lines.

1.6.1 Optical Observations

Jets and the HH objects they create can be observed at optical wavelengths in regions of low visual extinction, for example regions in which most of the ambient molecular material has been already accreted onto the star or dispersed. As in the observations of Mundt & Fried (1983) and Mundt et al. (1987), optical forbidden emission lines provide a powerful tool for examining jets and HH objects since they appear bright in these lines. They are called forbidden emission lines because the probability of the transitions occurring at normal gas densities is extremely low. Common lines that are observed, at visual wavelengths, include [OI] at λ=6300, 6363, [SII] at λ=6717, 6731, [NI] at λ=5198, 5200, [OII] at λ=3727, [NII] at λ=5755, 6548, 6584, [CaII] at λ=7291 and [OIII] at λ=4959, 5007.

As mentioned above in Section 1.5, these lines arise in the extended cooling layers that occur behind shocks when gas, which has been heated by travelling through the shock, cools and recombines while continuing to emit strongly. Once the gas has cooled sufficiently in the post-shock region, i.e. after a cooling time, most of this emission will be gone. Thus these lines are most useful for tracing the cooling layers behind shocks. Atomic lines such as Hα are used to trace the layer immediately following a shock since excited neutral hydrogen atoms give rise to strong Balmer emission. Figures 1.2 and 1.6 show the stellar jet systems HH 46/47 and HH 111 in [SII] (red) and Hα (green/blue) emission. Section 1.7 outlines some of the properties of stellar jets obtain from various observations.

Radial velocity calculations obtained from these line profiles show that the majority of the flows are blueshifted with respect to stellar velocity, i.e. they are moving towards us. This anomaly occurs as a result of it being easier to detect blueshifted flows than their redshifted counterparts, since a thick circumstellar disk or the cloud into which they are pointing often obscures these counterflows.

1.6.2 Ultraviolet Observations

Continuum emission increases towards the blue and ultraviolet parts of the spectrum, as discovered by Bohm et al. (1974). Following spectrophotometric observa-

tions, Dopita et al. (1982a) suggested that the spectrum is probably produced when two-photon emission from hydrogen receives a strong enhancement via collisional excitation.

Ortolani & Dodorico (1980) produced the first far UV observation of a HH object, HH 1 between λ=1000 and λ=2000, which showed a strong continuum and confirmed the blue-violet excess found by Bohm et al. (1974). They also found strong emission lines in [CIV] and [CIII]. The strengths of these emission lines exceeded the strengths expected from the shock models of that time and pointed out the inadequacy of such models. This issue was resolved when Cardelli et al. (1988) proposed an alternative extinction curve for the interstellar medium which could be used in the shock models. Extinction is the absorption and scattering of light by dust and gas between the emitting object and the observer and is often called reddening because blue light is weakened by more than red light. The use of this new curve in the shock models produced less weakening in the blue and ultraviolet regimes bringing these models more into line with the observations.

1.6.3 Infrared Observations

In regions of high visual extinction shocks can sometimes be traced in the near- and mid-infrared transitions of H_2 or in the forbidden lines of [FeII]. Both of these provide numerous lines with different levels of excitation that enable the examination of the shock kinematics. H_2 molecules become collisionally excited in dense regions at temperatures of a few 10^3 K, therefore their transitions can be used as tracers of the shocked molecular gas. High velocity shocks will dissociate H_2 so there will be very little radiative emission from H_2 behind strong shocks (Hollenbach & McKee, 1979; Downes & Cabrit, 2003).

On the other hand, there will be radiative emission behind non-dissociative, lower velocity shocks. Elias (1980) was one of the first to detect molecular hydrogen emission lines in the infrared and pointed out that the typical H_2 line widths were less than $70\,\mathrm{km\,s^{-1}}$ and that typical radial velocities were no more than 30 km/sec in magnitude which implied shock velocities of no more than $20\,\mathrm{km\,s^{-1}}$. This was

in disagreement with the optical observations and the plane-parallel shock models of the time. Also in disagreement were the unusually strong line ratios of [SII],[OI] and [CI], found by Boehm et al. (1980) in some objects. These disagreements lead to the eventual need for a new type of model, the bow shock model, in which the shock speed varies along the bow with the largest velocities found at the apex.

Therefore, H_2 can trace weaker shocks not visible in the optical. In particular, two useful lines of H_2 that are excited in shocks with velocities in the range 10-50 $\mathrm{km\,s^{-1}}$ are v=1-0 S(1) at λ=2.122 μm and v=2-1 S(1) at λ=2.247 μm. Observations in these lines, and the radial velocities derived from their line profiles, provide evidence in support of the velocity range and dissociation discussed above. Higher excitation vibrational lines reveal higher velocity more collimated flows that are analogous to the EHV CO outflows discussed elsewhere in this section. H_2 line observations of individual shock fronts have been compared to those predicted by shock models in order to determine which model, in combination with what physical parameters, is best able to predict the observered emission (e.g. Smith et al., 2003). In this way H_2 observations can be used to constrain outflow parameters. H_2 has also proved to be useful as a tracer of parsec-scale jets in the L1641-N complex (Stanke et al., 1998). Also in the same cluster a 10.6 pc flow HH 404/127 has been discovered by Reipurth et al. (1998b), assuming their interpretation of the system's axes of symmetry are correct.

Whereas H_2 traces the molecular component of outflows, [FeII] is particularly useful at picking out atomic jet components with moderate excitation levels and is often used to pick out the base of jets in embedded regions. For example Reipurth et al. (1999) traced the jet in the HH 111 system to within 2.4″ of its VLA source as can be seen in Figure 1.6. The figure on the left hand side shows observations, using two narrow band filters, that contain the [FeII] 1.64 μm and H_2 2.12 μm emission lines which are shown in blue and red respectively. The jet and counter jet can be seen clearly in [FeII] but are very weak in H_2. The figure on the right hand side, originally given in Reipurth et al. (1997b), shows [SII] emission in blue which comes mainly from the core of the jet and Hα emission in orange which comes mainly from

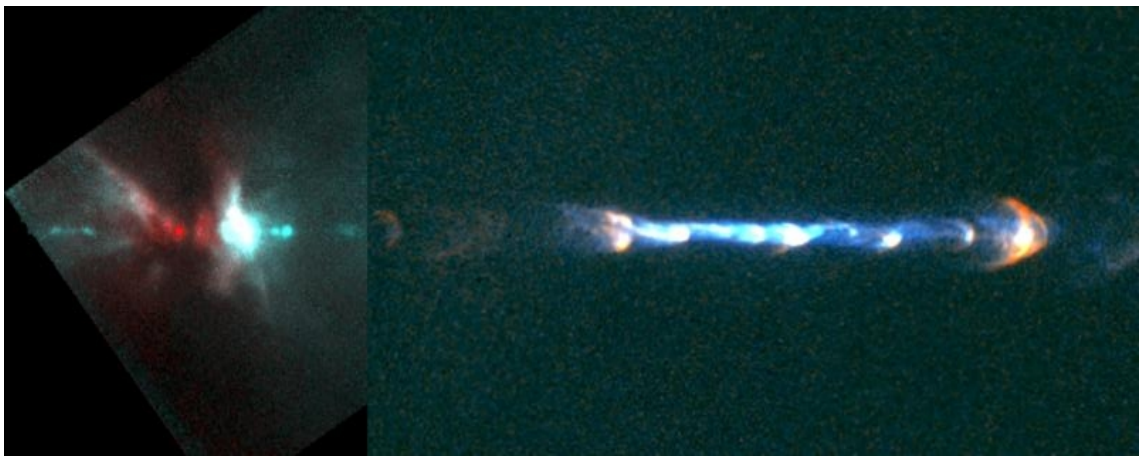

Figure 1.6: A mosaic image of HH 111 based on HST NICMOS images (left) and WFPC2 images (right). See text for details. (Credit: Reipurth et al. (1999) and NASA/ESA)

shocks being driven into the surrounding material. Reipurth et al. (1997a) showed the object to have a length of 7.7 pc making it the longest known HH flow at that time. We can clearly see a chain of faint knots followed by a large bow shock further along the flow.

1.6.4 Millimeter-wavelength Observations

Millimeter-wavelength observations, in ^{12}CO J=2-1 and ^{12}CO J=1-0, have been extensively carried out and reveal poorly collimated bipolar molecular outflows of low velocity (3-30 $\mathrm{km\,s^{-1}}$). Section 1.8 describes a number of properties of molecular outflows that have been determined from these observations. Downes & Cabrit (2003) explain these CO outflows in terms of the entrainment of ambient gas (see also De Young, 1986; Raga & Cabrit, 1993, among others). Intermediate velocity (30-100 $\mathrm{km\,s^{-1}}$) molecular bullets have been observed in some of the more highly collimated CO outflows. One well studied example is the HH 711 flow in which Lizano et al. (1988) detected high velocity 21 cm HI emission, up to 170 $\mathrm{km\,s^{-1}}$ along the line of sight, driving CO emission travelling at intermediate velocities of up to 100 $\mathrm{km\,s^{-1}}$. A later study by Bachiller & Cernicharo (1990) found discrete CO bullets on the outflow axis moving at velocities $> 100\,\mathrm{km\,s^{-1}}$.

In the HH 111 jet system Cernicharo & Reipurth (1996) carried out high spatial resolution, 12″, ^{12}CO J=2-1 observations and found extremely high velocity (EHV)

CO towards the principal HH working surface, HH 111V, travelling at the same velocity as the optically emitting gas with true space velocities calculated as being between 250 and 500 $\mathrm{km\,s^{-1}}$! They also discovered three equidistant CO bullets further out, precisely along the flow axis, which were not detected in the optical but which had space velocities of about 240 $\mathrm{km\,s^{-1}}$. They concluded that the reason three of these bullets were not optically visible was most likely due to the density of the ambient medium, at such large distances from the main cloud core, being so low that there is no shock interaction between the bullets and the near-vacuum through which they move.

Millimeter-wavelength observations have also focused on other molecular species each of which are observed to trace different components of the gas (Bachiller & Perez Gutierrez, 1997). Some species were found to trace material at rest (C_3H_2, N_2H^+, $H^{13}CO^+$, DCO^+) while others corresponded to shocked regions (SiO, CH_3OH, H_2CO, HCN, CN, SO, SO_2). In particular, SiO emission was found to trace the interaction of the outflow with the ambient gas at the end of the outflow lobe as well as the high velocity molecular bullets mentioned previously.

1.6.5 Centimeter-wavelength Observations

Centimeter wavelength emission, mostly due to free-free emission that is produced when free electrons are scattered off ions without being captured, has also revealed radio continuum jets emerging from their YSOs.

The 21 cm line of HI, which is a result of hyperfine splitting in which the spins of the proton and electron change from a parallel to antiparallel configuration, does not require shocks to be observable, since this species is excited by collisions at the ambient temperature of the cloud. It has been used to trace entrained gas in outflows (Lizano et al., 1988). Such HI observations are made very difficult by the relatively poor angular resolution of the cm single-dish telescopes and by the confusion with foreground and background emission from the Galaxy.

1.6.6 X-ray and More Recent Observations

More recently, as a result of the launch of the XMM/Newton and Chandra (CXO) X-ray observatories, X-ray emission has been detected emanating from shocks with velocities in excess of $300\,\mathrm{km\,s^{-1}}$. Some are associated with HH objects, Pravdo et al. (2001), while others appear to be associated with knots found in [FeII] at the bases of the jets (Favata et al., 2002; Pravdo & Tsuboi, 2005).

Another recent development was the discovery of externally irradiated jets by Reipurth et al. (1998a); Cernicharo et al. (1998). Strong ultraviolet radiation fields, of Lyman continuum ($\lambda < 912$) and far-ultraviolet ($912 < \lambda < 2000$) radiation, from a massive star ionises the interstellar medium in its vicinity. A jet flowing into such a region becomes ionised at its surface or throughout its entire body. As discussed by Bally & Reipurth (2001), in a situation such as this, the observed intensity of the Hα line can be directly related to the emission measure, and the [SII] lines can be used to measure the electron density. Measurements of the radial velocity field and flow morphology can be combined with these parameters to infer many flow properties such as the mass-loss rate, momentum carried in each beam, and the energy injected into the cloud by the flow. These calculations should be much more reliable than previous calculations based on shock analysis which relied on electron densities derived on the basis of line ratios and assumptions such as a particular ionisation fraction. Recent studies have shown that irradiated flows are common in HII regions. A number of these flows show extreme bends, Bally et al. (2006) considered several mechanisms for bending jets, including radiation pressure, the rocket effect on a neutral jet, and the impact of a side wind.

1.7 Properties of Jets

From observations, a number of jet properties can be determined. Some of the most important of these are discussed below including the velocity, density, radius, collimation and length.

1.7.1 Velocity

Radial velocities of up to 400 km s^{-1} have been observed in jets (Mundt et al., 1987) although typical radial velocities are in the range 100-150 km s^{-1}. These velocities are obtained from the line profiles and linewidths of shock excited species, such as [NII] and [OIII]. The velocities are usually observed in the region behind a shock, and so they represent the post-shock gas velocity whose magnitude will be less than the jet velocity behind the shock, $v_{\rm post}$, by an amount proportional to the shock velocity, $v_{\rm shock}$. Therefore, the true radial velocity of the jet will be underestimated. For a weak internal shock, $v_{\rm shock} < 30$ km s^{-1}, this underestimate will not usually be significant, but for a stronger shock it will be.

Observations of the proper motions of the bright knots found along the length of jets, reveal tangential velocities of up to 350 km s^{-1} with more typical values in the range 50-200 km s^{-1} (Mundt et al., 1987). The proper motion of a shock indicates the propagation velocity of the shock, $v_{\rm prop}$, the value of which depends on the pre-shock velocity, $v_{\rm pre}$, and the shock velocity, $v_{\rm shock}$, according to the shock relations. Therefore, velocities obtained through proper motions will also, along with the radial velocities, underestimate the jet velocity, $v_{\rm post}$. For this reason, in order to derive the true space motion of a jet accurately, models of the dynamics of the shocks are required (see Morse et al., 1992). Nonetheless, by simply using Pythagoras' theorem, typical true space velocities are in the range 100-250 km s^{-1} with some jets found to have true space velocities of up to 450 km s^{-1}. More recent observations also support these velocity ranges. For example, Micono et al. (1998) and Coppin et al. (1998) derived molecular jet velocities ranging from 100-500 km s^{-1} from the proper motion of H_2 v=1-0 S(1) knots.

The shock velocities, $v_{\rm shock}$, implied by emission linewidths and line ratios are significantly lower than the true space velocities measured based on radial velocities and proper motions. Hence, some internal shocks are propagating into a co-moving medium (Dopita, 1978), that is already moving out from the stellar object with appreciable velocity, of several hundred km s^{-1} in some cases. Also, it has been suggested that the temporal variability of the jet at the source produces these internal

shocks in the jet. They occur when recently ejected, high velocity material "catches up" with previously ejected material that's moving at a slower velocity. The end result is numerous velocity fluctuations over the length of the jet (Raga et al., 1990).

1.7.2 Density

Jet density is an important property since the amount of cooling, and hence emission, that occurs behind a shock depends on the jet density and the shock velocity. Shock velocities can be determined from emission linewidths and line ratios but determining the jet density is more complicated and first requires the determination of the electron density of the plasma within the jet. One method calculates the electron density based on line ratios from regions of emission behind shocks, such as the ratio of the [SII] line at λ=6717 to the [SII] line at λ=6731. The intensities of these lines depend on, among other things, the ionization fraction in the shocked region, the geometry of the shock and the strength and structure of magnetic fields in the region. These dependencies must be taken into account when inferring the post-shock electron density and may introduce errors into the calculations.

To convert the electron number density to total number density it must be divided by the ionisation fraction, f, of the gas in the region where the emission lines are measured. The ionisation fraction can be calculated from several different line ratios, such as [OI](λ6300)/Hα, [SII](λ6723)/Hα and [NI](λ5200)/Hβ, and is typically found to be between 3% (Hartigan et al., 1994) and 10% (Raga, 1991). Hartigan et al. (1994) used an ionisation rate of approximately 3% but also described a necessary density correction, resulting in a factor of four reduction in density. This correction is required because material in the post-shock region is more compressed when compared to the average material in the jet. The uncertainty in the ionisation fraction, and hence any densities derived using it, is the main reason why a method based on observations of irradiated jets is now the preferred method of some authors.

The discovery of externally irradiated jets by Reipurth et al. (1998a) and Cernicharo et al. (1998) (see Section 1.6) has lead to improved calculations in the densities of jets. In these systems we observe the entire flow and not just the portion

that radiates behind a shock. If a jet is fully ionised by the external radiation field, the derived electron number density of the plasma within the jet *is* the jet number density, thus the calculations should be much more reliable than previous calculations. As detailed by Bally & Reipurth (2001), the peak Hα surface brightness in an emitting region can be used to obtain a measure of the amount of emission from the jet in that region. Also, the depth of the emitting region along the line of sight can be set equal to the jet radius, i.e. the jet can be assumed to be cylindrical. The radius of the jet can be measured directly on the plane of the sky, so using this value in conjunction with the peak emission measure for the emitting region, the electron number density and hence the jet number density can be calculated.

Bally & Reipurth (2001) obtained number density values of between 500-2000 cm^{-3} with an average number density in the features they studied of 1150 cm^{-3}. Since some irradiated jets are likely to be only partially ionized, with a shielding layer that protects a neutral core from the Lyman continuum radiation, these densities may be underestimates. Nevertheless, the density values obtained by Bally & Reipurth (2001) are comparable to previous calculations of 10^2-10^4 cm^{-3} (Hartigan et al., 1994).

Measurements of the velocity field and flow morphology can be combined with the above density calculations to infer many flow properties such as the mass-loss rate, the momentum carried in each beam, and the energy injected into the cloud by the flow.

1.7.3 Radius

Mundt et al. (1987) list the radii of some jets as ranging from below 1×10^{-3} pc up to 4.6×10^{-2} pc. These radii are just about resolvable using ground-based telescopes, with upper limits being given for some of the radii as their jet widths were smaller than the telescopes resolution. A number of these radii were later confirmed using HST observations by Ray et al. (1996). In this paper, jets in HL Tau, HH 30, HH 1 and HH 34 were traced back very close to the source. In the case of HH 30 the jet was traced to within 0.25″ (35 AU, 1.69×10^{-4} pc or 5.2×10^{14} cm) of the source.

They found that the radii of these jets remained large and decreased only slowly as the source was approached. So jet radii vary slowly with distance from the source depending on a jets collimation. More recent observations of externally irradiated jets (Bally & Reipurth, 2001) have listed jet widths that range from the telescope resolution of 1.12×10^{-3} pc up to 8.92×10^{-3} pc.

1.7.4 Collimation

Jets are highly collimated outflows with opening angles of a few degrees further out than 50 AU, from the central star. Cabrit (2007) notes that this is compatible with the "Mach angle", α, expected for the free lateral expansion of a supersonic jet which is

$$\alpha = 2 \times \tan^{-1}(c_s/v_j) \simeq 3.8^{\circ} \tag{1.6}$$

for a typical temperature of 10^4 K and a jet speed of $v_j = 300\,\mathrm{km\,s^{-1}}$. Within 50 AU the results of Hartigan et al. (1994) show much wider opening angles of 20°-30°. This shows that jets very quickly become collimated, after initially being launched with wider angles, and that collimation occurs on quite a short length scale (50 AU). Typical length-to-width ratios for jets are therefore $\sim$ 15:1.

1.7.5 Length

Due to the temporal variability of jets at their sources (see Section 1.7.2) it is difficult to accurately measure their lengths. Bowshocks can be found that were created in previous outflow episodes, i.e. they do not coincide with the termination of the most recently ejected jet material. The question then arises as to whether a previous outflow episode should be considered to contribute to the length of the most recent, and more obviously jet-like, outflow episode. One could consider the length over which a jet emits detectable radiation in a continuous streak, since this is easier to measure. This length represents the length of the most recently ejected jet and is a lower limit on the overall outflow length.

For outflows in Orion, Bally et al. (2006) measured the lengths of 24 jets using HST observations. They were found to have lengths of between 0.65″ and 20″ which, assuming Orion is at a distance of 470 pc, equals 1.4×10^{-3} pc and 4.4×10^{-2} pc respectively. The average length of all the jets was about 5.3″ or 1×10^{-2} pc. Looking at one particular case, HH 878, the length of the detectable jet emission is 1.5″ or 3×10^{-3} pc. Although the jet disappears at that distance from the source, a pair of arcsecond-scale bow shocks can be seen about 19″ and 33″ northwest of the source. This illustrates nicely the difficulty in differentiating between the jet length and the outflow length. The total length of the bipolar outflow is 50″ or 0.11 pc.

Alternatively, and perhaps more accurately, if we consider bow shocks to be the termination points of jets, then since bow shocks are typically 0.1 pc from their exciting stars (Hartigan et al., 2000), an average jet length of 0.1 pc is obtained. In some extreme cases bow shocks have been discovered at distances of over 5 pc away from their sources, for example the HH 404/127 outflows discovered by Reipurth et al. (1998b) to have a combined length of up to 10.6 pc. Parsec-scale outflows have also been observed by other authors (such as Marti et al., 1993; Bally & Devine, 1994; Ogura, 1995; Reipurth et al., 1997a; Gomez et al., 1997), some of which have been discussed in McGroarty et al. (2004). The results of this paper are discussed in more detail in Chapter 4.

1.8 Properties of Molecular Outflows

From the different types of observations mentioned above, especially the ^{12}CO J=2-1 and ^{12}CO J=1-0 transitions of CO, a number of properties of molecular outflows have been determined. These properties have been outlined in numerous reviews. A critical review presented by Masson & Chernin (1993) shows that the observed properties of molecular outflows can be explained by a model in which the molecular outflow is driven solely by a collimated jet. Lada & Fich (1996) described the structure and energetics of a highly collimated bipolar outflow called NGC 2264G, in terms of outflow properties. Bachiller (1996) reviewed observations at various wavelengths including those captured with millimeter-wavelength interferometers and

discussed the different components of outflows especially the extremely high velocity (EHV) components. The strong and weak points of the different outflow models have been summarised, by Cabrit et al. (1997), in terms of how well they predict the observed outflow properties, while Richer et al. (2000) reviewed the commonalities and differences in outflow structure between low-mass and high-mass systems and described the shock chemistry and energetics of outflows. In particular they used the correlation of the flow momentum deposition rate with source luminosity to estimate the ratio, f, of mass ejection to mass accretion and obtained a value of $f \sim 0.3$, that seemes to hold over the whole range of luminosities. Some other common properties of molecular outflows that are discussed in the above reviews are outlined below. These properties become useful in constraining, and deciding between, outflow models.

1. Most molecular outflows are bipolar (Lada, 1985), consisting of red- and blue-shifted lobes on either side of a central driving source, with each lobe displaying a high degree of symmetry in their basic physical properties that suggests a common launch mechanism. In cases where bipolar symmetry is not observed environmental factors are thought to be responsible for this lack of symmetry. Different conditions in the molecular cloud on either side of the central driving source, such as a variation in density, can result in both lobes having very different morphologies. A good example occurs in the NGC 2024 cloud core, Richer et al. (1992) observed that most of the CO could be found in a lobe to the south of the source and suggested that the lack of a northern lobe is due to the lack of ambient molecular material where the flow breaks out into an ionised HII region.

2. The dependence of outflow morphology on cloud structure, as described in item (1) above, suggests that outflows consist of swept up material. This is also supported by the calculated masses of outflows, some of which are over 100 $M_{\odot}$ (for example MON R2 from Wolf et al., 1990). Masses of this magnitude, when compared to the typical stellar masses of class 0 low-mass protostars, make it unlikely that all of the mass in such an outflow could come solely from the

region around the driving source.

3. There is a relatively high level of collimation in molecular outflows with observed *initial* opening angles of $\sim 20^{\circ}$-90° and corresponding length-to-width ratios ranging from 3:1 to >20:1 (Arce et al., 2007).

4. Outflows exhibit an average line profile that indicates a power-law variation of mass with velocity, $m(v) \propto v^{-\gamma}$ with $\gamma \sim 1.3 - 2.1$ (Kuiper et al., 1981; Lada & Fich, 1996).

5. The collimation of an outflow increases with its velocity. Hence limb-brightened cavities are found at low velocities, and high collimation is found at higher velocities.

6. Position-velocity (PV) maps often show the systematic increase of flow velocity, with distance from the central source, in flows with well-separated outflow lobes (Lada & Fich, 1996). This is often referred to as the "Hubble law" in which $v \propto r$.

7. Overlapping of blueshifted and redshifted emission rarely occurs within the same flow lobe, implying that outflows are strongly forward directed with very little transverse motion. Lada & Fich (1996) found the contrast in intensity in each lobe, between gas at redshifted and blueshifted velocities, to be at least a factor of 20.

8. Molecular outflows are associated with optical and infrared jets and HH objects.

9. As mentioned in Section 1.6, some extremely high-velocity (EHV) CO emission has been observed along the flow axis of a number of outflows (Cernicharo & Reipurth, 1996). Some of these CO "bullets" were not detected in the optical even though they were found to have true space velocities of about $240\,\mathrm{km\,s^{-1}}$. Evidence of these high velocity "bullets" has also been observed in vibrationally excited H_2, and shock-enhanced species like SiO or CH_3OH (Bachiller & Perez Gutierrez, 1997).

1.9 Jet Launching Mechanisms

Several models have been proposed to explain how jets are launched, one of the earliest being the model by Barral & Canto (1981), mentioned previously. This model was a purely hydrodynamical model in which the wind was collimated by the thermal pressure from the surrounding accretion disk. Königl (1982) noted that "the expanding bubble could become unstable to the formation of de Laval nozzles which channel the flow into two oppositely directed, supersonic jets". This model was based upon a medium with an anisotropic density and pressure distribution which Königl (1982) concluded required a magnetic field for its creation. Also, as argued by Decampli (1981), the high temperatures that this model would require at the base of the jet would mean that the radiative losses, due mainly to X-ray emission at these high temperatures, would be much larger than the stellar luminosity creating a mechanism that would be too inefficient. A magnetic field coupled to the central protostar or to the inner part of a circumstellar disk was proposed and provides a powerful mechanism to explain the production of jets. Indications of jet rotation have been observed by Bacciotti et al. (2002) using high resolution spectro-imaging and adaptive optics methods. Derived toroidal velocities were found to be in the range $6-15\,\mathrm{km\,s^{-1}}$, depending on position. It must also be noted that the kinematic structure of a rotating jet involves faster and more collimated gas being continuously bracketed by wider and slower material.

There are two main magnetohydrodynamical (MHD) wind models that differ depending on where the jet originates, either at the disk surface or at the star-disk boundary layer. Both models agree that winds are launched by a centrifugal force originating from the rotation of the accretion disk which launches the accreting material along the magnetic field lines. The winds carry off angular momentum and gravitational binding energy from material in the accretion disk and thus prevent the star from rotating at breakup velocity. This effectively means that it is accretion which powers the winds and that the wind mass-loss rate, $\dot{M}_w$, and the accretion rate, $\dot{M}_a$, are interlinked. Calculations of the accretion rates and wind mass-loss rates of several sources, obtained from observations of their optical spectra, support

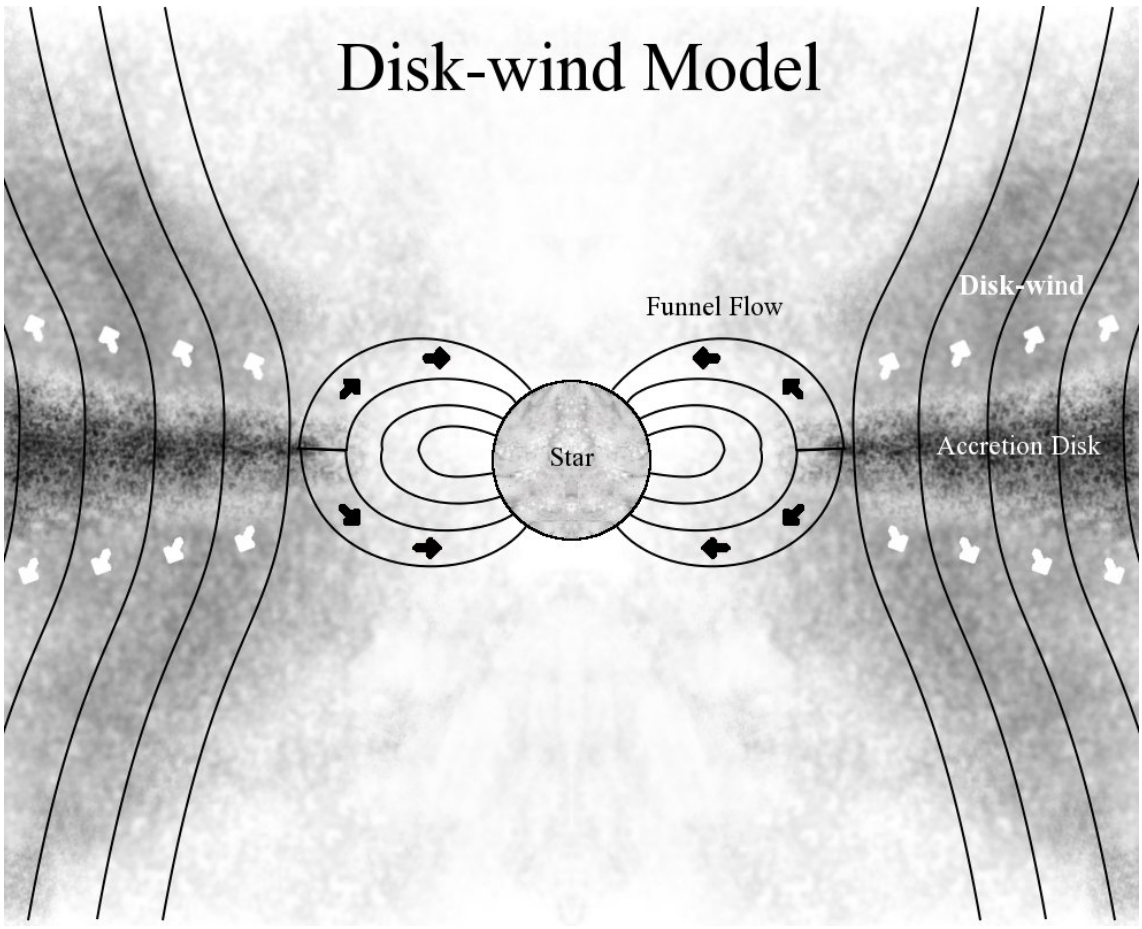

Figure 1.7: Disk-wind model.

a ratio of $\dot{M}_w/\dot{M}_a \simeq 0.1$ (Gullbring et al., 1998). Essentially, the point the two models disagree on, is the location on the disk where the jets are launched from.

1.9.1 Disk-driven Wind

A model for the production of extragalactic jets by Blandford & Payne (1982) was adapted to the production of YSO jets by Pudritz & Norman (1983, 1986). In this model the wind is launched, along the magnetic field lines that thread the disk, from every radius upon the disks surface all the way down to the co-rotation radius of the disk, the radius where the Keplarian angular speed of rotation, Ω_x, equals the angular speed of the star, Ω_*. The greatest amount of energy is released from the inner portions of the disk. Every annulus of a large keplerian disk rotates near breakup velocity, so the large centrifugal forces that this creates, assuming a large enough magnetic field, can be applied to launch a powerful disk-wind. One of the main criticisms of this model is that the magnetic fields it requires are too large to

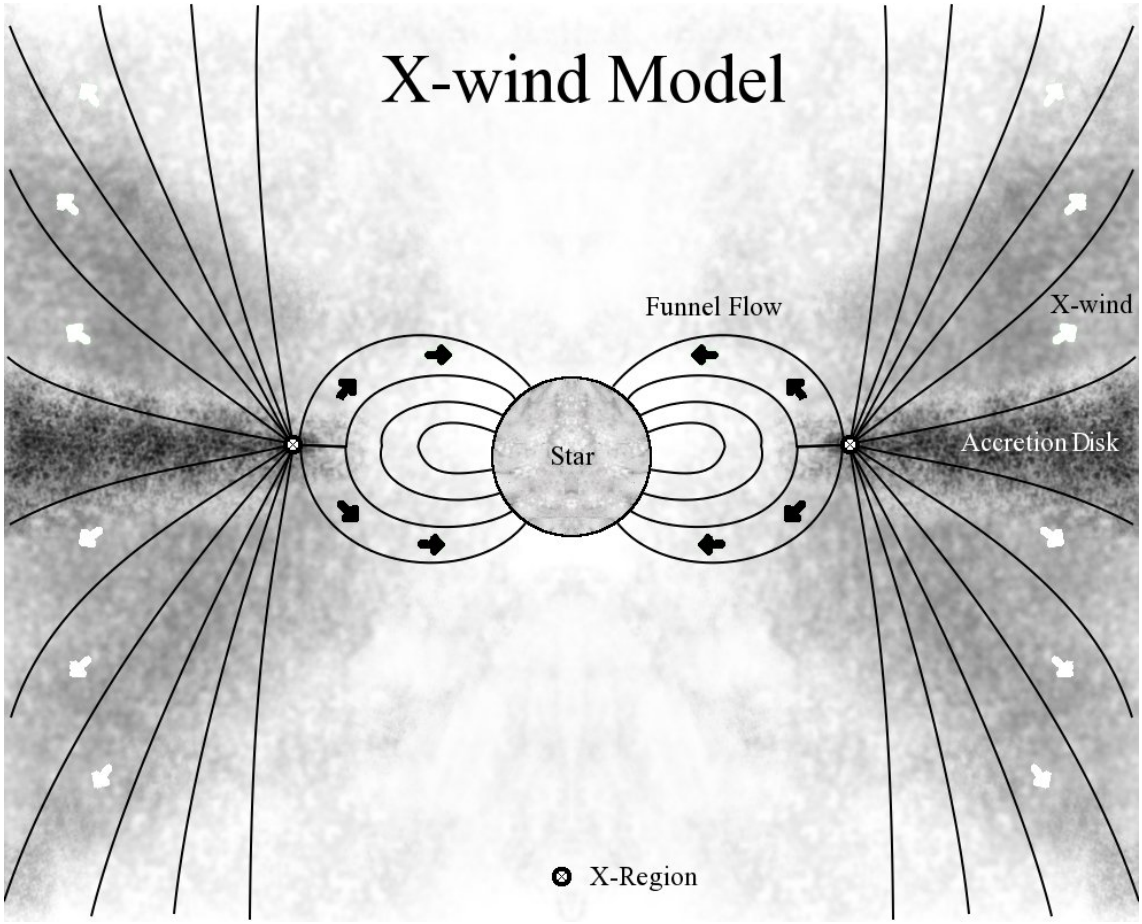

Figure 1.8: X-wind model.

be generated everywhere along the disk. Shu et al. (1994) states that the "shielding currents in the surface layers of the disk prevent stellar field lines from penetrating the disk everywhere except for a range of radii about $\varpi = R_x$", where R_x is the co-rotation radius. They cite the calculations of Umebayashi & Nakano (1988) that predict very low ionisation levels in the disk at all but the innermost radii. The low ionisation is a result of high surface densities in the disk that block ionising radiation. Shu et al. (1994) propose that ohmic dissipation and ambipolar diffusion would rid the interior of the disk of strong magnetic fields. The external parts of the disk, closest to the surface, will be ionised so it is possible that these regions support the magnetic field but it is unknown if they could support a field of large enough strength.

1.9.2 X-wind

The main difference between the X-wind model (Shu et al., 1988) and the disk-wind model above is that magnetic fields, and hence a wind, are only predicted to be present in the boundary layer between the accretion disk and the star where their rotational velocities are similar, i.e. at a range of radii about $\varpi = R_x$, the co-rotation radius or X-point. The reasoning behind this was given in the previous section.

Pelletier & Pudritz (1992) pointed out that stars must spin at near breakup velocity near their equator in order for sufficient momentum to be transferred to a centrifugally driven wind but from the observations of Vogel & Kuhi (1981) we know that they rotate much slower than this. Modified versions of the X-wind model allow for the star to be rotating at below the breakup velocity (Shu et al., 1994).

1.10 Structure of this Work

Astrophysical systems like jets, outflows and supernova remnants are mainly observed thanks to their strong shocks. These systems and their shocks, along with other hydrodynamical systems, can be modelled using different sets of equations, one such set of equations is the Euler equations which are based on the conservation of mass, momentum, and energy of a compressible, inviscid fluid.

The physics of these astrophysical systems and their shocks is highly non-linear and as a result of this complexity, the use of computational simulations is necessary. Numerical methods are used to integrate the hydrodynamical equations. The numerical method that is chosen needs to be able to satisfactorily resolve the strong shocks that can occur in these types of fluid flows. Chapter 2.1 describes the Euler equations and some of the most common numerical methods that are used to integrate the hydrodynamical Euler equations. The particular method used in this work, which is a MUSCL-type scheme that is second order accurate in space and time, is also outlined.

Chapter 3 discusses a new cooling function based on the results of recent quantum

mechanical calculations of the cross sections for ro-vibrational transitions. Several simulations were undertaken with and without this new cooling function. The details and results of these simulations are given in this chapter.

Chapter 4 details long duration numerical simulations carried out on the propagation of jet-driven molecular outflows into inhomogeneous media. The density in these media decreases with distance from the jet source, therefore we simulate molecular outflows in the process of leaving their parent molecular clouds. The effects of this on the density and velocity structure, mass-velocity relations, age estimates and the length-to-width ratios of these outflows is discussed in this chapter.

Finally, in Chapter 5 we summarise the results and conclusions of this work and discuss the possibilities for future studies.

Chapter 2

Numerical Methods

2.1 Computational Fluid Dynamics

Fluid dynamics concerns the study of fluids in motion while computational fluid dynamics (CFD) concerns computer simulations of fluid flows. In fluid dynamics the governing equations, often in the form of partial differential equations, are based on some basic assumptions that are made about the fluids being studied. In CFD these partial differential equations are converted into a system of algebraic equations in order to create computer simulations of the interaction of fluids. Generally the initial state of a particular fluid can be described by sets of values of the flow variables at selected spatial locations. These values can then be advanced in space and time based on the particular system of algebraic equations being considered to produce quantitative predictions of the fluid flow. For this work, the equations used are based on the Euler equations where the assumption of a compressible fluid in which there is no viscosity is made. These equations are outlined in Section 2.2. In CFD in order to solve the various systems of algebraic equations and advance the system in time and space many competing numerical methods are utilised. Among others these methods include finite difference, finite element, finite volume, and spectral methods. A brief outline of each method is given in Section 2.4 along with a more detailed discussion of finite volume and finite difference methods.

2.2 The Euler Equations

The governing equations of hydrodynamics are expressions of conservation and the second law of thermodynamics. The quantities that are conserved are mass, momentum and energy. By conservation we mean that these quantities are neither created nor destroyed but may be redistributed or converted from one form to another. The second law of thermodynamics states that a fourth quantity called entropy should never decrease following the fluid.

The Euler equations govern the motion of a compressible, inviscid fluid. They correspond to the Navier-Stokes equations with zero viscosity and they are usually written in the form shown here because this emphasises the fact that they directly represent conservation of mass, momentum, and energy. In differential form the Euler equations are

$$\frac{\partial \rho}{\partial t} + \boldsymbol{\nabla} \cdot [\rho \boldsymbol{u}] = 0, \tag{2.1}$$

$$\frac{\partial (\rho \boldsymbol{u})}{\partial t} + \boldsymbol{\nabla} \cdot [\rho \boldsymbol{u} \otimes \boldsymbol{u} + p \boldsymbol{I}] = 0, \tag{2.2}$$

$$\frac{\partial E}{\partial t} + \boldsymbol{\nabla} \cdot [(E + p) \boldsymbol{u}] = 0, \tag{2.3}$$

where $\boldsymbol{u} = (u, v, w)$ is the fluid velocity vector, p is the pressure, $\boldsymbol{I}$ is the identity tensor and ρ is the fluid density. The total energy density for the fluid is

$$E = \frac{1}{2}\rho(u^2 + v^2 + w^2) + e_{\text{int}}, \tag{2.4}$$

where the first term on the right hand side is the kinetic energy of the gas and the last term, e_{int}, is the internal energy density of the gas which depends on the pressure and the type of gas being studied. Equation (2.2) includes the divergence

of a dyadic tensor ($\otimes$), so

$$\rho \boldsymbol{u} \otimes \boldsymbol{u} + p\boldsymbol{I} = \begin{pmatrix} \rho u \\ \rho v \\ \rho w \end{pmatrix} \begin{pmatrix} u & v & w \end{pmatrix} + \begin{pmatrix} p & 0 & 0 \\ 0 & p & 0 \\ 0 & 0 & p \end{pmatrix}$$
$$= \begin{pmatrix} \rho u^2 + p & \rho uv & \rho uw \\ \rho uv & \rho v^2 + p & \rho vw \\ \rho uw & \rho vw & \rho w^2 + p \end{pmatrix}, \tag{2.5}$$

where $\boldsymbol{u} = (u, v, w)$. This equation is more often written

$$\rho \left(\frac{\partial}{\partial t} + \boldsymbol{u}.\boldsymbol{\nabla} \right) \boldsymbol{u} + \boldsymbol{\nabla} p = 0. \tag{2.6}$$

When written in conservative vector form, the Euler equations are

$$\frac{\partial \boldsymbol{q}}{\partial t} + \frac{\partial \boldsymbol{f}}{\partial x} + \frac{\partial \boldsymbol{g}}{\partial y} + \frac{\partial \boldsymbol{h}}{\partial z} = 0, \tag{2.7}$$

where

$$\boldsymbol{q} = \begin{pmatrix} \rho \\ \rho u \\ \rho v \\ \rho w \\ E \end{pmatrix} \quad \boldsymbol{f} = \begin{pmatrix} \rho u \\ p + \rho u^2 \\ \rho uv \\ \rho uw \\ (E + p)u \end{pmatrix} \quad \boldsymbol{g} = \begin{pmatrix} \rho v \\ \rho uv \\ p + \rho v^2 \\ \rho vw \\ (E + p)v \end{pmatrix} \quad \boldsymbol{h} = \begin{pmatrix} \rho w \\ \rho uw \\ \rho vw \\ p + \rho w^2 \\ (E + p)w \end{pmatrix}.$$

This form makes it clear that f, g and h are fluxes.

The equations above thus represent conservation of mass, three components of momentum, and energy. There are thus five equations and six unknowns (ρ, u, v, w, E, p). Closing the system requires an equation of state in which we define the pressure p. In order for the fluxes to be functions of only the conserved quantities we require the pressure, p, to be defined only in terms of the mass density (ρ), the three components of momentum (ρu, ρv, ρw) and the total energy density (E). The

most commonly used equation of state is the ideal gas law

$$p = \rho \bar{R} T, \tag{2.8}$$

where p is the pressure, ρ is the density, $\bar{R}$ is the specific gas constant and T is the temperature. The specific gas constant, $\bar{R}$, depends on the gas being studied and is related to the universal gas constant, R, by the formula $\bar{R} = R/M$ where M is the mass of one mole of the gas. This leads to

$$p = \rho \frac{R}{M} T = n_M R T, \tag{2.9}$$

where $n_M = \rho/M$ is the number density of moles of the gas, i.e. the number of moles of the gas per unit volume. Noting that $R = N_A k_B$, where N_A is Avogadro's number which is the number of "entities" in a mole of any molecular substance, and k_B is Boltzmann's constant, the ideal gas law can also be written

$$p = n k_B T, \tag{2.10}$$

where $n = n_M N_A$ is the number density of "entities" in the gas. An "entity" in this case is any elementary particle and for this work includes atoms, molecules and free electrons.

The equation of state used in this work is derived from the ideal gas law (2.10) but before discussing that derivation we need to give some definitions. The heat capacity ratio is defined as

$$\gamma = \frac{c_p}{c_v}, \tag{2.11}$$

where c_p is the constant pressure heat capacity and c_v is the constant volume heat capacity. Each of these constants depend on the gas being studied. The constant volume heat capacity can be related to Boltzmann's constant by

$$c_v = \frac{N k_B}{\gamma - 1}, \tag{2.12}$$

where $N = nV$ is the number of "entities" in the gas. Also by assuming that, at a microscopic level, large numbers of gas molecules interact only upon direct collision we can express the internal energy density as

$$e_{\text{int}} = \frac{c_v}{V} T. \tag{2.13}$$

Manipulation of the these two equations leads to the following intermediate equation

$$T = \frac{(\gamma - 1) e_{\text{int}}}{n k_B},$$

which when substituted into the ideal gas law (2.10) leads to the following equation of state

$$p = (\gamma - 1) e_{\text{int}}. \tag{2.14}$$

Taking this equation along with the equation for the total energy density (2.4) and rearranging them we can express the pressure in terms of the conserved quantities only,

$$p = (\gamma - 1) \left(E - \frac{1}{2} \rho (u^2 + v^2 + w^2) \right). \tag{2.15}$$

This is the equation of state used in this work and will be referred to as the polytropic equation of state.

For an ideal gas the heat capacity ratio, γ, can be related to the degrees of freedom, f, of its constituent particles such that

$$\gamma = \frac{f + 2}{f}. \tag{2.16}$$

Thus we observe that for a monatomic gas, with three degrees of freedom corresponding to motion in the three spatial directions, $\gamma_1 = 5/3 = 1.67$. In a diatomic gas there are also two rotational degrees of freedom so $f = 5$ and $\gamma_2 = 7/5 = 1.4$.

For this work, the abundances of the different elements composing the gas is based on the abundance of the elements in the solar corona. Also, a certain percentage of the hydrogen is in the form of molecular hydrogen which is diatomic. Therefore the value for γ used in this work is based on a gas whose degrees of freedom are a weighted average of $f = 3$ for a monatomic gas and $f = 5$ for a diatomic gas. If n is the total number density and n_{H_2} is the H_2 number density then there are $n - n_{H_2}$ atoms, ions and electrons. Using these number densities to weight the degrees of freedom of the gas gives

$$f = \frac{3(n - n_{H_2}) + 5(n_{H_2})}{(n - n_{H_2}) + n_{H_2}} = \frac{3n + 2n_{H_2}}{n}. \tag{2.17}$$

Substituting this into the equation for γ (2.16) gives

$$\gamma = 1 + \frac{2n}{3n + 2n_{H_2}}, \tag{2.18}$$

which when substituted into the equation for c_v (2.12) gives

$$c_v = \frac{(3n + 2n_{H_2})}{2n} N k_B. \tag{2.19}$$

2.2.1 The Integral or Weak Form of the Euler Equations

The integral form of the Euler equations can be obtained directly from the principles of conservation of mass, momentum and energy. For a one-dimensional flow, consider the fluid in a region $[x_1, x_2]$ during a time interval $[t_1, t_2]$. Conservation of a quantity, q, within this region and time interval states that the change in the total quantity in $[x_1, x_2]$ in time interval $[t_1, t_2]$ equals the flux of the quantity through the boundaries of $[x_1, x_2]$ in time interval $[t_1, t_2]$. This can be written mathematically as

$$\int_{x_1}^{x_2} [q(x, t_2) - q(x, t_1)]\, dx = -\int_{t_1}^{t_2} [f(q(x_2, t)) - f(q(x_1, t))]\, dt, \tag{2.20}$$

where $q(x, t)$ is the quantity per unit volume and $f(q(x, t))$ is the rate at which the quantity, q, flows past point x in the positive x direction.

So in the case of mass, the conservation of mass states that the change in total mass in $[x_1, x_2]$ in time interval $[t_1, t_2]$ equals the mass flux through the boundaries of $[x_1, x_2]$ in time interval $[t_1, t_2]$. This can be written mathematically as

$$\int_{x_1}^{x_2} [\rho(x, t_2) - \rho(x, t_1)]\, dx = -\int_{t_1}^{t_2} [\rho(x_2, t)u(x_2, t) - \rho(x_1, t)u(x_1, t)]\, dt, \tag{2.21}$$

where $\rho(x, t)$ is the density or mass per unit volume, $u(x, t)$ is the velocity and $\rho(x, t)u(x, t)$ is the rate at which mass flows past point x in the positive x direction. Similarly, the conservation of momentum for the Euler equations states that the change in total momentum in $[x_1, x_2]$ in time interval $[t_1, t_2]$ equals the momentum flux through the boundaries of $[x_1, x_2]$ in time interval $[t_1, t_2]$ plus the momentum change due to pressure on the boundaries of $[x_1, x_2]$. Stated mathematically as

$$\begin{aligned}\int_{x_1}^{x_2} [\rho(x, t_2)u(x, t_2) - \rho(x, t_1)u(x, t_1)]\, dx = &-\int_{t_1}^{t_2} [\rho(x_2, t)u^2(x_2, t) - \rho(x_1, t)u^2(x_1, t)]\, dt \\ &-\int_{t_1}^{t_2} [p(x_2, t) - p(x_1, t)]\, dt,\end{aligned} \tag{2.22}$$

where $\rho(x, t)u(x, t)$ is the momentum per unit volume, $\rho(x, t)u^2(x, t)$ is the rate at which momentum flows past point x in the positive x direction and $p(x, t)$ is the pressure at point x and time t. Finally, the conservation of energy for the Euler equations states that the change in total energy in $[x_1, x_2]$ in time interval $[t_1, t_2]$ equals the energy flux through the boundaries of $[x_1, x_2]$ in time interval $[t_1, t_2]$ plus the energy change due to pressure on the boundaries of $[x_1, x_2]$. Stated mathematically as

$$\begin{aligned}\int_{x_1}^{x_2} [E(x, t_2) - E(x, t_1)]\, dx = &-\int_{t_1}^{t_2} [E(x_2, t)u(x_2, t) - E(x_1, t)u(x_1, t)]\, dt \\ &-\int_{t_1}^{t_2} [p(x_2, t)u(x_2, t) - p(x_1, t)u(x_1, t)]\, dt,\end{aligned} \tag{2.23}$$

where $E(x,t)$ is the energy density or energy per unit volume, $E(x,t)u(x,t)$ is the rate at which energy flows past point x and $p(x,t)u(x,t)$ is the energy change at x due to pressure. The formula for the energy density, $E(x,t)$, is the same formula that was used above when describing the differential form of the Euler equations and is given by Equation (2.4).

2.2.2 Deriving the Differential Form of the Euler Equations

The differential form of the conservation law can be derived from Equation (2.20) by assuming that $q(x,t)$ and $f(q(x,t))$ are differentiable functions, i.e that they are smooth. If $q(x,t)$ and $f(q(x,t))$ are smooth then

$$q(x,t_2) - q(x,t_1) = \int_{t_1}^{t_2} \frac{\partial}{\partial t} q(x,t)\, dt \tag{2.24}$$

and

$$f(q(x_2,t)) - f(q(x_1,t)) = \int_{x_1}^{x_2} \frac{\partial}{\partial x} f(q(x,t))\, dx. \tag{2.25}$$

Substituting these into Equation (2.20) gives

$$\int_{t_1}^{t_2} \int_{x_1}^{x_2} \left(\frac{\partial}{\partial t} q(x,t) + \frac{\partial}{\partial x} f(q(x,t)) \right) dx\, dt = 0. \tag{2.26}$$

Since this equation holds for any region $[x_1, x_2]$ and any time interval $[t_1, t_2]$, the integrand of the above equation must be equal to zero, that is

$$\frac{\partial}{\partial t} q(x,t) + \frac{\partial}{\partial x} f(q(x,t)) = 0. \tag{2.27}$$

Denoting partial derivatives in subscript notation, for example denoting the partial derivative of q with respect to t as q_t, the above equation becomes

$$q_t + f(q)_x = 0, \tag{2.28}$$

which is the differential form of the conservation law. Applying the above method to the conservation of mass, momentum and energy results in the differential form of the Euler equations

$$\rho_t + (\rho u)_x = 0, \tag{2.29}$$

$$(\rho u)_t + (\rho u^2 + p)_x = 0, \tag{2.30}$$

$$E_t + ((E + p)u)_x = 0. \tag{2.31}$$

2.2.3 Extension to Multi-dimensional Space

The integral form of the Euler equations can be extended to higher dimensional flows. In this case we consider a volume of fluid V in three-dimensional space and its surface S through which the fluxes pass and upon which the pressure acts. The conservation of a quantity, $q(\boldsymbol{r}, t)$, gives the following equation

$$\iiint_V [q(\boldsymbol{r}, t_2) - q(\boldsymbol{r}, t_1)]\, dV = -\int_{t_1}^{t_2} \iint_S \boldsymbol{F}(q(\boldsymbol{r}, t)) \cdot \boldsymbol{n}\, dS\, dt, \tag{2.32}$$

where $\boldsymbol{n}$ is the outward pointing unit normal vector of the surface element dS, $\boldsymbol{r}$ is the position vector and $\boldsymbol{F}(q(\boldsymbol{r}, t)) = (f(q), g(q), h(q))$. $\boldsymbol{F}(q(\boldsymbol{r}, t)) \cdot \boldsymbol{n}$ is therefore the rate at which the quantity q flows through the surface S at any point $\boldsymbol{r}$.

Conservation of mass, momentum and energy then gives the following three equations

$$\iiint_V [\rho(\boldsymbol{r}, t_2) - \rho(\boldsymbol{r}, t_1)]\, dV = -\int_{t_1}^{t_2} \iint_S [\rho \boldsymbol{u}] \cdot \boldsymbol{n}\, dS\, dt, \tag{2.33}$$

$$\iiint_V [\rho(\boldsymbol{r}, t_2)\boldsymbol{u}(\boldsymbol{r}, t_2) - \rho(\boldsymbol{r}, t_1)\boldsymbol{u}(\boldsymbol{r}, t_1)]\, dV = -\int_{t_1}^{t_2} \iint_S [\rho \boldsymbol{u} \otimes \boldsymbol{u} + p\boldsymbol{I}] \cdot \boldsymbol{n}\, dS\, dt, \tag{2.34}$$

$$\iiint_V [E(\boldsymbol{r}, t_2) - E(\boldsymbol{r}, t_1)]\, dV = -\int_{t_1}^{t_2} \iint_S [(E + p)\boldsymbol{u}] \cdot \boldsymbol{n}\, dS\, dt. \tag{2.35}$$

The differential form of the conservation law in multi-dimensional space can be

derived using the divergence theorem which is also known as Gauss' theorem. Gauss' theorem states that if $\boldsymbol{F}$ is a continuously differentiable vector field defined on a neighborhood of V, then the outward flux through the surface of V is equal to the triple integral of the divergence on the volume V. This can be stated mathematically as

$$\iiint_V (\nabla \cdot \boldsymbol{F})\, dV = \iint_S \boldsymbol{F} \cdot \boldsymbol{n}\, dS, \tag{2.36}$$

where the surface S is the boundary of the volume V. So when the function for a conserved quantity, $q(\boldsymbol{r}, t)$, is continuously differentiable we can make use of Gauss' theorem. Equation (2.32) then becomes

$$\iiint_V [q(\boldsymbol{r}, t_2) - q(\boldsymbol{r}, t_1)]\, dV = -\int_{t_1}^{t_2} \iiint_V \nabla \cdot \boldsymbol{F}(q(\boldsymbol{r}, t))\, dS\, dt. \tag{2.37}$$

Since

$$\nabla \cdot \boldsymbol{F}(q(\boldsymbol{r}, t)) = f(q)_x + g(q)_y + h(q)_z$$

when $\boldsymbol{r} = (x, y, z)$ and

$$q(\boldsymbol{r}, t_2) - q(\boldsymbol{r}, t_1) = \int_{t_1}^{t_2} \frac{\partial}{\partial t} q(\boldsymbol{r}, t)\, dt$$

when q is continuously differentiable, we have that

$$\int_{t_1}^{t_2} \iiint_V (q_t + f(q)_x + g(q)_y + h(q)_z)\, dV\, dt = 0,$$

and therefore

$$q_t + f(q)_x + g(q)_y + h(q)_z = 0. \tag{2.38}$$

When the above derivation is applied to the conservation of mass, the three

components of momentum, and energy, we obtain

$$\rho_t + (\rho u)_x + (\rho v)_y + (\rho w)_z = 0, \tag{2.39}$$

$$(\rho u)_t + (\rho u^2 + p)_x + (\rho uv)_y + (\rho uw)_z = 0, \tag{2.40}$$

$$(\rho v)_t + (\rho uv)_x + (\rho v^2 + p)_y + (\rho vw)_z = 0, \tag{2.41}$$

$$(\rho w)_t + (\rho uw)_x + (\rho vw)_y + (\rho w^2 + p)_z = 0, \tag{2.42}$$

$$E_t + ((E + p)u)_x + ((E + p)v)_y + ((E + p)w)_z = 0, \tag{2.43}$$

which is the differential form of the Euler equations in three dimensional space.

2.2.4 Other Useful Forms of the Euler Equations

We recall that the Euler equations can be written in their one dimensional conservative form as

$$\frac{\partial \boldsymbol{q}}{\partial t} + \frac{\partial \boldsymbol{f}}{\partial x} = 0, \tag{2.44}$$

where

$$\boldsymbol{q} = \begin{pmatrix} q_1 \\ q_2 \\ q_3 \end{pmatrix} = \begin{pmatrix} \rho \\ \rho u \\ E \end{pmatrix}, \tag{2.45}$$

and where, using the polytropic equation of state given in Equation (2.15),

$$\boldsymbol{f} = \begin{pmatrix} f_1 \\ f_2 \\ f_3 \end{pmatrix} = \begin{pmatrix} \rho u \\ \rho u^2 + p \\ (E + p)u \end{pmatrix} = \begin{pmatrix} q_2 \\ (\gamma - 1)q_3 + \left(\frac{3-\gamma}{2}\right)\frac{q_2^2}{q_1} \\ \gamma\frac{q_2 q_3}{q_1} - \left(\frac{\gamma-1}{2}\right)\frac{q_2^3}{q_1^2} \end{pmatrix}. \tag{2.46}$$

From this, through the use of the chain rule, we obtain

$$\frac{\partial \boldsymbol{q}}{\partial t} + A\frac{\partial \boldsymbol{q}}{\partial x} = 0, \tag{2.47}$$

where A is the Jacobian matrix of $\boldsymbol{f}$ so that

$$A(\boldsymbol{q}) = \frac{\partial \boldsymbol{f}(\boldsymbol{q})}{\partial \boldsymbol{q}} = \begin{bmatrix} \frac{\partial f_1}{\partial q_1} & \frac{\partial f_1}{\partial q_2} & \frac{\partial f_1}{\partial q_3} \\ \frac{\partial f_2}{\partial q_1} & \frac{\partial f_2}{\partial q_2} & \frac{\partial f_2}{\partial q_3} \\ \frac{\partial f_3}{\partial q_1} & \frac{\partial f_3}{\partial q_2} & \frac{\partial f_3}{\partial q_3} \end{bmatrix}$$

$$= \begin{bmatrix} 0 & 1 & 0 \\ -\left(\frac{3-\gamma}{2}\right)\frac{q_2^2}{q_1^2} & (3-\gamma)\frac{q_2}{q_1} & \gamma - 1 \\ -\gamma\frac{q_2 q_3}{q_1^2} + (\gamma-1)\frac{q_2^3}{q_1^3} & \gamma\frac{q_3}{q_1} - \left(\frac{3(\gamma-1)}{2}\right)\frac{q_2^2}{q_1^2} & \gamma\frac{q_2}{q_1} \end{bmatrix},$$

which finally leads to

$$A(\boldsymbol{q}) = \begin{bmatrix} 0 & 1 & 0 \\ \frac{1}{2}(\gamma-3)u^2 & (3-\gamma)u & \gamma - 1 \\ -\frac{\gamma u E}{\rho} + (\gamma-1)u^3 & \frac{\gamma E}{\rho} - \frac{3}{2}(\gamma-1)u^2 & \gamma u \end{bmatrix}. \tag{2.48}$$

The matrix A above is diagonalisable which means that the Euler equations are a hyperbolic system of equations and can be described by waves. Therefore, there is some matrix L such that

$$L^{-1}AL = \Lambda, \tag{2.49}$$

where Λ is a diagonal matrix whose entries are the three wave speeds given by the eigenvalues of A. The three eigenvalues of A are the roots of the characteristic polynomial

$$|A(\boldsymbol{q}) - \lambda I| = 0, \tag{2.50}$$

which are

$$\lambda_1 = u - c_s, \quad \lambda_2 = u, \quad \lambda_3 = u + c_s, \tag{2.51}$$

where c_s is the speed of sound in the fluid,

$$c_s = \sqrt{\frac{\gamma p}{\rho}}. \tag{2.52}$$

By using a change of variables

$$d\boldsymbol{v} = L^{-1} d\boldsymbol{q}, \tag{2.53}$$

we obtain the characteristic form of the Euler equations

$$\frac{\partial \boldsymbol{v}}{\partial t} + \Lambda \frac{\partial \boldsymbol{v}}{\partial x} = 0, \tag{2.54}$$

with

$$\Lambda = \begin{bmatrix} u - c_s & 0 & 0 \\ 0 & u & 0 \\ 0 & 0 & u + c_s \end{bmatrix}. \tag{2.55}$$

All information travels through the fluid at either the speed of the flow, u, or the speed of sound relative to the flow, $u \pm c_s$, except when waves from the same family interact with one another as in the case of shock waves discussed in Section 2.3.1. Therefore the domain of dependence and range of influence for each point in the x-t plane depend on these typical wave speeds and are shown in Figure 2.1.

The matrix L above is a matrix whose columns are the right eigenvectors of A, $\boldsymbol{r_i}$, and L^{-1} is a matrix whose rows are the left eigenvectors of A, $\boldsymbol{l_i}$. The right eigenvectors are solutions of $A\boldsymbol{r_i} = \lambda_i \boldsymbol{r_i}$ and are

$$\boldsymbol{r_1} = \begin{bmatrix} 1 \\ u - c_s \\ \frac{u^2}{2} + \frac{c_s^2}{\gamma - 1} - c_s u \end{bmatrix}, \quad \boldsymbol{r_2} = \begin{bmatrix} 1 \\ u \\ \frac{1}{2}u^2 \end{bmatrix}, \quad \boldsymbol{r_3} = \begin{bmatrix} 1 \\ u + c_s \\ \frac{u^2}{2} + \frac{c_s^2}{\gamma - 1} + c_s u \end{bmatrix}. \tag{2.56}$$

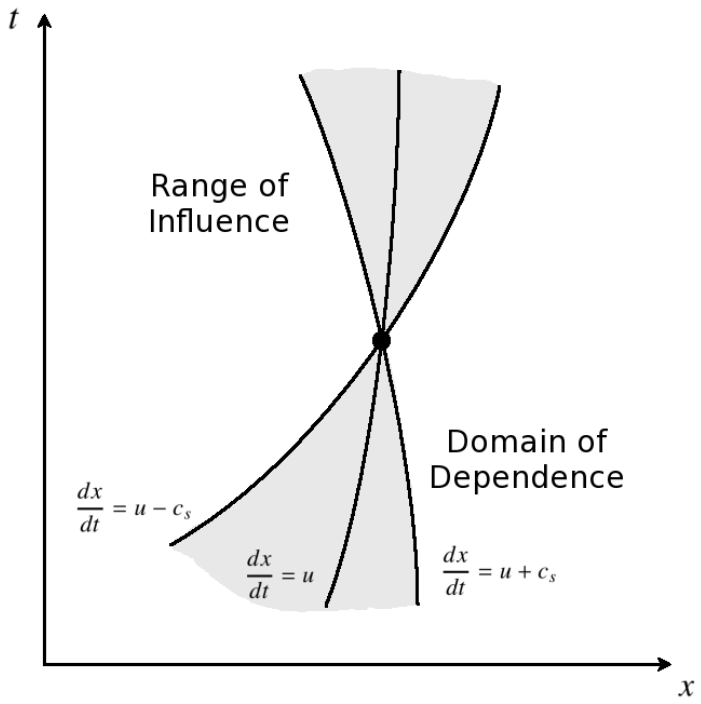

Figure 2.1: Diagram of the typical waves occurring in positive subsonic flow. For each point in the x-t plane these waves determine the range of influence and domain of dependence.

The left eigenvectors are solutions of $\boldsymbol{l_i}A = \lambda_i \boldsymbol{l_i}$ and are

$$\boldsymbol{l_1} = \begin{bmatrix} \frac{u^2}{2} + \frac{c_s u}{\gamma - 1}, & -u - \frac{c_s}{\gamma - 1}, & 1 \end{bmatrix}, \tag{2.57}$$

$$\boldsymbol{l_2} = \begin{bmatrix} \frac{u^2}{2} - \frac{c_s^2}{\gamma - 1}, & -u, & 1 \end{bmatrix}, \tag{2.58}$$

$$\boldsymbol{l_3} = \begin{bmatrix} \frac{u^2}{2} - \frac{c_s u}{\gamma - 1}, & -u + \frac{c_s}{\gamma - 1}, & 1 \end{bmatrix}. \tag{2.59}$$

Therefore

$$L = \begin{bmatrix} 1 & 1 & 1 \\ u - c_s & u & u + c_s \\ \frac{u^2}{2} + \frac{c_s^2}{\gamma - 1} - c_s u & \frac{1}{2}u^2 & \frac{u^2}{2} + \frac{c_s^2}{\gamma - 1} + c_s u \end{bmatrix} \tag{2.60}$$

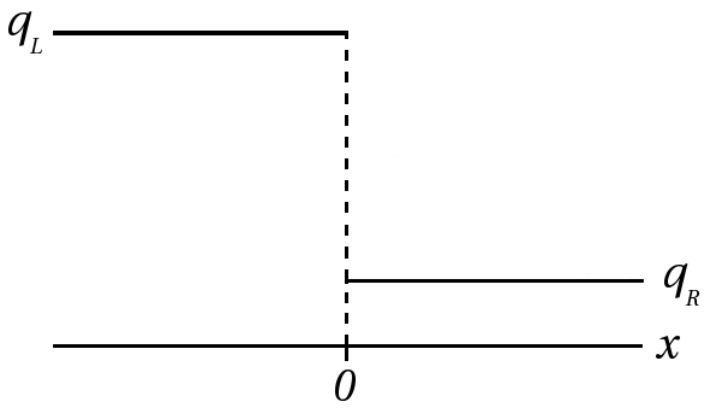

Figure 2.2: Initial conditions for the Riemann problem.

and

$$L^{-1} = \begin{bmatrix} \frac{u^2}{2} + \frac{c_s u}{\gamma - 1} & -u - \frac{c_s}{\gamma - 1} & 1 \\ \frac{u^2}{2} - \frac{c_s^2}{\gamma - 1} & -u & 1 \\ \frac{u^2}{2} - \frac{c_s u}{\gamma - 1} & -u + \frac{c_s}{\gamma - 1} & 1 \end{bmatrix}. \tag{2.61}$$

Using another change of variables we can also transform the conservative form of the equations into their primitive variable form expressed solely in terms of density, velocity and pressure.

$$\frac{\partial \boldsymbol{P}}{\partial t} + C \frac{\partial \boldsymbol{P}}{\partial x} = 0, \tag{2.62}$$

where

$$\boldsymbol{P} = \begin{pmatrix} \rho \\ u \\ p \end{pmatrix}, \quad C = \begin{bmatrix} u & \rho & 0 \\ 0 & u & \frac{1}{\rho} \\ 0 & \gamma p & u \end{bmatrix}.$$

When given in term of primitive variables the solution to the Riemann problem, as outlined in Section 2.3, is much simpler.

2.3 The Riemann Problem

The Riemann problem involves a conservation law

$$\frac{\partial q}{\partial t} + \frac{\partial f(q)}{\partial x} = 0, \tag{2.63}$$

along with the initial data

$$q(x,0) = \begin{cases} q_l, & x < 0, \\ q_r, & x > 0, \end{cases} \tag{2.64}$$

where q_l and q_r are constants. The Riemann problem is to find the solution to the above problem. It can be defined as the initial value problem for a system of conservation laws with no source terms, carried out in one dimensional space, and using piecewise constant data with two values for each variable separated by a single discontinuity, see Figure 2.2. Either side of the discontinuity the constant data extends to infinity.

The Riemann problem is a fundamental part of many numerical methods which often use an exact or approximate solution to the Riemann problem, many of these methods are based on a method proposed by Godunov (1959). An exact analytical solution to the Riemann problem can be found for any linear system of equations and, as we will see later, also for the nonlinear Euler equations. Solutions to the Riemann problem are self-similar which means that a knowledge of the solution at time t_0 is sufficient to obtain the solution for $t > t_0$ by using a suitable rescaling, i.e by stretching the solution in space. In this way the solution only depends on a single variable x/t rather than on x and t separately. Numerical methods using Riemann solvers require only the flux at $x = 0$, which is constant along the line $x = 0$, also by self-similarity. Approximate solutions to the Riemann problem are often used in numerical methods as these require less computational resources than the exact solutions while improving the wave capturing ability of the methods.

The solution to the Riemann problem for the Euler equations involves splitting the jump from q_l to q_r into a series of three jumps each of which propagates at

a particular speed λ_i. This can also be thought of as splitting the solution into three waves with corresponding wavespeeds of λ_i where each wave can be one of the following types of waves; rarefaction waves, shock waves or contact discontinuities. The jump in the p^{th} family, travelling at speed λ_p, is called the p-wave. Examples of rarefaction waves, shock waves and contact discontinuities are given in the following sections.

2.3.1 Shock Waves

The first type of wave is a shock wave or compression wave and it occurs when the wavespeed to the left of a discontinuity, λ_L is greater than the wavespeed to the right, λ_R. For example, consider Burgers equation, which obtained its name from Johannes Martinus Burgers (1895-1981) who studied this equation in connection with his work on velocity fluctuations in turbulent flows. Consider this equation in one dimensional space, where the flux function is given by $f(q) = \frac{1}{2}q^2$ which leads to the equation $q_t + qq_x = 0$, along with piecewise constant initial data

$$q(x,0) = \begin{cases} q_L & \text{if} x < 0, \\ q_R & \text{if} x > 0. \end{cases} \tag{2.65}$$

The solution when $q_L > q_R$ is the unique weak solution shown in Figure 2.3,

$$q(x,t) = \begin{cases} q_L & \text{if} x < st, \\ q_R & \text{if} x > st, \end{cases} \tag{2.66}$$

where

$$s = (q_L + q_R)/2 \tag{2.67}$$

is the speed of the shock wave, i.e the speed at which the discontinuity is propagating. The characteristics in both the left and right regions converge onto the shock. For the Euler equations the passing of a shock wave increases the pressure and density.

The speed of propagation of the discontinuity can be determined by conservation.

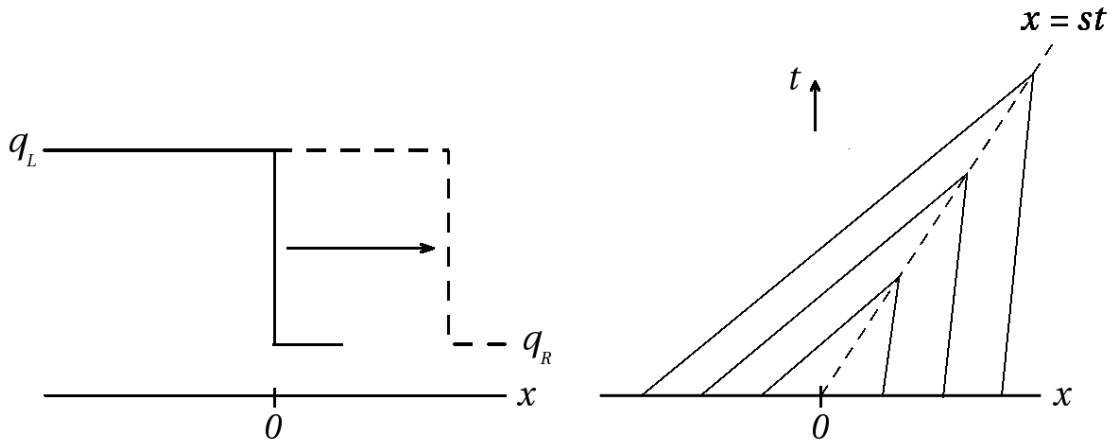

Figure 2.3: A shock wave

From conservation we have that

$$\int_{x_L}^{x_R} [q(x, t_N) - q(x, t_0)]\, dx = -\int_{t_0}^{t_N} [f(q(x_R, t)) - f(q(x_L, t))]\, dt, \tag{2.68}$$

from time t_0 to t_N and between the boundaries x_L and x_R. Figure 2.4 shows the boundaries of this region in space-time and also shows a discontinuity propagating at speed s. By referring to this figure, we can evaluate each side of the above equation as

$$\begin{aligned}
\int_{x_L}^{x_R} [q(x, t_N) - q(x, t_0)]\, dx &= \int_{x_L}^{x_R} q(x, t_N)\, dx - \int_{x_L}^{x_R} q(x, t_0)\, dx \\
&= [q_L(l_L + s(t_N - t_0)) + q_R(l_R - s(t_N - t_0))] - [q_L l_L + q_R l_R] \\
&= q_L s(t_N - t_0) - q_R s(t_N - t_0) \\
&= (q_L - q_R) s(t_N - t_0), \qquad (2.69)
\end{aligned}$$

where l_L, l_R and $s(t_N - t_0)$ correspond to distances as shown in Figure 2.4 and

$$\begin{aligned}
\int_{t_0}^{t_N} [f(q(x_R, t)) - f(q(x_L, t))]\, dt &= \int_{t_0}^{t_N} f(q(x_R, t))\, dt - \int_{t_0}^{t_N} f(q(x_L, t))\, dt \\
&= f(q_R)(t_N - t_0) - f(q_L)(t_N - t_0) \\
&= (f(q_R) - f(q_L))(t_N - t_0). \qquad (2.70)
\end{aligned}$$

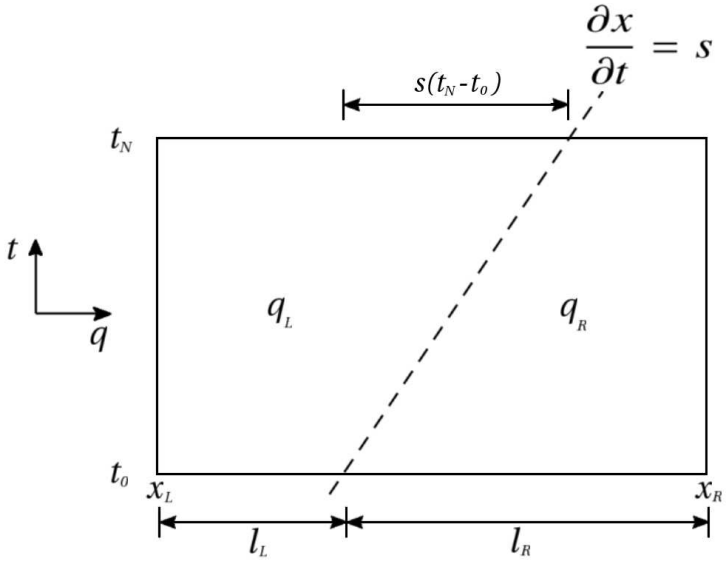

Figure 2.4: Discontinuity propagating at speed s in space-time

Substituting these back into Equation (2.68) we obtain a relation for the propagation speed of the discontinuity

$$s = \frac{f(q_L) - f(q_R)}{q_L - q_R}, \tag{2.71}$$

which is known as the Rankine-Hugoniot jump relation.

2.3.2 Rarefaction Waves

The second type of wave is a rarefaction wave and it occurs when the wavespeed to the left of a discontinuity, λ_L is less than the wavespeed to the right, λ_R. Considering Burgers equation again, there is more than one solution when $q_L < q_R$. One of these solutions is a propagating discontinuity of speed s but in this case the characteristics in both the left and right regions diverge away from the shock as can be seen in Figure 2.5. A second weak solution is a rarefaction wave, as shown in Figure 2.6, where

$$q(x,t) = \begin{cases} q_L & \text{if} \quad x < q_L t, \\ \dfrac{x}{t} & \text{if} \quad q_L t \leqslant x \leqslant q_R t, \\ q_R & \text{if} \quad x > q_R t. \end{cases} \tag{2.72}$$

In order to choose between these weak solutions we require that the correct weak solution also be the solution to the associated set of equations that include viscosity,

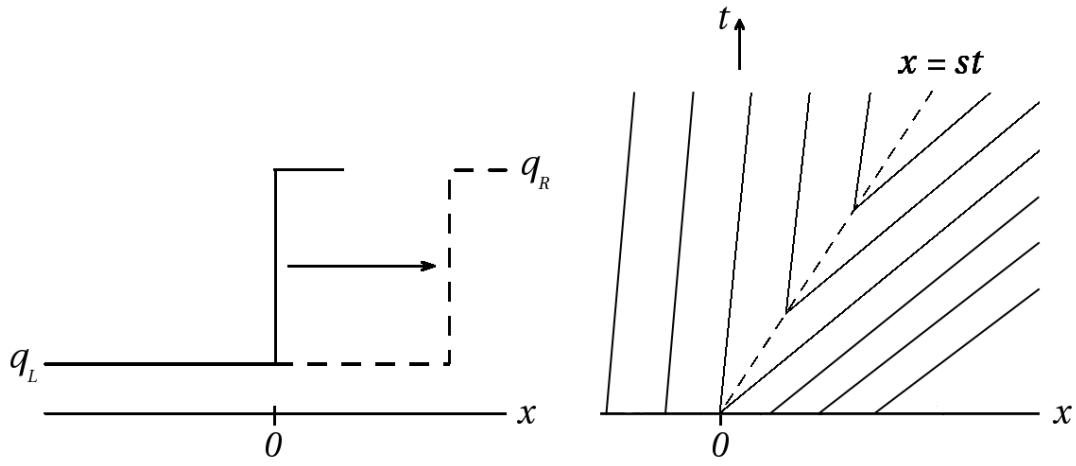

Figure 2.5: Entropy violating shock

in the limit as the viscosity tends to zero. This is called the vanishing viscosity solution and it is found that the rarefaction wave satisfies this requirement. The shock wave solution violates the second law of thermodynamics which requires the entropy following the fluid to neither increase nor decrease except at shocks. At shocks entropy must stay the same or increases following the fluid, or in this case across the shock. Solutions which satisfy the second law of thermodynamics are called entropy solutions. For Burgers equation the second law of thermodynamics is satisfied if $q_L > q_R$. For the above shock wave solution the opposite is true, so the shock solution is an entropy violating shock. For the Euler equations the second law of thermodynamics is satisfied if the wave speed just to the left of the shock is greater than the shock speed, which is, in turn, greater than the wave speed just to the right of the shock, i.e.

$$u_L + a_L > s > u_R + a_R \tag{2.73}$$

or

$$u_L - a_L > s > u_R - a_R. \tag{2.74}$$

Also, for the Euler equations, the passing of a rarefaction wave decreases the pressure and density. The boundary on the high-pressure side of the wave is called the head of the rarefaction while the boundary on the low-pressure side is called the tail.

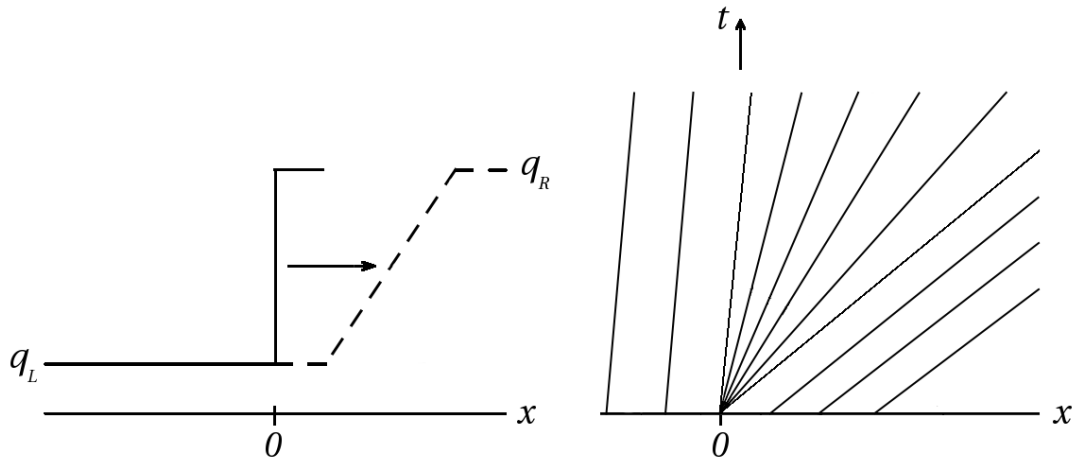

Figure 2.6: Rarefaction wave

2.3.3 Contact Discontinuities

For the Euler equations there is a third kind of wave called a contact discontinuity. Across a contact discontinuity the velcocity perpendicular to the surface of the contact discontinuity and the pressure remain constant while the remaining variables have discontinuities. This means the characteristics on either side of a contact discontinuity are parallel to each other. Since the velocity on both sides of a contact discontinuity are the same, fluid cannot pass through a contact discontinuity. The second law of thermodynamics requires entropy *following the fluid* to stay the same or increase across a shock, however since no fluid passes through a contact discontinuity this law does not apply across a contact discontinuity. Thus, entropy may change across a contact discontinuity but it is not created, i.e. a contact discontinuity separates regions of different entropy.

2.4 Numerical Methods

The physics of jets is highly non-linear and as a result of this complexity, the use of computational simulations is necessary. Many competing numerical methods are utilised in order to discretise and solve the hydrodynamic equations and hence advance the system in time and space. Four of the main classes of methods are spectral methods, finite element methods, finite difference methods and finite volume methods. A brief outline of each method is given below along with a more

detailed discussion of finite volume and finite difference methods. While spectral methods and finite element methods approximate or discretise the solution of the partial differential equations, finite difference methods discretise the partial differential equations themselves and finite volume methods discretise the integral form of these equations. As we shall see, many of the techniques used in finite difference methods can be adapted for application to finite volume methods.

2.4.1 Spectral Methods

Consider a partial differential equation of the form

$$Hq = f(x), \tag{2.75}$$

where H is the operator of the partial differential equation. For example in the case of the Poisson equation

$$H = \left(\frac{\partial^2}{\partial x^2} + \frac{\partial^2}{\partial y^2} \right). \tag{2.76}$$

In spectral methods it is assumed that the unknown, $q(x)$, can be approximated by a sum of $N+1$ basis functions, $\psi_n(x)$, usually sinusoids or Chebyshev polynomials, such that

$$q(x) \approx q_N(x) = \sum_{n=0}^{N} a_n \psi_n(x). \tag{2.77}$$

Substituting this series into the partial differential equations (2.75), along with a similar series approximation for the function f, we are left with a residual function

$$R(x, a_0, a_1, \ldots, a_n) = Hq_N - f. \tag{2.78}$$

In the case of the exact solution, $q(x)$, the residual function will be equal to zero everywhere. Therefore, the idea in spectral methods is to choose the series coefficients so that the residual function is minimised. One way of doing this is to choose a set of points, equal in number to the undetermined coefficients, and set the residual

function equal to zero at these points. This leaves a system of equations, equal in number to the undetermined coefficients and involving the coefficients of the terms in the series, that can be solved.

For a set of equations with a time-dependent component the coefficients of the terms in the series become time dependent and the original partial differential equations reduce to a set of ordinary differential equations in time, which can then be solved using a time-stepping method. It is also possible to solve the time-dependent equation in a purely spectral way by expanding the series in time as well as space but this can be computationally expensive and inefficient.

Since the spectral method involves a linear combination of continuous global functions it works best when the solution is smooth

2.4.2 Finite Element Methods

The spectral method and the finite element method are quite similar. The main difference between them is that the spectral method approximates the solution as a linear combination of continuous global functions that are generally nonzero over the entire domain of the solution while the finite element method splits the intervals into a number of subintervals and approximates the solution as a linear combination of local functions (usually piecewise continuous). By local we mean that they are nonzero only on small subdomains, of a couple of sub-intervals. So, the finite element method is a more general or localised approach to the global approach of the spectral method. Effectively the spectral method is a special case of the finite element method.

There are three common refinement methods for achieving more accurate finite element solutions. The first is to increase the number of elements, usually called h-refinement because h is the common symbol for the size or average size of a subinterval, thereby reducing the average size of a subinterval. The second is to employ higher-degree interpolation functions, usually called p-refinement, which is precisely the method employed in spectral methods. The third method, called r-refinement, is to implement an adaptive mesh by moving some of the nodes while

simultaneously maintaining the same number of elements as well as the degree of the interpolation functions. Finally there are combinations of the above methods, called hp-refinement.

Since the nodes can be moved, as in r-refinement above, finite element methods are useful when handling complex geometries and boundaries or even in cases where there is a moving boundary, for example the piston of a car engine. However this usefulness is reduced in computational fluid dynamics. This is because of the requirement for grids with large numbers of cells or gridpoints, in which the computational expense of the finite element and spectral methods becomes large.

2.4.3 Finite Difference Methods

In finite difference methods the idea is to discretise the partial differential equations and to replace the derivatives appearing in the equations by finite differences that approximate them. The derivative of a function f at a point x is defined as

$$f'(x) = \lim_{h \to 0} \frac{f(x+h) - f(x)}{h}. \tag{2.79}$$

Since a forward difference is an expression of the form $f(x+h) - f(x)$ we can see that the forward difference divided by h approximates the derivative when h is small. The error in this approximation can be derived from Taylor's theorem.

Consider the one-dimensional form of equation 2.1 assuming a constant velocity u

$$\frac{\partial \rho}{\partial t} + \boldsymbol{\nabla} \cdot [\rho u] = 0, \tag{2.80}$$

therefore

$$\frac{\partial \rho}{\partial t} + u \frac{\partial \rho}{\partial x} = 0. \tag{2.81}$$

The first step is to discretise the above equation on some geometric grid, in this case we use a uniform grid with a grid spacing of Δx as shown in Figure 2.7. Letting ρ_i^n

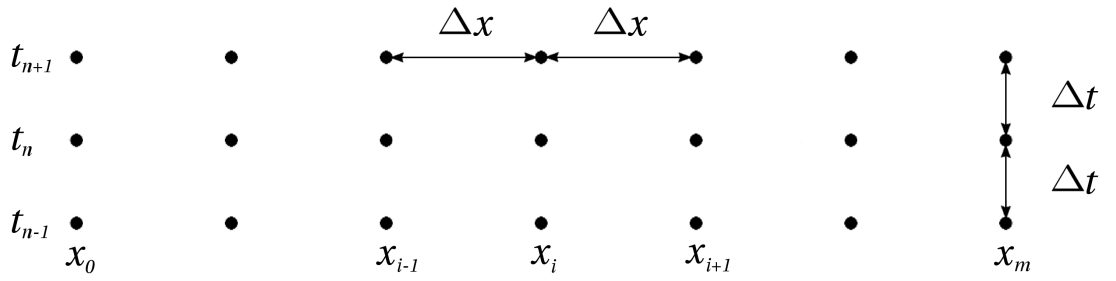

Figure 2.7: The partial differential equations under consideration are discretised on a geometric grid. A uniform grid with a grid spacing of Δx and a time step of Δt is shown here.

be an approximation of ρ at $x = x_i$ and time $t = t_n$ we can then use Taylor series expansions to obtain

$$\rho_{i+1}^n = \rho_i^n + \Delta x \left[\frac{\partial \rho}{\partial x}\right]_i^n + \frac{\Delta x^2}{2}\left[\frac{\partial^2 \rho}{\partial x^2}\right]_i^n + \frac{\Delta x^3}{6}\left[\frac{\partial^3 \rho}{\partial x^3}\right]_i^n + O(\Delta x^4), \tag{2.82}$$

$$\rho_{i-1}^n = \rho_i^n - \Delta x \left[\frac{\partial \rho}{\partial x}\right]_i^n + \frac{\Delta x^2}{2}\left[\frac{\partial^2 \rho}{\partial x^2}\right]_i^n - \frac{\Delta x^3}{6}\left[\frac{\partial^3 \rho}{\partial x^3}\right]_i^n + O(\Delta x^4). \tag{2.83}$$

Rearranging each of these equations we can approximate the first spatial derivative using

$$\left[\frac{\partial \rho}{\partial x}\right]_i^n = \frac{\rho_{i+1}^n - \rho_i^n}{\Delta x} + O(\Delta x), \qquad \text{(forward difference)} \tag{2.84}$$

$$= \frac{\rho_i^n - \rho_{i-1}^n}{\Delta x} + O(\Delta x). \qquad \text{(backward difference)} \tag{2.85}$$

The approximations are obtained by throwing away the error terms indicated by the O notation. By subtracting equations 2.82 and 2.83 and rearranging the terms we can also approximate the first spatial derivative as

$$\left[\frac{\partial \rho}{\partial x}\right]_i^n = \frac{\rho_{i+1}^n - \rho_{i-1}^n}{2\Delta x} + O(\Delta x^2). \qquad \text{(centred difference)} \tag{2.86}$$

Similarly we can approximate the first time derivative as

$$\left[\frac{\partial \rho}{\partial t}\right]_i^n = \frac{\rho_i^{n+1} - \rho_i^n}{\Delta t} + O(\Delta t), \qquad \text{(forward difference)} \tag{2.87}$$

$$= \frac{\rho_i^n - \rho_i^{n-1}}{\Delta t} + O(\Delta t), \qquad \text{(backward difference)} \tag{2.88}$$

$$= \frac{\rho_i^{n+1} - \rho_i^{n-1}}{2\Delta t} + O(\Delta t^2). \qquad \text{(centred difference)} \tag{2.89}$$

Discretisations of equation 2.81 can be obtained using the above approximations for the derivative terms. For example using a forward in time approximation (2.88) at time $t = t_n$ and a centred in space approximation (2.86) we obtain the discretisation

$$\frac{\partial \rho}{\partial t} + u\frac{\partial \rho}{\partial x} = \frac{\rho_i^{n+1} - \rho_i^n}{\Delta t} + u\frac{\rho_{i+1}^n - \rho_{i-1}^n}{2\Delta x} + O(\Delta t, \Delta x^2) = 0. \tag{2.90}$$

This rearranges to become

$$\rho_i^{n+1} \approx \rho_i^n - \frac{u\Delta t}{2\Delta x}\left[\rho_{i+1}^n - \rho_{i-1}^n\right]. \tag{2.91}$$

This type of scheme is called an explicit scheme. Once the values ρ_i^n are known across the whole spatial grid we can advance the solution forward in time using equation 2.91 to obtain the values for the variable at the next time step $t = t_{n+1}$. The stability of this scheme is discussed in the next section below and in the section on von Neumann Analysis.

On the other hand, if we use use a backward in time approximation at time $t = t_{n+1}$ and a centred in space approximation (2.86) we obtain the discretisation

$$\frac{\partial \rho}{\partial t} + u\frac{\partial \rho}{\partial x} = \frac{\rho_i^{n+1} - \rho_i^n}{\Delta t} + u\frac{\rho_{i+1}^{n+1} - \rho_{i-1}^{n+1}}{2\Delta x} + O(\Delta t, \Delta x^2) = 0. \tag{2.92}$$

This rearranges to become

$$\rho_i^{n+1} \approx \rho_i^n - \frac{u\Delta t}{2\Delta x}\left[\rho_{i+1}^{n+1} - \rho_{i-1}^{n+1}\right] \tag{2.93}$$

We note that the value for ρ_i^{n+1} depends on the adjacent spatial values at the

new time, $t = t_{n+1}$. Therefore ρ_i^{n+1} must be solved for simultaneously with its adjacent spatial values, ρ_{i+1}^{n+1} and ρ_{i-1}^{n+1}, and hence all spatial values must be solved for simultaneously. This type of scheme is called an implicit scheme. Consequently, we can obtain ρ_i^{n+1} from solving the system of linear equations

$$\rho_i^{n+1} + \frac{u\Delta t}{2\Delta x}\left[\rho_{i+1}^{n+1} - \rho_{i-1}^{n+1}\right] = \rho_i^n. \tag{2.94}$$

Equation 2.94 can be rewritten as

$$a\rho_{i-1}^{n+1} + b\rho_i^{n+1} + c\rho_{i+1}^{n+1} = \rho_i^n, \tag{2.95}$$

where

$$a = -\frac{u\Delta t}{2\Delta x}, \quad b = 1, \quad c = \frac{u\Delta t}{2\Delta x}.$$

The above equation (2.95) can be rewritten in matrix form,

$$A\boldsymbol{\rho^{n+1}} = \boldsymbol{b^n}, \tag{2.96}$$

by defining an $(M-1)\times(M-1)$ matrix A

$$A = \begin{bmatrix} b & c & 0 & \cdots & & \cdots & & & 0 \\ a & b & c & 0 & \cdots & & \cdots & & \vdots \\ 0 & a & b & c & 0 & \cdots & & \cdots & 0 \\ \vdots & & \ddots & \ddots & \ddots & & & & \vdots \\ 0 & \cdots & 0 & a & b & c & 0 & \cdots & 0 \\ \vdots & & & & \ddots & \ddots & \ddots & & \vdots \\ 0 & \cdots & & \cdots & 0 & a & b & c & 0 \\ \vdots & & \cdots & & \cdots & 0 & a & b & c \\ 0 & & & \cdots & & \cdots & 0 & a & b \end{bmatrix},$$

where M is the number of intervals in the grid and hence $M+1$ is the number of

grid points, by defining an $(M-1)$ vector $\boldsymbol{\rho^{n+1}}$

$$\boldsymbol{\rho^{n+1}} = \begin{bmatrix} \rho_1^{n+1} \\ \rho_2^{n+1} \\ \vdots \\ \rho_{m-1}^{n+1} \end{bmatrix},$$

and by defining an $(M-1)$ vector $\boldsymbol{b^n}$

$$\boldsymbol{b^n} = \begin{bmatrix} \rho_1^n - a\rho_0^{n+1} \\ \rho_2^n \\ \vdots \\ \rho_{m-2}^n \\ \rho_{m-1}^n - c\rho_m^{n+1} \end{bmatrix},$$

where ρ_0^{n+1} and ρ_m^{n+1} are defined by the boundary conditions. Thus, given $\boldsymbol{\rho^n}$, we can calculate $\boldsymbol{b^n}$ using the boundary conditions and then solve (2.96) to obtain $\boldsymbol{\rho^{n+1}}$ using

$$\boldsymbol{\rho^{n+1}} = A^{-1}\boldsymbol{b^n}. \tag{2.97}$$

The stability of this scheme is discussed in the next section below.

Convergence and Stability

When constructing a numerical scheme the goal is to construct a scheme that converges, that is a scheme that approaches the true solution of the PDE when the mesh width, h, tends to zero. Lax's Equivalence Theorem states that, for a consistent scheme, stability is a necessary and sufficient condition for convergence. A scheme is said to be consistent with the PDE being discretised if the local truncation error tends to zero as the mesh size tends to zero

$$L_{\text{TE}} \to 0 \quad \text{as} \quad \Delta t \to 0 \quad \text{and} \quad \Delta x \to 0. \tag{2.98}$$

There are many different definitions of stability and instability. Assuming consistency, one interpretation of numerical instability is that of unbounded growth whereby a method is unstable if the error grows to infinity as time goes to infinity. Another stricter interpretation defines a stable scheme as one that does not magnify approximation errors and doesn't have local errors significantly larger than the average error. Regardless of the definition the aim is to control the spurious oscillations that are a common sign of instability.

Similar to the definitions of stability, there are many prescribed conditions for ascertaining whether a scheme is stable or not, some of which are stricter than others. One condition that is necessary for stability, but not sufficient, is the Courant-Friedrichs-Lewy (CFL) condition. It states that the full numerical domain of dependence must contain the physical domain of dependence of the equations being solved. A scheme that violates this condition might be missing important information and hence deviate from the true solution. The physical domain of dependence is determined by the wave speeds as can be seen in Figure 2.1, while the numerical domain of dependence is determined by the stencil of the scheme. In turn, a schemes' stencil depends on the mesh width, the size of the time step and on the scheme used. For a particular scheme, with a particular mesh, the CFL condition can often be satisfied by carefully choosing the size of the time step.

Since unstable solutions typically oscillate, one approach for determining a schemes stability is to express the solution as the sum of oscillating trigonometric functions, i.e. as a Fourier series. This approach is discussed in more detail in Section 2.4.4 below, where a linear stability analysis method called von Neumann analysis is outlined. Stricter non-linear methods also exist, one of which leads to the total variation bounded (TVB) condition which requires that the total amount of oscillation as measured by the total variation remains bounded. If we define the total variation of a quantity Q on a grid as

$$TV(Q^n) = \sum_{i=-\infty}^{\infty} |Q_{i+1}^n - Q_i^n|, \tag{2.99}$$

then a scheme that satisfies the TVB condition must satisfy the following

$$TV(Q^n) \leqslant M \leqslant \infty \tag{2.100}$$

for all n and for some constant M. Even stricter again, the total variation diminishing (TVD) condition, first introduced by Harten (1983), requires that the total variation is reduced or remains constant at each time step. Therefore, a scheme that satisfies the TVD condition must satisfy the following

$$TV(Q^{n+1}) \leqslant TV(Q^n). \tag{2.101}$$

TVD methods typically achieve non-linear stability through the use of flux-averaging, which is discussed in more detail below. As we shall see, the freedom of flux-averaging allows one to enforce the TVD condition.

The stability of the explicit scheme defined in Equation (2.91) is determined in the section below on von Neumann Analysis. This scheme will always be unstable, regardless of any condition that's put on the time step, i.e. it's unconditionally unstable. The implicit scheme defined in Equation (2.94) is always numerically stable and convergent but usually more computationally intensive than the explicit method as it requires solving a system of numerical equations on each time step.

2.4.4 Finite Volume Methods

Finite volume methods discretise the integral form of the partial differential equations. Similar to the finite difference method a meshed geometry is used, but in this case the mesh is a mesh of cells rather than points. This means that each cell in the meshed geometry actually corresponds to a particular volume, hence the term "Finite volume". The values of the variables in a particular cell are then taken as the average values over the volume of that cell and hence can be called cell averages. The surface integrals in the integral form of the partial differential equations are then evaluated as fluxes at the surfaces of each finite volume. Because the flux entering a given volume is identical to that leaving the adjacent volume, these methods

are conservative. Another advantage of the finite volume method is that it is easily formulated to allow for unstructured meshes.

Consider Equation (2.20) that describes the conservation law for a conserved quantity, $q(x,t)$. Using the uniform meshed geometry shown in Figure 2.7 and by defining Q_i^n to be the average value of the conserved quantity at time t_n between $x_{i-1/2}$ and $x_{i+1/2}$, the locations of the upstream and downstream edges of the i^{th} cell, we have that

$$Q_i^n = \frac{1}{\Delta x} \int_{x_{i-\frac{1}{2}}}^{x_{i+\frac{1}{2}}} q(x,t_n)\,dx. \tag{2.102}$$

Defining $F_{i\pm1/2}^n$ to be the average flux of the conserved quantity across the boundaries $x = x_{i\pm1/2}$ between time t_n and t_{n+1} we have that

$$F_{i\pm1/2}^n = \frac{1}{\Delta t} \int_{t_n}^{t_{n+1}} f(q(x_{i\pm1/2},t))\,dt. \tag{2.103}$$

Rearranging the above equations we have

$$\int_{x_{i-\frac{1}{2}}}^{x_{i+\frac{1}{2}}} q(x,t_n)\,dx = \Delta x Q_i^n,$$

$$\int_{t_n}^{t_{n+1}} f(q(x_{i\pm1/2},t))\,dt = \Delta t F_{i\pm1/2}^n,$$

which when substituted into Equation (2.20) and rearranged gives the formula

$$Q_i^{n+1} = Q_i^n - \frac{\Delta t}{\Delta x}\left[F_{i+1/2}^n - F_{i-1/2}^n\right]. \tag{2.104}$$

This is an exact relation but by approximating the average flux across the boundaries, $F_{i\pm1/2}^n$, we can interpret this formula approximately in each cell of the discretised domain. There are many ways of prescribing the numerical flux and the choice of this prescription will determine the specific method obtained.

FTCS Scheme

One of the simplest choices for the numerical flux gives a forward in time centred in space scheme (FTCS). The flux is approximated by

$$F^n_{i+1/2} \approx \frac{1}{2}\left[F(Q^n_i) + F(Q^n_{i+1})\right], \tag{2.105}$$

where

$$F(Q^n_i) = u^n_i Q^n_i, \tag{2.106}$$

and leads to the scheme

$$Q^{n+1}_i \approx Q^n_i - \frac{1}{2}\frac{\Delta t}{\Delta x}\left[F(Q^n_{i+1}) - F(Q^n_{i-1})\right]. \tag{2.107}$$

Von Neumann Analysis

When analysing the stability of this scheme a method called von Neumann analysis can be utilised. The idea is to perform a spatial Fourier transform along all spatial dimensions, in order to produce a Fourier decomposition of the scheme's error. We consider the time evolution of a single Fourier mode of wave-number k, $Q(x,t) = T(t)e^{ik\theta}$, where i is the complex number, $i = \sqrt{-1}$. Substituting a trial solution of $Q^n_k = T^n e^{ik\theta}$ into the equation for the scheme and setting

$$c = \frac{u\Delta t}{\Delta x} \tag{2.108}$$

yields

$$T^{n+1}e^{ik\theta} = T^n e^{ik\theta} - \frac{1}{2}c\left[T^n e^{i(k+1)\theta} - T^n e^{i(k-1)\theta}\right], \tag{2.109}$$

which reduces to

$$T^{n+1} = AT^n, \tag{2.110}$$

where

$$\begin{aligned} A &= 1 - \frac{1}{2}c\left[e^{i\theta} - e^{-i\theta}\right] \\ &= 1 - \frac{1}{2}c\left[2i\sin\theta\right] \\ &= 1 - ic\sin\theta. \end{aligned} \tag{2.111}$$

Thus, the amplitude of the Fourier mode is amplified by a factor A at each time-step. In order for a scheme to be stable, the modulus of this amplification factor must be less than one for all possible values of k. In this case that results in the requirement that

$$|A|^2 = 1 + c^2\sin^2\theta \leqslant 1, \tag{2.112}$$

which is clearly never satisfied. Therefore, the FTCS method will always be unstable, regardless of any condition that's put on the time step, i.e. it's unconditionally unstable.

The Lax-Friedrichs Scheme

Choosing a flux approximation of

$$F^n_{i+1/2} \approx \frac{1}{2}\left[F(Q^n_{i+1}) + F(Q^n_i)\right] - \frac{1}{2}\frac{\Delta x}{\Delta t}\left(Q^n_{i+1} - Q^n_i\right) \tag{2.113}$$

leads to the Lax-Friedrichs Scheme

$$Q^{n+1}_i \approx \frac{1}{2}\left(Q^n_{i+1} + Q^n_{i-1}\right) - \frac{1}{2}\frac{\Delta t}{\Delta x}\left[F(Q^n_{i+1}) - F(Q^n_{i-1})\right]. \tag{2.114}$$

This scheme is conditionally stable when $|c| \leqslant 1$

The Lax-Wendroff Scheme

Choosing a flux approximation of

$$F^n_{i+1/2} \approx \frac{1}{2}\left[F(Q^n_{i+1}) + F(Q^n_i)\right] - \frac{1}{2}\frac{\Delta t}{\Delta x}u(Q^n_{i+1/2})\left[F(Q^n_{i+1}) - F(Q^n_i)\right] \tag{2.115}$$

$$\approx \frac{1}{2}\left[F(Q^n_{i+1}) + F(Q^n_i)\right] - \frac{1}{2}\frac{\Delta t}{\Delta x}u^2(Q^n_{i+1/2})\left[Q^n_{i+1} - Q^n_i\right] \tag{2.116}$$

leads to the Lax Wendroff scheme

$$Q^{n+1}_i \approx Q^n_i - \frac{1}{2}\frac{\Delta t}{\Delta x}\left[F(Q^n_{i+1}) - F(Q^n_{i-1})\right] + \frac{1}{2}\left(\frac{\Delta t}{\Delta x}\right)^2\left[u(Q^n_{i+1/2})\left[F(Q^n_{i+1}) - F(Q^n_i)\right] - u(Q^n_{i-1/2})\left[F(Q^n_i) - F(Q^n_{i-1})\right]\right] \tag{2.117}$$

$$\approx Q^n_i - \frac{1}{2}\frac{\Delta t}{\Delta x}\left[F(Q^n_{i+1}) - F(Q^n_{i-1})\right] + \frac{1}{2}\left(\frac{\Delta t}{\Delta x}\right)^2\left[u^2(Q^n_{i+1/2})\left[Q^n_{i+1} - Q^n_i\right] - u^2(Q^n_{i-1/2})\left[Q^n_i - Q^n_{i-1}\right]\right], \tag{2.118}$$

where $u(Q^n_{i+1/2})$ is the average speed for the cell centred on $x_{i+1/2}$ at time t_n.

$$u(Q^n_{i+1/2}) = \frac{\partial F(Q^n_{i+1/2})}{\partial Q^n_{i+1/2}} \tag{2.119}$$

and can be approximated in several different ways such as

$$u(Q^n_{i+1/2}) \approx \frac{u^n_{i+1} + u^n_i}{2} \tag{2.120}$$

or

$$u(Q^n_{i+1/2}) \approx \begin{cases} \frac{F(Q^n_{i+1}) - F(Q^n_i)}{Q^n_{i+1} - Q^n_i} & \text{for} \quad Q^n_i \neq Q^n_{i+1}, \\ u(Q^n_i) & \text{for} \quad Q^n_i = Q^n_{i+1}, \end{cases}$$

$$= \begin{cases} \frac{u^n_{i+1}Q^n_{i+1} - u^n_i Q^n_i}{Q^n_{i+1} - Q^n_i} & \text{for} \quad Q^n_i \neq Q^n_{i+1}, \\ u(Q^n_i) & \text{for} \quad Q^n_i = Q^n_{i+1}. \end{cases} \tag{2.121}$$

This scheme becomes a little more complicated when considering a system of m conserved quantities like the Euler equations, it becomes

$$\begin{aligned}\boldsymbol{Q}_i^{n+1} \approx \boldsymbol{Q}_i^n &- \frac{1}{2}\frac{\Delta t}{\Delta x}\left[\boldsymbol{F}(\boldsymbol{Q}_{i+1}^n) - \boldsymbol{F}(\boldsymbol{Q}_{i-1}^n)\right] \\ &+ \frac{1}{2}\left(\frac{\Delta t}{\Delta x}\right)^2 \left[A^2(\boldsymbol{Q}_{i+1/2}^n)\left[\boldsymbol{Q}_{i+1}^n - \boldsymbol{Q}_i^n\right] - A^2(\boldsymbol{Q}_{i-1/2}^n)\left[\boldsymbol{Q}_i^n - \boldsymbol{Q}_{i-1}^n\right]\right] \quad (2.122)\end{aligned}$$

where A is the Jacobian matrix of $\boldsymbol{F}$

$$A(\boldsymbol{Q}) = \frac{\partial \boldsymbol{F}(\boldsymbol{Q})}{\partial \boldsymbol{Q}} = \begin{bmatrix} \frac{\partial F_1}{\partial Q_1} & \cdots & \frac{\partial F_1}{\partial Q_m} \\ \vdots & \ddots & \vdots \\ \frac{\partial F_m}{\partial Q_1} & \cdots & \frac{\partial F_m}{\partial Q_m} \end{bmatrix}. \quad (2.123)$$

This scheme is conditionally stable when $0 \leqslant |c| \leqslant 1$ and is second order accurate in time as well as space. It is only slightly diffusive but is quite dispersive and thus is highly susceptible to non-linear instabilities.

The Two-Step Lax-Wendroff Scheme

Evaluating the Jacobian matrix in the Lax-Wendroff Scheme can be computationally expensive so by using a two-step approach this complication can be avoided. Choosing a flux approximation of

$$F_{i+1/2}^n \approx F(Q_{i+1/2}^{n+1/2}), \quad (2.124)$$

where

$$Q_{i+1/2}^{n+1/2} \approx \frac{1}{2}\left[Q_{i+1}^n + Q_i^n\right] - \frac{1}{2}\frac{\Delta t}{\Delta x}\left[F(Q_{i+1}^n) - F(Q_i^n)\right], \quad (2.125)$$

leads to the two-step Lax-Wendroff scheme

$$Q_i^{n+1} \approx Q_i^n - \frac{\Delta t}{\Delta x}\left[F(Q_{i+1/2}^{n+1/2}) - F(Q_{i-1/2}^{n+1/2})\right]. \quad (2.126)$$

The first step in this method steps to time $t_{n+1/2}$ from time t_n and calculates $Q_{i+1/2}^{n+1/2}$ by mapping the conserved quantities on the original mesh, x_i, onto a new mesh, $x_{i+1/2}$, in which the new cells are centred on the boundaries of the original cells. One should note that the calculation of $Q_{i+1/2}^{n+1/2}$ is actually the Lax-Friedrichs scheme (2.114) but using a half step in time along with a half step in space that's centred around $x_{i+1/2}$. The new values for the conserved quantities, $Q_{i+1/2}^{n+1/2}$, can then be used in the second step of this method to approximate the fluxes across the boundaries of the original cells, $F_{i+1/2}^{n}$.

Godunov Schemes

Godunov's method uses a Riemann solver to approximate the conserved quantities $Q_{i+1/2}^{\mathrm{RIE}}$ at each cell interface, $x_{i+1/2}$, and then uses this to obtain a flux approximation that is given by

$$F_{i+1/2}^{n} \approx F(Q_{i+1/2}^{\mathrm{RIE}}). \tag{2.127}$$

Using the conservation equation (2.104) this results in the scheme

$$Q_i^{n+1} \approx Q_i^n - \frac{\Delta t}{\Delta x}\left[F(Q_{i+1/2}^{\mathrm{RIE}}) - F(Q_{i-1/2}^{\mathrm{RIE}})\right]. \tag{2.128}$$

This method is valid for linear systems as well as non-linear systems as long as the non-linear Riemann problem can be solved at the cell interfaces.

Stability analysis of the Godunov scheme gives us the condition

$$|A|^2 = (1-c)^2 + 2c(1-c)\cos\theta + c^2 \leqslant 1, \tag{2.129}$$

which becomes

$$0 \leqslant c \leqslant 1, \tag{2.130}$$

which is the same as the result obtained based on the CFL condition for Godunov schemes. For the Euler equations the CFL condition becomes equivalent to ensuring

that no waves from the Riemann problem can travel a distance of more than one cell in one time-step. The condition gives us the Courant number, C, and requires that

$$C = \frac{s_{\max}\Delta t}{\Delta x} \leqslant 1, \tag{2.131}$$

where $s_{\max} = \max_{\text{grid}}(|\boldsymbol{u}| + c_s)$ is the maximum wave speed over the entire grid, $|\boldsymbol{u}|$ is the fluid velocity and c_s is the local speed of sound in the fluid.

Flux Averaging, Limiting and Correcting

Flux averaging is a technique commonly used to avoid the difficulties that often occur around regions with strong gradients. It consists of using two or more established methods where, in an extreme case, one method is chosen in smooth regions and another method is chosen near shocks. In a less extreme case, an average of the two methods is chosen where the weighting, or averaging factor, given to each method is chosen in order to damp spurious oscillations and enforce non-linear stability conditions, typically to satisfy the TVD condition. This is achieved by setting the averaging factor so that in smooth regions greater emphasis is given to a method that works well in smooth regions while near shocks greater emphasis is given to a method that works well near shocks. The ratios of divided differences are used to decide how close to a shock we are. In a flux-averaged method the conservative flux can be written as

$$F^n_{i+1/2} = \text{avg}^{\,n}_{i+1/2}(F^{(1)}_{i+1/2}, F^{(2)}_{i+1/2}), \tag{2.132}$$

where $\text{avg}^{\,n}_{i+1/2}$ is any averaging function. $F^{(1)}_{i+1/2}$ and $F^{(2)}_{i+1/2}$ are the conservative numerical fluxes of two different methods, one often a first order method and the other often a second order method. This method is usually referred to as flux averaging for finite-difference schemes and flux limiting for finite-volume schemes.

In the context of flux-limited methods the averaging function is written as

$$F^n_{i+1/2} = \text{avg}^{\,n}_{i+1/2}(F^{(1)}_{i+1/2}, F^{(2)}_{i+1/2}) = F^{(1)}_{i+1/2} + \phi^n_{i+1/2}(F^{(2)}_{i+1/2} - F^{(1)}_{i+1/2}), \tag{2.133}$$

where the averaging parameter, $\phi^n_{i+1/2}$, is referred to as the flux limiter. We define $\phi^n_{i+1/2}$ to be

$$\phi^n_{i+1/2} = \phi(\theta), \tag{2.134}$$

where ϕ is now a function which determines the flux limiter and θ is the upwind difference ratio such that

$$\theta = \begin{cases} \frac{Q^n_i - Q^n_{i-1}}{Q^n_{i+1} - Q^n_i} & \text{if} \quad u^n_{i+1/2} > 0, \\ \frac{Q^n_{i+2} - Q^n_{i+1}}{Q^n_{i+1} - Q^n_i} & \text{if} \quad u^n_{i+1/2} < 0. \end{cases} \tag{2.135}$$

There is a range of different functions, ϕ, that can be chosen in order to determine the flux limiter. One choice gives the minmod flux limiter and is defined as

$$\phi(\theta) = \text{minmod}\,(1, \theta) = \begin{cases} 1 & \text{if} \quad \theta \geqslant 1, \\ \theta & \text{if} \quad 0 < \theta < 1, \\ 0 & \text{if} \quad \theta \leqslant 0. \end{cases} \tag{2.136}$$

Another choice gives the superbee limiter and is defined as

$$\phi(\theta) = \max\,(0, \min(2\theta, 1), \min(\theta, 2)) = \begin{cases} 0 & \text{if} \quad \theta \leqslant 0, \\ 2\theta & \text{if} \quad 0 \leqslant \theta \leqslant \frac{1}{2}, \\ 1 & \text{if} \quad \frac{1}{2} \leqslant \theta \leqslant 1, \\ \theta & \text{if} \quad 1 \leqslant \theta \leqslant 2, \\ 2 & \text{if} \quad \theta \geqslant 2. \end{cases} \tag{2.137}$$

A third choice gives the van Leer limiter and is defined as

$$\phi(\theta) = \text{av}(1, \theta) \begin{cases} \frac{2\theta}{1+\theta} & \text{if} \quad \theta \geqslant 0, \\ 0 & \text{if} \quad \theta < 0, \end{cases} \tag{2.138}$$

where the function av of two arguments is the non-linear averaging function given in van Leer (1977)

$$\mathrm{av}(a,b) = \begin{cases} \frac{2ab}{a+b} & \text{if } ab > 0, \\ 0 & \text{otherwise.} \end{cases} \tag{2.139}$$

In flux-correction methods the averaging function is replaced by a differencing function so that

$$F^n_{i+1/2} = F^{(1)}_{i+1/2} + \mathrm{diff}\,^n_{i+1/2}(F^{(1)}_{i+1/2}, F^{(2)}_{i+1/2}), \tag{2.140}$$

where the differencing function $\mathrm{diff}\,^n_{i+1/2}(F^{(1)}_{i+1/2}, F^{(2)}_{i+1/2})$ is called a flux correction. Whereas flux-limited methods average two methods, flux-corrected methods alter one method to make it more like another method. In flux-corrected methods the second method usually has less artificial viscosity than the first, therefore the flux correction is antidissipative. A common example of a flux-correction method is the flux-corrected transport (FCT) method developed by Boris & Book (1973).

Flux Splitting

Some methods combine flux averaging, as described in the section above, with flux splitting, using flux averaging to avoid the difficulties that often occur around regions with strong gradients and using flux splitting to ensure that the method is an upwinded method and satisfies the CFL condition. Flux splitting involves splitting the flux so that right-going waves cause flux f^+ and left-going waves cause flux f^- such that

$$f(q) = f^+(q) + f^-(q) \tag{2.141}$$

and

$$\frac{df^+}{dq} \geqslant 0, \qquad \frac{df^-}{dq} \leqslant 0. \tag{2.142}$$

The conservation equation for q in flux split form is then

$$\frac{\partial q}{\partial t} + \frac{\partial f^+}{\partial q} + \frac{\partial f^-}{\partial q} = 0, \tag{2.143}$$

where $\partial f^+/\partial q$ can be discretised using one method and $\partial f^-/\partial q$ can be discretised using another method. The methods can be chosen to ensure that the CFL condition is satisfied. Defining the flux at the interface between two cells as

$$f_{i+1/2} = f^+(q_i) + f^-(q_{i+1}) \tag{2.144}$$

leads to a first-order upwind method. Two examples of flux-split methods are described in Steger & Warming (1981) and Liou & Steffen (1993).

2.5 Numerical Methods Used For This Work

This section outlines the specifics of the scheme used in this work. The numerical method that is chosen to integrate the hydrodynamical equations mentioned above, needs to be able to satisfactorily resolve the strong shocks that can occur in these types of fluid flows. In particular, the method used in this work is a MUSCL-type scheme (van Leer, 1977; Falle, 1991) that is described in Downes & Ray (1999) and is second order accurate in space and time.

The code is solved on a 2D or 3D grid. Each grid point defines the physical conditions for a particular region or cell. The physical conditions of two neighbouring cells or grid points are joined by a discontinuity at the cell interface. The code uses a linear Riemann solver to obtain suitable values for the physical conditions at the interface except where the resolved pressure differs either from the left or right state at the cell interface by greater than 10% where it uses a non-linear Riemann solver. The code also takes account of cooling due to ionisation and radiative atomic transitions. The details of the changes to the equations from Section (2.2) caused by these additions, are given in Section 2.5.1 below.

2.5.1 The Equations

The equations solved are

$$\frac{\partial \rho}{\partial t} = -\boldsymbol{\nabla} \cdot [\rho \boldsymbol{u}], \tag{2.145}$$

$$\frac{\partial (\rho \boldsymbol{u})}{\partial t} = -\boldsymbol{\nabla} \cdot [\rho \boldsymbol{u} \otimes \boldsymbol{u} + p\boldsymbol{I}], \tag{2.146}$$

$$\frac{\partial E}{\partial t} = -\boldsymbol{\nabla} \cdot [(E + p)\, \boldsymbol{u}] - L, \tag{2.147}$$

$$\frac{\partial (n_{\mathrm{H}} f)}{\partial t} = -\boldsymbol{\nabla} \cdot [n_{\mathrm{H}} f \boldsymbol{u}] + J(f, n_{\mathrm{H}}, T), \tag{2.148}$$

$$\frac{\partial n_{\mathrm{H_2}}}{\partial t} = -\boldsymbol{\nabla} \cdot [n_{\mathrm{H_2}} \boldsymbol{u}] - n_{\mathrm{H_2}} n_{\mathrm{H}} k(T), \tag{2.149}$$

$$\frac{\partial n_{\mathrm{H}}}{\partial t} = -\boldsymbol{\nabla} \cdot [n_{\mathrm{H}} \boldsymbol{u}] + 2 n_{\mathrm{H_2}} n_{\mathrm{H}} k(T), \tag{2.150}$$

$$\frac{\partial (\rho \tau)}{\partial t} = -\boldsymbol{\nabla} \cdot [\rho \tau \boldsymbol{u}], \tag{2.151}$$

where ρ is the mass density, $\boldsymbol{u} = (u, v, w)$ is the fluid velocity vector, p is the pressure, $\boldsymbol{I}$ is the identity tensor, E is the total energy density, L is the energy loss, n_{H} and $n_{\mathrm{H_2}}$ are the number densities of atomic and molecular hydrogen, f is the ionisation fraction of hydrogen, T is the temperature, $J(f, n_{\mathrm{H}}, T)$ is the rate of ionisation/recombination of atomic hydrogen, $k(T)$ is the dissociation coefficient of molecular hydrogen obtained from Dove & Mandy (1986), and τ is a scalar introduced to track the jet material.

Equations (2.145) to (2.147) are the conservation equations for mass, momentum and energy, respectively. Equation (2.148) describes the ionisation fraction of hydrogen, Equation (2.149) describes the number density of hydrogen molecules, Equation (2.150) describes the number density of hydrogen atoms, and Equation (2.151) is an equation for τ that acts as a tracer for the jet material.

The Ionisation Equation

In order to calculate the total number density of the gas including free electrons we need to know the number of free electrons in the gas. The total number density of the gas is used to calculate the heat capacity, c_v, of the gas and therefore affects the gas dynamics. We assume that the only free electrons, that affect the dynamics

of the gas, come from hydrogen. This assumption is relatively accurate at high temperatures ($T > 5 \times 10^3 K$) above which hydrogen starts to become ionised and is most accurate at temperatures above a few times $10^4 K$ at which point almost all hydrogen is in the form of ions. Below $T = 5 \times 10^3 K$ the ionisation of other species becomes more important, but since hydrogen is far more abundant than the other species its ionisation is, by far, the most important overall.

We keep track of the flow of ionised hydrogen and its creation through the use of a continuity equation (2.148) for the ionisation fraction, f, of hydrogen. On the right hand side of this equation is a source term which, following Falle & Raga (1995), is the rate of ionisation of atomic hydrogen J, i.e. the rate at which H^+ ions are created, and is given by

$$J(f, n_{\rm H}, T) = n_{\rm H}^2 \left\{ f(1-f)c(T) - f^2 r(T) \right\}. \tag{2.152}$$

Here $c(T)$ and $r(T)$ are the collisional ionisation and radiative recombination coefficients in $\rm cm^3\ s^{-1}$ respectively and are given by

$$c(T) = 6.417 \times 10^{-11} T^{1/2} \exp\left(\frac{-1.579 \times 10^5}{T}\right),$$
$$r(T) = 2.871 \times 10^{-10} T^{-0.7}.$$

Initially the ionisation fraction is set so that the the rate at which H^+ ions are created is zero, i.e. $J = 0$, and results in

$$f = \frac{c(T)}{c(T) + r(T)}. \tag{2.153}$$

The energy loss due to the ionisation of atomic hydrogen also needs to be taken into account in the energy equation and is discussed in more detail below.

The Hydrogen Equations

Molecular hydrogen is included in these simulations therefore its dissociation needs to be accounted for. Dissociation of molecular hydrogen is the process by which it

becomes split into its two constituent hydrogen atoms. It can occur when a particle collides with a hydrogen molecule and some of the kinetic energy of the collision is converted into internal energy, resulting in the breaking of the bond and hence the fragmentation of the molecule into two hydrogen atoms. As noted by Dove & Mandy (1986), at sufficiently low densities the time between collision is so long that almost every molecule that becomes internally excited by a collision will lose that energy through emission of radiation before colliding again. Therefore in the case of a low density medium the most important way for dissociation to occur is through dissociation out of the lowest energy level ($v = 0$ and $J = 0$) only. Using this approach we obtain $k(T)$ the collisional dissociation rate coefficient for H-H_2 collisions, which is thought to be the most efficient collision type at dissociating H_2. The reformation of H_2 is ignored because it is thought that the reformation time is too long, when compared to the duration of the simulations, for it to have a significant effect. It must be noted that Raga et al. (2005) recently found that in at least some cases the contrary is true.

The flow of molecular hydrogen and its destruction is kept track of through the use of a continuity equation (2.149) for molecular hydrogen. The term on the right hand side is the source term which, following Dove & Mandy (1986), includes the collisional dissociation rate coefficient, $k(T)$, given in $\mathrm{cm}^3\ \mathrm{s}^{-1}$ by

$$k(T) = \frac{\beta(k_B T)^{2.012} \exp\left[\frac{-4.463}{T}\right]}{(1 + (0.2472)k_B T)^{3.512}}, \tag{2.154}$$

where

$$\beta = 1.05 \times 10^{-10}\,\mathrm{eV}^{1.5}\,\mathrm{cm}^3\,\mathrm{s}^{-1}$$

and where k_B is Boltzmann's constant,

$$k_B = 8.618 \times 10^{-5}\,\mathrm{eV\,K}^{-1}.$$

Of course if you have an equation that accounts for the removal of hydrogen molecules that have been dissociated you also need one to account for the inclusion of the ad-

ditional hydrogen atoms that this creates, and so we require a continuity equation for atomic hydrogen too (2.150). The source term on the right hand side of this equation adds two hydrogen atoms for every hydrogen molecule that is dissociated. As in the case of the ionisation of atomic hydrogen the energy loss due to the dissociation of molecular hydrogen also needs to be taken into account in the energy equation, as discussed below.

The Jet Tracer Equation

Equation (2.151) is an equation for τ that acts as a tracer for the jet material. Initially $\tau = 0$ everywhere on the grid except at the boundary from which the jet enters where $\tau = 1$. Comparing the equation for τ with the density equation (2.145) we see that τ is advected in the same way as density. By setting $\rho_{\rm jet}$ to be the density of jet material entering the grid, which is kept constant, we can obtain the density of jet material in any cell by calculating $\tau\rho_{\rm jet}$ for that cell. The fraction of fluid in a particular cell comprised of jet material can then be obtain by dividing the density of jet material by the overall density for that cell,

$$\frac{\tau(i,j)\rho_{\rm jet}}{\rho(i,j)}. \tag{2.155}$$

This fraction is useful in estimating the amount of mixing between the jet and ambient medium.

The Energy Equation

As in Section 2.2 we assume the gas law to be

$$p = (\gamma - 1)\left(E - \frac{1}{2}\rho(u^2 + v^2 + w^2)\right). \tag{2.156}$$

The total energy density is then given by the equation

$$E = \frac{1}{2}\rho(u^2 + v^2 + w^2) + \frac{1}{\gamma - 1}p. \tag{2.157}$$

The energy loss, L, due to radiative and chemical processes is given by

$$L = L_{\rm rad} + E_I J(f, n_{\rm H}, T) + E_D k(T), \tag{2.158}$$

where E_I is the ionisation energy of atomic hydrogen and E_D is the dissociation energy of molecular hydrogen. $L_{\rm rad}$ is the loss due to radiative transitions and is made up of a function for losses due to atomic transitions (Sutherland & Dopita, 1993), and one for losses due to molecular transitions (Le Bourlot et al., 1999). The second term in L is the energy dumped into ionization of H, and the third is that dumped into dissociation of H_2.

Radiative Cooling and Emissions

As mentioned above $L_{\rm rad}$ is the energy loss due to radiative transitions and is made up of a function for losses due to atomic transitions (Sutherland & Dopita, 1993), and one for losses due to molecular transitions (Le Bourlot et al., 1999). Sutherland & Dopita (1993) calculated the cooling function for a plasma slab under equilibrium and non-equilibrium conditions for a range of species abundances and for a range of temperatures, 10^4-$10^{8.5}$K. These cooling functions were given in tabular form where log of the temperature, $\log(T)$, was tabulated against several other plasma properties including the log of the normalised cooling rate, $\log(\Lambda_N)$, given in units of ergs cm^{-3} s^{-1}. The specific function chosen for this work is the one that takes into account the effects of non-equilibrium ionisation, has solar abundances of the species, assumes that all the radiation generated by the cooling plasma is reabsorbed downstream and is for a gas cooling from $\log(T) = 6.5$ to $\log(T) = 4$. Linear interpolation is used to interpolate between the values in the table and hence obtain a cooling curve of the normalised cooling rate. This cooling curve should be accurate up to very high densities (10^8 cm^{-3}). Below 10^4K we assume that the only significant radiative cooling is due to molecular hydrogen.

Energy losses due to molecular transitions are based on a paper by Le Bourlot et al. (1999), in which the radiative cooling rate of a gas containing H_2 which is collisionally excited by H, He and H_2 is computed. Further details on this cooling

function are given in Chapter 3.

2.5.2 The Scheme

The scheme used here is the temporally and spatially second order accurate scheme described in Downes & Ray (1999). It is a two-step scheme which steps to time $t = t_{n+1/2}$ from $t = t_n$ using an upwind scheme that is first order in time and space. The values of the variables at time $t = t_{n+1/2}$ are then used to calculate fluxes which are second order accurate in space. These fluxes are used to integrate from time $t = t_n$ to time $t = t_{n+1}$ which leads to a scheme which is second order in time.

As an example of how we integrate Equations (2.145) to (2.151) let us consider a continuity equation for a variable q, in one dimension. Using a half time step in Equation 2.104 we have the exact relation

$$Q_i^{n+1/2} = Q_i^n - \frac{\Delta t}{2\Delta x}\left[F_{i+1/2}^n - F_{i-1/2}^n\right], \tag{2.159}$$

which can be interpreted approximately using an approximation to the average flux across the boundaries, $F_{i\pm1/2}^n$. Defining ${}^1F_{i+1/2}^n$, a first order approximation to the average flux across the cell boundary $x = x_{i+1/2}$ at time $t = t_n$, as

$${}^1F_{i+1/2}^n = \begin{cases} u_{i+1/2}^n Q_i^n & \text{if } u_{i+1/2}^n \geqslant 0, \\ u_{i+1/2}^n Q_{i+1}^n & \text{otherwise,} \end{cases} \tag{2.160}$$

where $u_{i+1/2}^n$ is the advection velocity, leads to the first order approximation to the values of the variable, q, at time $t = t_{n+1/2}$

$$Q_i^{n+1/2} \approx Q_i^n - \frac{\Delta t}{2\Delta x}\left[{}^1F_{i+1/2}^n - {}^1F_{i-1/2}^n\right]. \tag{2.161}$$

The advection velocity, pressure and density at the cell boundary $x = x_{i+1/2}$ are calculated using a Riemann solver. Letting $u^*(u_L, u_R)$ be the advection velocity

resolved using the Riemann solver, we obtain

$$u^n_{i+1/2} = u^*(u_L, u_R) = u^*(u^n_i, u^n_{i+1}). \tag{2.162}$$

In order to gain a second order in time approximation to the values of the variable, q, at time $t = t_{n+1}$ we use a central-time central-space (CTCS) method, better known as the leapfrog method, with a half time and spatial step:

$$Q^{n+1}_i \approx Q^n_i - \frac{\Delta t}{\Delta x}\left[F^{n+1/2}_{i+1/2} - F^{n+1/2}_{i-1/2}\right]. \tag{2.163}$$

The fluxes at the half time step are used to "leapfrog" from time $t = t_n$ to time $t = t_{n+1}$. The fluxes are calculated using the first order accurate values of the variable, q, at time $t = t_{n+1/2}$ and so this method, while being second order in time, will only be first order accurate in space.

In order to make this method second order accurate in space we need to calculate the second order fluxes at time $t = t_{n+1/2}$. To do this we make an estimate of the gradients of the primitive variables ρ, u and p in each cell. For a variable, q, we estimate the gradient of q within cell i,

$$\frac{\partial q}{\partial x} = \frac{g^{Q(t_n)}_i}{\Delta x},$$

using the equation

$$g^{Q(t_n)}_i = \mathrm{av}(Q^n_{i+1} - Q^n_i, Q^n_i - Q^n_{i-1}), \tag{2.164}$$

where the function av is the non-linear averaging function defined in Equation 2.139 such that

$$g^{Q(t_n)}_i = \begin{cases} \frac{2(Q^n_{i+1}-Q^n_i)(Q^n_i-Q^n_{i-1})}{Q^n_{i+1}-Q^n_{i-1}} & \text{if } (Q^n_{i+1} - Q^n_i)(Q^n_i - Q^n_{i-1}) > 0, \\ 0 & \text{otherwise.} \end{cases} \tag{2.165}$$

We can now define the second order flux at $x = x_{i+1/2}$ and time $t = t_{n+1/2}$ as

$$ {}^2F_{i+1/2}^{n+1/2} = \begin{cases} u_{i+1/2}^{n+1/2}[Q_i^{n+1/2} + \frac{1}{2}g_i^{Q(t_{n+1/2})}] & \text{if } u_{i+1/2}^{n+1/2} > 0, \\ u_{i+1/2}^{n+1/2}[Q_{i+1}^{n+1/2} - \frac{1}{2}g_{i+1}^{Q(t_{n+1/2})}] & \text{otherwise,} \end{cases} \tag{2.166} $$

where the advection velocity $u_{i+1/2}^{n+1/2}$ is again calculated using the Riemann solver. The notable difference here is that the left and right values of the primitive variables sent to the Riemann solver are first corrected to take account of their gradients. So for u we have that

$$ u_{i+1/2}^{n+1/2} = u^*(u_L, u_R) = u^*(u_i^{n+1/2} + \frac{1}{2}g_i^{u(t_{n+1/2})}, u_{i+1}^{n+1/2} - \frac{1}{2}g_{i+1}^{u(t_{n+1/2})}). \tag{2.167} $$

A second order accurate scheme in time and space is then given by solving

$$ Q_i^{n+1} = Q_i^n - \frac{\Delta t}{\Delta x}\left[{}^2F_{i+1/2}^{n+1/2} - {}^2F_{i-1/2}^{n+1/2}\right]. \tag{2.168} $$

2.5.3 Boundary Conditions

The scheme outlined above requires a double layer of boundary cells or "ghost cells" to be set up around the boundary of the grid. These boundary cells need to be updated, at the beginning of each of the two steps involved in the scheme, according to the boundary conditions. The boundary conditions are reflective along the jet axis, $r = 0$, and on the left-hand side of the grid, $z = 0$, except where the jet enters. All remaining boundaries have gradient zero conditions. For gradient zero boundary conditions a boundary cell is set to equal its nearest neighbouring cell that is inside the computational grid. For reflective boundary conditions the two boundary cells are set to be a refection of the two corresponding cells inside the computational grid, i.e. reflection across the boundary, with the added condition that the value of the velocity perpendicular to that boundary is reversed.

2.5.4 Methods for Dealing With Numerical Problems

There are several numerical problems that can occur in molecular outflow simulations. One problem, related to the stability of the scheme, concerns spurious oscillations in the solution that often occur around regions with strong gradients. Another common problem is the occurrence of negative pressures in some cells on the grid, usually encountered when a cooling function has been incorporated into the equations.

Artificial Viscosity

To damp spurious oscillations artificial viscosity is added which increases the numerical diffusion and hence smooths the oscillations that occur around shocks. The artificial viscosity is added to the pressure term and so it affects the momentum and energy flux calculations. The amount added to the momentum flux across each cell interface is given by

$$\nu = l_\nu^2 \rho^2 u_b^2, \tag{2.169}$$

where u_b is the velocity jump across the cell interface, ρ is the resolved density at the cell interface and l_v is the length scale, given in terms of the number of cells, over which the shock is to be smeared. The amount added to the energy flux across each cell interface is given by νu^*, where u^* is the resolved velocity at the cell interface. This artificial viscosity is only added when there is a compression at the cell interface, that is when the velocity to the left is greater than the velocity to the right.

Negative Pressures

If there's a large amount of cooling in a particular cell it can sometimes reduce the total energy by so much that there's more kinetic energy in that cell than total energy after cooling. Since internal energy is total energy minus kinetic energy, the result would be negative internal energy and hence negative pressure for that cell, which is an obviously unphysical phenomenon. From the discussion above, we can see that

this might occur in a region with high cooling relative to internal energy. Since the molecular H_2 cooling is proportional to ρ^2 and the internal energy is proportional to ρ^1, numerical density errors in regions of very low density can cause molecular H_2 cooling to be larger than it should be, which in turn can cause negative pressures. One method of resolving this problem is to reset any negative pressures, to positive values, after each half and full time step. Each negative pressure is reset to the maximum value for the pressure in each of its four neighbouring cells. That is, if $p_{i,j} < 0$, it is reset to

$$p_{i,j} = \max(p_{i-1,j}, p_{i+1,j}, p_{i,j-1}, p_{i,j+1}). \tag{2.170}$$

If the four neighbouring cells all have negative pressures then the pressure is reset to it's original value before the time step was begun.

2.5.5 The Riemann Solver

As described above, the advection velocity, pressure and density at the cell boundaries $x = x_{i+1/2}$ are calculated using a Riemann solver to solve the Riemann problem at the cell interfaces. The solution to the Riemann problem is much simpler when given in terms of primitive variables

$$\boldsymbol{P} = \begin{pmatrix} \rho \\ u \\ p \end{pmatrix}. \tag{2.171}$$

A first approximation is obtained using a linear Riemann solver which gives accurate results in smooth regions but encounters difficulties in the presence of shocks and rarefactions. For this reason, if the pressure resolved in the linear Riemann solver differs by more than 10% to either the pressure in the left state or the pressure in the right state, a non-linear solver is then used. There are four possible wave patterns involved in the solution to the Riemann problem for the Euler equations, each of which is shown in Figure 2.8. The middle wave will always be a contact

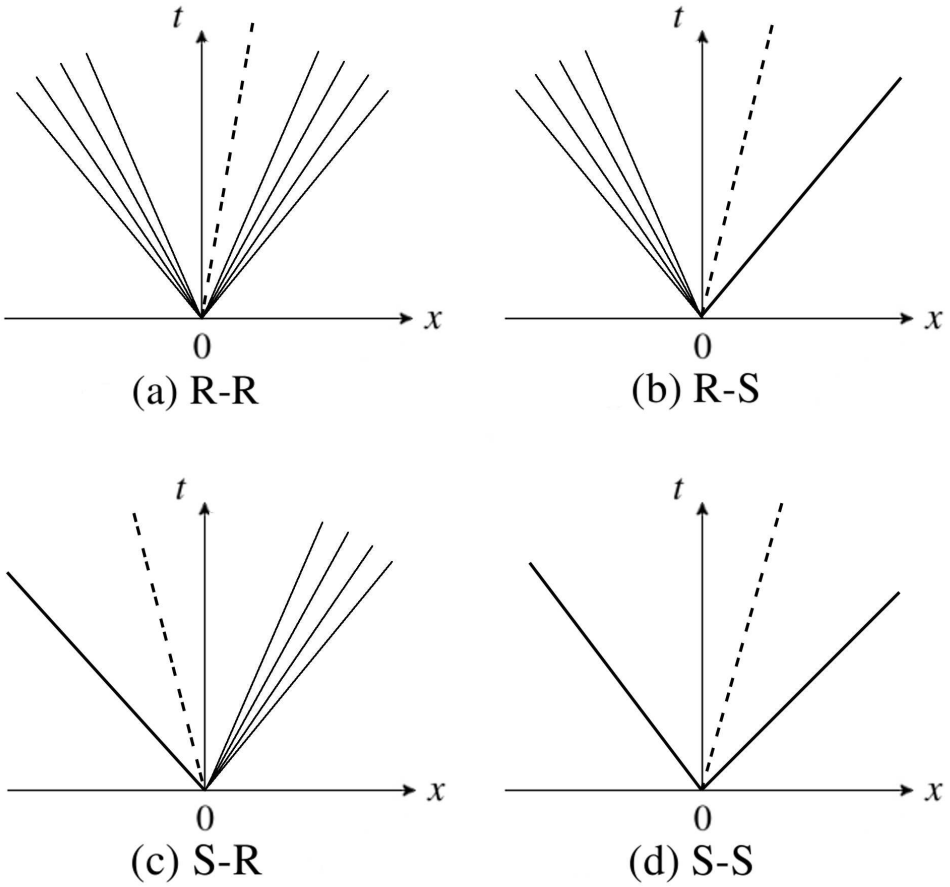

Figure 2.8: The four possible wave patterns involved in the solution to the Riemann problem for the Euler equations. The middle wave will always be a contact discontinuity while the first and third waves will be either shocks or rarefactions. (a) Two rarefactions (R-R). (b) One rarefaction and one shock (R-S). (c) One shock and one rarefaction (S-R). (d) Two shocks (S-S).

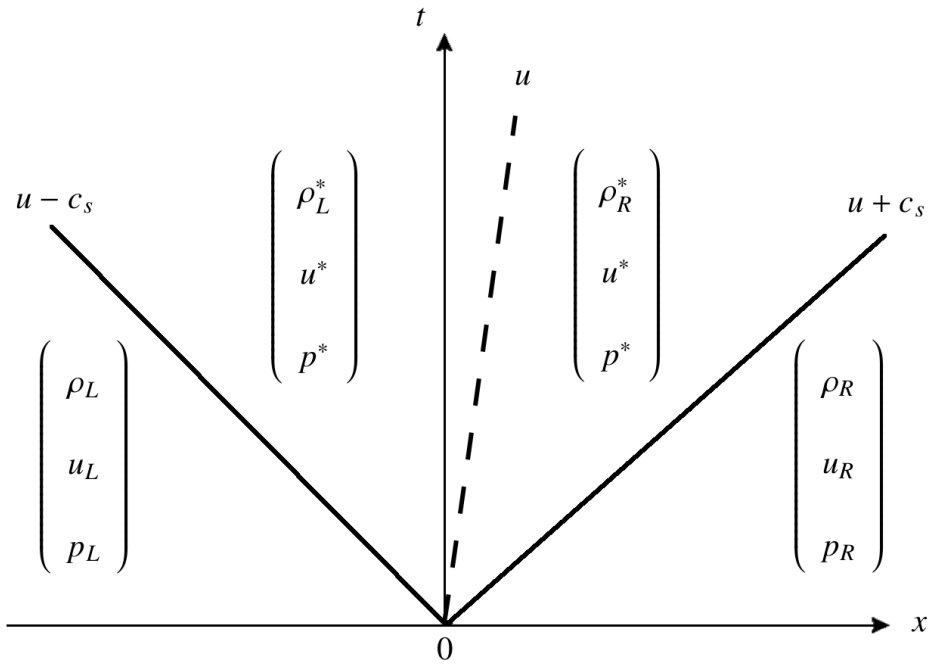

Figure 2.9: Diagram showing the four regions involved in the solution to the Riemann problem for the Euler equations. The regions correspond, from left to right, to the left state (L), the inner left state ($^*L$), the inner right state ($^*R$) and the right state (R).

discontinuity while the first and third waves will be either shocks or rarefactions. So, the four possible wave patterns correspond to the different combinations of the first and third waves. They can both be rarefactions (R-R), or both be shocks (S-S) or one could be a shock and the other a rarefaction (S-R) or vice-versa (R-S).

The region between the first and third waves is divided into two constant regions by the contact discontinuity, that we shall call $^*L$ and $^*R$. Figure 2.9 shows the four regions involved in the solution. Using the fact that the pressure and velocity are constant across the contact along with the usual shock and rarefaction relations, obtained by connecting the $^*L$ region to the left state across the first wave and the $^*R$ region to the right state across the third wave, we derive a non-linear equation for the pressure in the inner region. The solution for the pressure in the inner region, p^*, is the root of the equation

$$h(p) = h_L(p) + h_R(p) + (u_R - u_L) = 0, \tag{2.172}$$

where

$$h_L(p) = \begin{cases} (p - p_L)\sqrt{\frac{\alpha_L}{p+\beta_L}} & \text{if } p > p_L \quad \text{(shock)} \\ \frac{2c_L}{(\gamma-1)}\left[\left(\frac{p}{p_L}\right)^z - 1\right] & \text{if } p \leqslant p_L \quad \text{(rarefaction)} \end{cases}$$

$$h_R(p) = \begin{cases} (p - p_R)\sqrt{\frac{\alpha_R}{p+\beta_R}} & \text{if } p > p_R \quad \text{(shock)} \\ \frac{2c_R}{(\gamma-1)}\left[\left(\frac{p}{p_R}\right)^z - 1\right] & \text{if } p \leqslant p_R \quad \text{(rarefaction)} \end{cases}$$

and

$$\alpha_L = \frac{2}{(\gamma+1)\rho_L}, \quad \beta_L = \frac{(\gamma-1)}{(\gamma+1)}p_L, \quad \alpha_R = \frac{2}{(\gamma+1)\rho_R}, \quad \beta_R = \frac{(\gamma-1)}{(\gamma+1)}p_R,$$

$$c_L = \sqrt{\frac{\gamma p_L}{\rho_L}}, \quad c_R = \sqrt{\frac{\gamma p_R}{\rho_R}}, \quad z = \frac{(\gamma-1)}{2\gamma},$$

where c_L and c_R are the velocities of sound in the left and right states respectively.

In the case of two rarefactions (R-R), with equal values for the heat capacity ratio on either side of the interface, Equation 2.172 simplifies to give

$$p^* = \left[\frac{c_L + c_R - \frac{\gamma-1}{2}(u_R - u_L)}{(c_L/p_L^z) + (c_R/p_R^z)}\right]^{1/z}. \tag{2.173}$$

When the heat capacity ratio on both sides of the interface are different an iterative Newton-Raphson method is used to determine the value for p^*. When the Newton-Raphson method fails to converge a bisection method is used instead.

In the remaining cases Equation 2.172 is solved iteratively, updating p^* at each iteration until it's value converges. The initial pressure given to each of the iterative methods is the approximate pressure obtained using the linear Riemann solver.

The velocity in the inner region follows on from the pressure, p^*, and is given by

$$u^* = \frac{1}{2}(u_L + u_R) + \frac{1}{2}\left[h_R(p^*) - h_L(p^*)\right]. \tag{2.174}$$

Once we have a solution for the pressure and velocity in the inner region, p^* and u^*, the remaining unknowns are found using the standard shock and rarefaction

relations. The sign of the velocity tells us whether the contact discontinuity is to the left or to the right of the cell interface. The fluxes across the interface can then calculated from the resolved values of the pressure, density and velocity.

Chapter 3

New Cooling Function

A description of a new cooling function which is used in the two-dimensional hydrodynamic simulations of stellar jets carried out in this work is presented in this section along with the old cooling function for comparison. Radiative cooling plays an important role in determining the shape of a stellar jet. When an atom or molecule falls from one energy level to a lower energy level it emits a photon. In the case of a stellar jet there is a high probability that this photon will escape the jet and thereby contribute to the jet's cooling. A reduction in the temperature of the jet will also mean a reduction in the pressure which will, in turn, effect the shape of the jet. The new cooling function results in less molecular cooling taking place in the jet. Several simulations were undertaken some with the new cooling function and some with the old. The results of these simulations and the details of the cooling functions are included below.

3.1 Molecular Cooling

We know from quantum mechanics that energy exists only in discrete quantities, called quanta. Each atom or molecule has it's own energy level which, since energy is quantised, can only have certain discrete values. When collisions occur between atoms, molecules and photons, the electrons in the atoms or molecules can be raised from one energy level to a higher energy level. This process, whereby the electron transitions from a lower to a higher orbit, is called excitation. In a collision between

a photon and a molecule, the photon will be absorbed by the molecule if it contains exactly the energy required for an electron in the molecule to make an upward transition from a lower to a higher orbit.

The lifetime of such a raised energy level can be very brief. The excited electron in the atom or molecule loses the energy of excitation by falling to a lower level. At the same time it emits a photon to carry off the excess energy. This is called de-excitation.

A high percentage of the photons that are emitted will escape from the medium, thereby contributing to it's cooling. So in the case of a jet, with many de-excitations and therefore the emission of many photons, the jet is cooled.

The rotational excitation of H_2 only becomes important for kinetic temperatures T >100 K while the ro-vibrational excitation requires T >1000 K.

3.2 Changes to the Cooling Function

The two-dimensional hydrodynamic simulations outlined in Section 2.5 already included a radiative cooling function (Downes & Ray, 1999) but the cooling function needed to be updated in order to reflect changes found in more recent research. These changes are discussed here. In Downes & Ray (1999) the cooling function dealing with H_2 cooling was based on a paper by Lepp & Shull (1983). In this paper the rate coefficient for H_2 dissociation is computed. Also given are the rate coefficients for collisional de-excitation of H_2 by H and the radiative cooling rate. Of interest to us is the radiative cooling rate, $\Lambda_{\rm r}$, that is fitted to a sum of terms representing vibrational and rotational cooling from both H-H_2 and H_2-H_2 collisions, and is given in erg cm^{-3} s^{-1} by

$$\Lambda_{\rm r} = n_{\rm H_2}\left[\frac{L_{vH}}{1+(L_{vH}/L_{vL})}+\frac{L_{rH}}{1+(L_{rH}/L_{rL})}\right], \tag{3.1}$$

where the vibrational cooling coefficients at high and low density are

$$L_{vH} = 1.1 \times 10^{-13} \exp\left(-6744/T\right) \tag{3.2}$$

$$L_{vL} = 8.18 \times 10^{-13} [n_{\rm H} k_{\rm H}(0,1) + n_{\rm H_2} k_{\rm H_2}(0,1)], \tag{3.3}$$

where $k_{\rm H}(0,1)$ and $k_{\rm H_2}(0,1)$ are the $v = 0 \rightarrow 1$ collisional excitation rates for H-H_2 and H_2-H_2 collisions respectively and where the critical density, that defines what is meant by high and low density, is given by

$$\log n_{\rm cr} = \begin{cases} 4.00 - 0.416x - 0.327x^2, & ({\rm H\text{-}H_2}) \\ 4.13 - 0.968x - 0.119x^2, & ({\rm H_2\text{-}H_2}) \end{cases} \tag{3.4}$$

with $x = \log(T/10^4)$. Downes & Ray (1999) ignored the contribution of the $k_{\rm H_2}(0,1)$ term since cooling due to H_2-H_2 interactions are only important for low temperatures. The term $k_{\rm H}(0,1)$ is defined as

$$k_{\rm H}(0,1) = \begin{cases} 1.0 \times 10^{-12} \sqrt{T} \exp\left(-1000/T\right), & ({\rm T} > 1635\,{\rm K}) \\ 1.4 \times 10^{-13} \exp\left[(T/125) - (T/577)^2\right]. & ({\rm T} < 1635\,{\rm K}) \end{cases} \tag{3.5}$$

The rotational cooling coefficients at high and low density are

$$L_{rH} = \begin{cases} 3.9 \times 10^{-19} \exp\left(-6118/T\right), & ({\rm T} > 1087\,{\rm K}) \\ {\rm dex}\left(-19.24 + 0.474x - 1.247x^2\right), & ({\rm T} < 1087\,{\rm K}) \end{cases} \tag{3.6}$$

$$L_{rL} = \begin{cases} Q(n) 1.38 \times 10^{-22} \exp\left(-9243/T\right), & ({\rm T} > 4031\,{\rm K}) \\ Q(n)[{\rm dex}\left(-22.99 + 0.553x - 1.148x^2\right)], & ({\rm T} < 4031\,{\rm K}) \end{cases} \tag{3.7}$$

where

$$Q(n) = (n_{\rm H_2})^{0.77} + 1.2(n_{\rm H})^{0.77} \tag{3.8}$$

is a function which bridges the gap between the low density and high density limits of the cooling.

There are several reasons why it was decided to update the cooling function. The

fits in Equations (3.1) - (3.8) are only accurate to 50% (average deviation 20%) for temperatures between 100 K and 10^5 K and densities greater than 0.1 cm^{-3}. Also the cooling was calculated using only 4 vibrational levels, each with 21 rotational states since only the $\Delta J = 0, \pm 2$ transitions were considered. Departures from thermal equilibrium increase with decreasing density and also with increasing temperature, with densities of $n_{\mathrm{H}} > 10^7\,\mathrm{cm}^{-3}$ being required for the assumption of thermal equilibrium to yield a good approximation to the cooling function (Le Bourlot et al., 1999). Therefore, the assumption of local thermodynamic equilibrium (LTE) in calculating the cooling function above was the main reason for deciding to update the cooling function.

In Le Bourlot et al. (1999) the radiative cooling rate of a gas containing H_2, which is collisionally excited by H, He and H_2, is computed. This calculation uses the results of recent quantum mechanical calculations of the cross sections for rovibrational transitions between all the energy level up to approximately 20000 K above the ground state. Importantly LTE is *not* assumed. The rate of cooling per H_2 molecule expressed in erg s^{-1} is defined as

$$W(\mathrm{H_2}) = \frac{1}{n_{\mathrm{H_2}}} \sum_{\upsilon J, \upsilon' J'} (E_{\upsilon J} - E_{\upsilon' J'}) n_{\upsilon J} A(\upsilon J \rightarrow \upsilon' J') \,, \tag{3.9}$$

where $E_{\upsilon J} > E_{\upsilon' J'}$ are the energies of the levels, expressed relative to the $\upsilon = 0$, $J = 0$ ground state and given in units of ergs. $n_{\upsilon J}$ is the population density of the level (υ,J) expressed in cm^{-3}, $A(\upsilon J \rightarrow \upsilon' J')$ is the spontaneous transition probability from level (υ,J) to level (υ',J') expressed in s^{-1}, and $n_{\mathrm{H_2}} = \sum_{\upsilon J} n_{\upsilon J}$ is the total H_2 number density. At high densities, as we would expect, the cooling function approaches the values that are obtained by assuming LTE. The cooling function has been evaluated for a wide range of values of the gas density, temperature, the atomic to molecular hydrogen density ratio and the ortho to para H_2 ratio. These ranges

are

$$\begin{aligned} 1 \leqslant n(\mathrm{H}) &\leqslant 10^8\,\mathrm{cm}^{-3}, \\ 100 \leqslant T &\leqslant 10^4\,\mathrm{K}, \\ 10^{-8} \leqslant n_{\mathrm{H}}/n_{\mathrm{H_2}} &\leqslant 10^6, \\ 0.1 \leqslant n(\mathrm{ortho})/n(\mathrm{para}) &\leqslant 3, \end{aligned} \tag{3.10}$$

where $n(\mathrm{H}) = n_{\mathrm{H}} + 2n_{\mathrm{H_2}}$. The abundance ratio of $n(\mathrm{He})/n(\mathrm{H})$ was set to 0.1 throughout their calculations. Linear interpolation is used to interpolate on the 4-dimensional grid of values of $W(\mathrm{H_2})$.

3.3 Simulations

Two 2d hydrodynamic simulations of a jet were carried out in cylindrical symmetry, one with the original cooling function and the other with the new cooling function. The code is that used in Downes & Cabrit (2007) to perform long-duration simulations of YSO jets, and is outlined in Section 2.5. We consider a typical protostellar jet of radius 0.0016 pc (5×10^{15} cm) and with a mean velocity of 215 km s^{-1}. The velocity is varied sinusoidally with time by superimposing a spectrum of sine waves on the jet velocity with a total amplitude 128 km s^{-1} and periods of 5, 10, 20 and 50 years. The grid size for each simulation is 2400×400 with a resolution of 1×10^{14} cm in both the z and r directions. The jet temperature is taken to be 1000 K and the total jet number density is set to 100 cm^{-3}. The time-averaged jet Mach number is therefore about 93 with respect to the jet material. The ambient temperature is taken to be 100 K and the total ambient number density is set to 100 cm^{-3}, the same density as the jet. Overall the jet and ambient gases are assumed to be of solar abundances while the molecular fraction in the jet and ambient medium is taken to be $n(H_2) = 9n(H)$. The boundary conditions are reflecting on r = 0 (i.e. the jet axis) and on z = 0 except where the jet enters, and gradient zero on every other boundary. Each simulation was run for 450 years. A density plot for each simulation is shown in Figures 3.1 and 3.2.

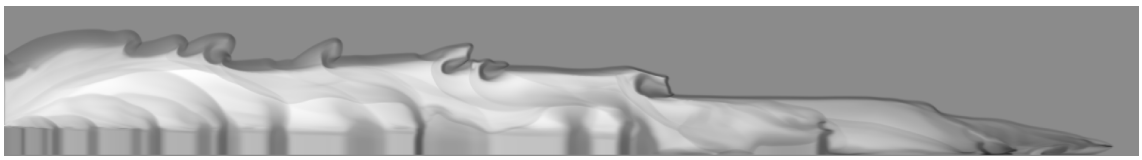

Figure 3.1: Density plot of a simulation run using the original cooling function.

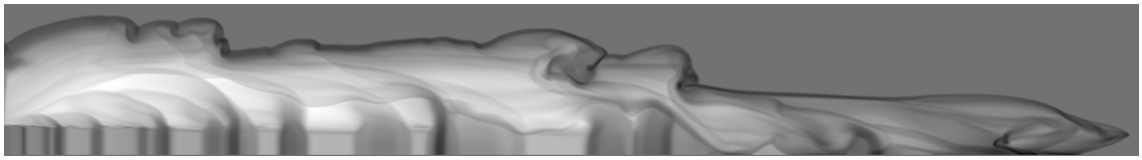

Figure 3.2: Density plot of a simulation run using the new cooling function.

3.4 Results

The head of the jet and bow shock system is under very high pressure due to the strong shocks that can be found there. This means the atoms and molecules are moving about much more energetically and therefore there are an increased number of collisions. With more collisions there are more excitations and therefore more de-excitations. More de-excitations means a higher amount of cooling. The result of a reduction in temperature is a reduction in pressure which ultimately results in a lower pressure gradient. Material at the bow shock spreads outward at a slower rate due to this reduced pressure gradient.

The output of the new cooling function is a lower cooling rate than the original function. So, from the converse of the above argument we should end up with the bow shock being more spread out than the original. Looking at the simulations in Fig. 3.1 and Fig. 3.2 we can see that this is the case.

Downes & Cabrit (2003) showed that molecular dissociation plays a crucial role in producing a break in slope at around $v_{\rm break} \simeq 20\,{\rm km\,s^{-1}}$ in the molecular mass-velocity relation for jet-driven flows. Figure 3.3 shows the mass-velocity relations for both our simulations. The main point to note is that the break in the molecular mass-velocity relation occurs at a much lower velocity for the simulation run using the new cooling function. The reason for this is the much higher level of dissociation that is found in this simulation as a result of the lower cooling rate and hence higher temperatures.

The lower than usual slopes for the mass-velocity relations shown in the figures

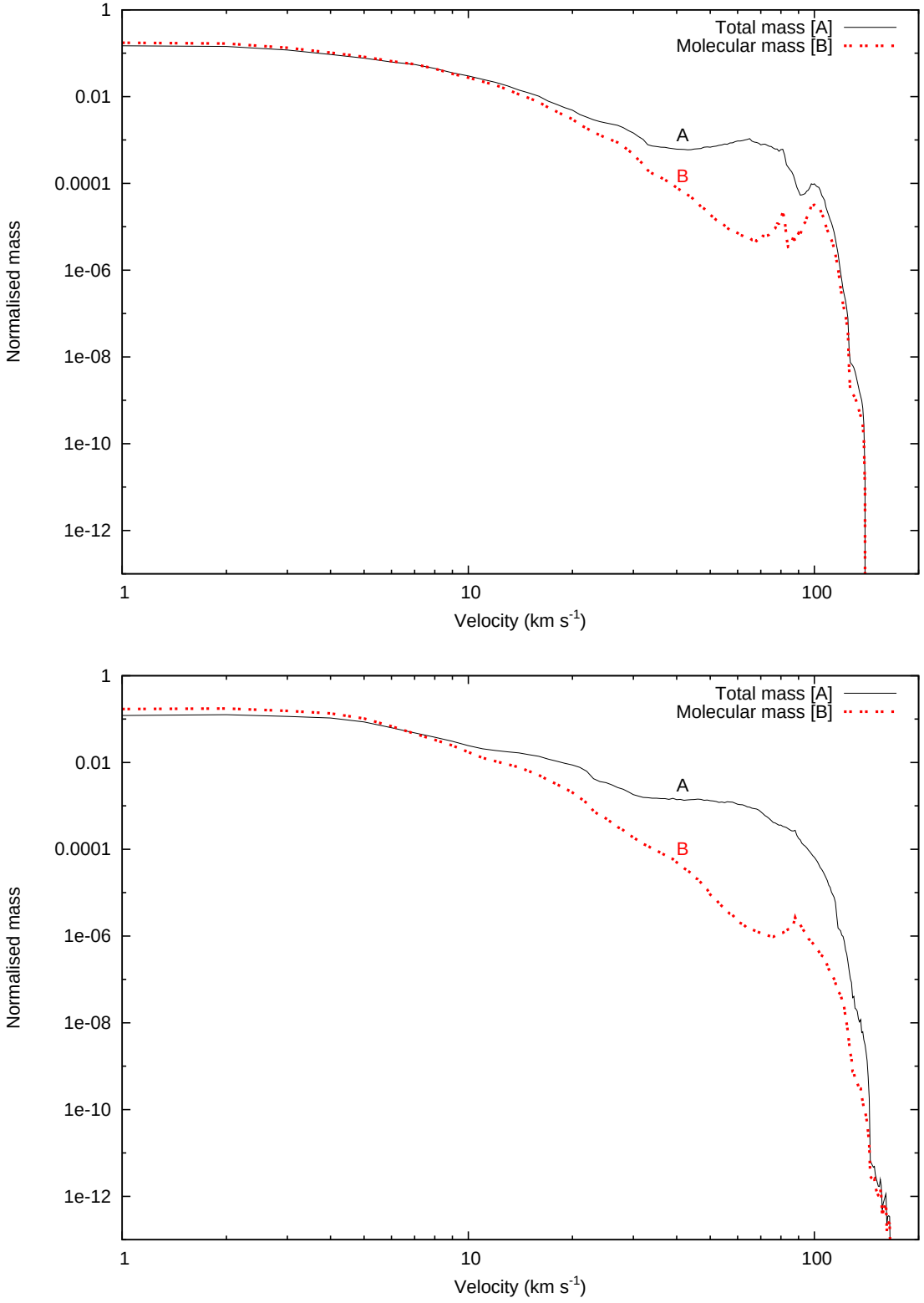

Figure 3.3: Plots of the normalised mass-velocity relations for all swept-up material (i.e. excluding jet material), [A], and for molecular swept-up material only, [B], for jet simulations after t = 450 years run using the old (top) and new (bottom) cooling functions. An angle of 30° to the plane of the sky is assumed.

are a result of the relatively young outflow ages of the simulations, 450 years. As noted in Keegan & Downes (2005) a minimum age of 1500 years is required in order to ensure that the system has overcome it's initial transience and that characteristics such as the mass-velocity relations have reached a quasi-steady state.

Chapter 4

Propagation of Molecular Outflows Into Inhomogeneous Media.

The structure of molecular clouds was discussed in Section 1.1. They have been observed to be 'clumpy' in nature containing dense cores and rarefied filaments and cocoons that form an almost hierarchical arrangement of smaller scale structures contained within larger ones (Myers et al., 1978). Also, they are magnetised and turbulent and it is thought that the inhomogeneous structure and fragmentation is due to some combination of turbulence, MHD instabilities and thermal instabilities (Williams et al., 2000, and references therein). The pre-steller dense cores that molecular clouds contain are thought to be initially supported against their self-gravity by magnetic or turbulent pressure, or perhaps both. Through ambipolar diffusion and/or the dissipation of turbulence self-gravity begins to dominate the other forces, the cores become gravitationally unstable and collapse to form protostars. The envelopes surrounding these protostars have been observed to be highly centrally concentrated, with radial density profiles consistent with $\rho \propto r^{-1.5}$ or $\rho \propto r^{-2}$ (Ladd et al., 1991).

Associated with the early stages of young stars is an energetic mass-ejection phenomenon. This mass-ejection phenomenon is thought to be responsible for the molecular outflows that are observed in molecular clouds. Interactions of these outflows with an inhomogeneous ambient medium may cause significant changes in the physical, dynamical and even chemical states of these outflows. We noted previously

that Dopita et al. (1982b) believed the "interaction of the jets with ambient cloudlets could hence be implicated with the production of HH nebulae". de Gouveia dal Pino et al. (1996) presented three-dimensional smoothed particle hydrodynamics (SPH) simulations that suggest that the collimated wiggling, and knotty structure of most jets may be due to the interaction of the propagating cooling jets with an inhomogeneous ambient medium. They simulated jets propagating through ambient gas with power-law density and pressure distributions. Unfortunately these simulations only lasted for 70 years, a very short amount of time in comparison to the estimated ages of outflows discussed below. Still they were able to conclude that jets propagating into portions of an ambient medium with negative density and pressure gradients develop a broad and relaxed cocoon and that the jet rapidly accelerates due to the drop of the ambient density and ram pressure. For an ambient medium with increasing density and pressure the cocoon becomes compressed and pushed backward by the ambient ram pressure and the beam is highly collimated. The compressing medium promotes Kelvin- Helmholtz (K-H) instabilities that cause beam pinching, twisting, and flapping which might explain the collimated wiggling of some jets.

de Gouveia Dal Pino (1999) has considered three-dimensional SPH simulations of interactions of overdense, radiatively cooling and adiabatic jets with dense, compact clouds in frontal and off-axis collisions and found that such events may drive momentum transfer and turbulent mixing. For off-axis collisions they found the deflected beams to initially describe a C-shaped trajectory, the angle of which decreased with time as the beam slowly penetrated the cloud. O'Sullivan & Lery (2002) presented similar simulations for non-adiabatic molecular magnetohydrodynamic (MHD) jets but also simulated a jet leaving it's molecular cloud. Once the jet had pierced the cloud and exited into the ISM it spread into a dramatically inflating cocoon and propagated more ballistically. Yirak et al. (2008) performed 2D hydrodynamic simulations of a pulsed astrophysical jet propagating through a medium that is populated with spherical inhomogeneities, or "clumps" which were smaller than the jet radius. The clumps are seen to affect the jet in several ways, such as impeding jet propagation and deflecting the jet off-axis. Numerical simulations were

also carried out by Lee et al. (2001) based on a wide-angle-wind model (see Section 1.4). These simulations were isothermal and included a stratified ambient medium whose density varied with distance from the source, r, and was proportional to $1/r^2$. Their results were compared to the observational features of several outflows and they concluded that the wide-angle-wind model could best produce the parabolic PV structure seen in some outflows.

Large-scale flows may contribute to the generation of turbulent motions and the self-regulation of star formation (Reipurth et al., 1997a). For this reason, key parameters in the theories of star formation are the total momentum and momentum injection rate ("thrust") of molecular outflows (Downes & Cabrit, 2007; Larson, 2003). The total outflow momentum is a measure of the feed-back from star formation on cloud turbulence, and its value per unit stellar mass is an essential parameter for theories of self-regulated star formation (e.g. Norman & Silk, 1980). Assuming that momentum is conserved in the wind/flow interaction, the outflow thrust (i.e. the ratio of flow momentum to age) gives a measure of the rate of momentum injection by the protostellar wind. Its ratio to the source luminosity sets a key constraint for theoretical ejection models (see Lada, 1985; Richer et al., 2000). In order to calculate the outflow thrust correctly observers must first measure the age of the outflow accurately. For this reason, among others, outflow age is an important property of a molecular outflow.

Through a survey of class I sources and what they describe as class II-D sources (those still having a residual infalling envelope) Parker et al. (1991) calculated typical outflow ages to be approximately 1.7×10^5 years. Their survey detected evidence of outflow activity associated with 70% of the sources they surveyed. Based on this, they deduced that at least 70% of the sources undergo outflow and that these outflows last for at least 70% of the time taken for their sources to evolve to the class II phase, i.e. until the majority of their envelopes have been accreted or dispersed. Several studies have concluded that the combined duration of class I and class II-D phases is $\sim 2.5 \times 10^5$ years (Beichman et al., 1986; Myers et al., 1987; Parker, 1991; Kenyon & Hartmann, 1995). Therefore, taking 70% of this time gives the typical

outflow ages mentioned above.

Some early estimates of outflow dynamical timescales were obtained by Snell et al. (1984) and were found to range from 1.5×10^3 - 1.7×10^4 years. These calculations were based on mean velocities (intensity-weighted) of 8 - 20 $\mathrm{km\,s^{-1}}$ and outflow extents of 0.03 - 0.15 pc. For a molecular outflow associated with the HH 80-81 outflow system, Yamashita et al. (1989) obtained an outflow velocity of 13 $\mathrm{km\,s^{-1}}$ based on PV diagrams of CO emission, which when coupled with a length of 1.5 pc gave a dynamical timescale of $\sim 10^5$ years. For the same system, Marti et al. (1993) used velocities based on the line widths of the HH objects themselves, $\Delta v \sim 700\,\mathrm{km\,s^{-1}}$, and calculated timescales of $\sim 4 \times 10^3$ years. This inconsistency illustrates the importance of velocity estimates on the accuracy of dynamical timescale calculations.

Dynamical timescales were also calculated in Parker et al. (1991) and were found to range from 9×10^3 - 1.4×10^4 years. For the outflow L1262 their calculation was based on each lobe extending 1.25 arcmin (0.07 pc at a distance of 200 pc) along its axis and having a velocity of 3.5 $\mathrm{km\,s^{-1}}$, as obtained from line widths. For the same outflow Terebey et al. (1989) found a timescale of 9×10^3 years using a similar velocity but a much shorter length of 0.03 pc. The differences in length were presumed to be a consequence of differences in the surface-brightness sensitivity of the interferometric measurements. This inconsistency illustrates the importance of accurate observations of outflow lengths.

The statistical approach of Parker et al. (1991) contradicts the majority of dynamical timescale estimates and suggests that dynamical ages underestimate the true outflow lifetimes by an order of magnitude. Parker et al. (1991) suggest that this is evidence in support of episodic outflow. Downes & Cabrit (2007) point out another possible explanation for this discrepancy. They noted that the sources of Parker et al. (1991) were selected to be in isolated dark globules, all much less than 1 pc in size, hence the jets would be expected to have left the clouds in $\sim 1 \times 10^4$ years. Therefore, the observed extents and hence dynamical ages of all the associated CO flows would be correspondingly truncated.

In the case of optical observations, early CCD observations only covered small

fields of view due to the small number of pixels the detectors contained (McGroarty et al., 2004). For this reason it was difficult to observe very large outflows. The use of CCD mosaicing however made it possible to observe parsec-scale flows (e.g. Ray, 1987) in optical emission from HH objects. The larger CCDs in use today have made it more common for flows of this scale to be observed (Bally & Reipurth, 2001; Reipurth & Bally, 2001; McGroarty et al., 2004). McGroarty et al. (2004) also observed flows that extend for large distances. Their data shows a clear tendency for HH objects to lie close to the edges of the parent cloud or at least close to the edges of clumps. This is as would be expected since extinction by dust is minimal near the cloud edges. They conclude that most, if not all, of the flows which they studied have blown-out of their parent cloud.

Observational evidence has been found of CO lobes that are severely truncated in comparison to the full extents of their associated jets. Optical jets that have broken well out of their parent molecular clouds, some of which are giant, parsec-scale jets, have been revealed (see Bally & Reipurth, 2001; Reipurth & Bally, 2001). Also, the discovery of externally irradiated jets by Reipurth et al. (1998a) and Cernicharo et al. (1998), as discussed in Section 1.6.6, shows that some CO lobes are severely truncated.

Ideally, an accurate age estimate could be achieved by taking the length of the outflow and dividing it by the time-averaged bowshock velocity at the tip of the bowshock. In reality, this time-averaged bowshock velocity is impossible to measure, since observations are usually only carried out at one, or a few, points in time, so various methods have become popular with observers for obtaining other velocity estimates. These standard observational methods for inferring the average outflow velocity, and hence the outflow dynamical ages, are applied to the simulations carried out in this work. Downes & Cabrit (2007) concluded that dynamical timescales overestimate the age of jet-driven flows. This work attempts to reconcile the age estimates obtained using the statistics of Class I outflow surveys and those that are obtained assuming current dynamical timescales are overestimated.

The normal assumption of a homogeneous ambient medium is relaxed in this

work. Various density profiles are prescribed, based on the idea of a dense core, outside of which the density decreases with distance from the centre. The molecular fraction also decreases with distance from the centre thereby simulating the transition from a molecular cloud to a purely atomic region. Pressure is kept constant in the ambient medium so the temperature increases with distance from the centre thus simulating a region of transition between a cool molecular cloud and a hot HII region. One of the simulations reaches high enough temperatures, 15000 K, for there to be a region of partial ionisation. Using these prescriptions for inhomogeneous ambient media, long duration numerical jet simulations are run to determine the effects that the various density profiles have on the resultant outflows. Effectively, we simulate jets that are leaving their molecular clouds, similar to the irradiated jets of Reipurth et al. (1998a) and Cernicharo et al. (1998). Outflow lengths, average velocities and inferred outflow ages are compared for each simulation to determine the effects of the different density profiles on these properties.

The wide-angle-wind models discussed above and outlined in Section 1.4 remain attractive as mechanisms through which molecular outflows are produced. They are considered particularly useful for explaining old outflows with large lateral extents and low collimation. Since these models assume density in the ambient medium to vary with the distance from the source, it is only natural to compare the collimation factors obtained based on these models with the collimation of the outflows simulated in this work.

Presented in Section 4.1 is the numerical model along with the specific details of each simulation carried out. Section 4.2 outlines the analysis that was subsequently carried out on the data from those simulations, while Section 4.3 outlines the results obtained using that analysis.

4.1 Numerical Model

Described in this section are the numerical method, initial conditions and density profiles used to carry out the simulations presented in this work. The code is that used in Downes & Cabrit (2007) to perform long-duration simulations of YSO jets

and is outlined in Section 2.5.

4.1.1 Initial Conditions

We consider a typical protostellar jet of radius 0.0016 pc (5×10^{15} cm) and with a mean velocity of 215 km s^{-1}. The velocity is varied sinusoidally with time by superimposing a spectrum of sine waves on the jet velocity with a total amplitude 128 km s^{-1} and periods of 5, 10, 20 and 50 years. The grid size for each simulation is 9000×1100 (8000×1300 for the exp-1 simulation in Table 4.1) with a resolution of 1×10^{14} cm in both the z and r directions. The jet temperature is taken to be 3000 K and the total jet number density is set to 800 cm^{-3}. As outlined in Section 1.7 these are typical values that are characteristic of stellar jets. The time-averaged jet Mach number is therefore about 54 with respect to the jet material. The different density and temperature structures of the ambient medium will be outlined in Section 4.1.2 and are based on a constant initial pressure across the entire grid and decreasing density with distance from the source. Overall the jet and ambient gases are assumed to be of solar abundances while the molecular fraction in the jet is taken to be $n(H_2) = 9n(H)$. The ambient molecular structure is outlined in Section 4.1.2. The boundary conditions are reflecting on r = 0 (i.e. the jet axis) and on z = 0 except where the jet enters, and gradient zero on every other boundary.

4.1.2 Initial Ambient Profiles

The purpose of this work is to use various prescriptions for inhomogeneous media to create more realistic density profiles, and hence more realistic simulations, based on the idea of a dense core whose density decreases with distance away from the core. The results from these simulations can then be compared to those from a simulation where the assumption of a homogeneous medium is made. Five simulations are run for the purpose of this work each using a different density profile to initialise the ambient medium.

Figure 4.1 shows the different ambient density and temperature profiles used. The horizontal axis in each plot shows distance along the z axis measured in units

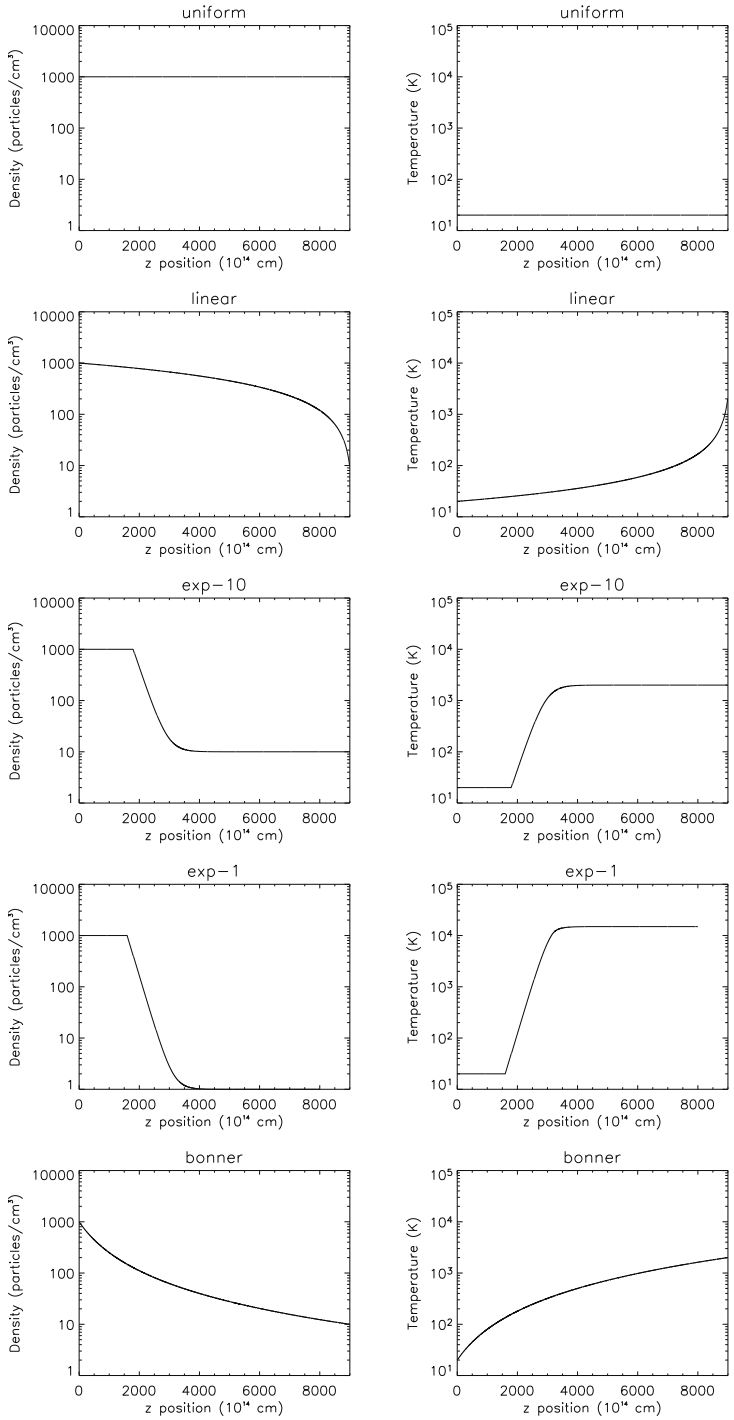

Figure 4.1: Initial ambient density and temperature profiles for each simulation. The horizontal axis in each plot shows distance measured in units of 10^{14} cm, while the vertical axis shows number density in the left hand plots and temperature in the right hand plots. The first profile represents a uniform molecular cloud with an ambient number density of $1000\,\mathrm{cm}^{-3}$. The remaining profiles have an ambient number density of $1000\,\mathrm{cm}^{-3}$ near the core and decrease to an ambient number density of $10\,\mathrm{cm}^{-3}$ further out, or in one case $1\,\mathrm{cm}^{-3}$. From top to bottom, the figure shows the uniform, linear, exp-10, exp-1 and bonnor profiles (see text for further details). All temperatures in the plots on the right hand side are calculated based on the densities in the left hand plots and the assumption of constant pressure, where the temperature nearest the core is 20 K.

Sim	Number Density Formula (cm^{-3})	
Uniform	1000	$\forall\, z$
Linear	$1000 - \left(\dfrac{990z}{\mathrm{Ncells}}\right)$	$\forall\, z$
Exp-10	1000	$z < z_1$
	$10 + 990\left(\exp\left[-\dfrac{z - z_1}{\mathrm{Ncells}/c}\right]\right)$	$z_1 \leqslant z < z_2$
	10	$z \geqslant z_2$
Exp-1	1000	$z < z_1$
	$1 + 999\left(\exp\left[-\dfrac{z - z_1}{\mathrm{Ncells}/c}\right]\right)$	$z_1 \leqslant z < z_2$
	1	$z \geqslant z_2$
Bonnor	$1000\left(\dfrac{1000}{1000 + z}\right)^2$	$\forall\, z$

Table 4.1: The density formulae that are used to obtain the density profiles in Figure 4.1. Ncells, the number of cells in the z direction, is 9000 for all simulations except the exp-1 simulation in which Ncells = 8000. Each cell measures 1×10^{14} cm in both the z and r directions. $z_1 = (\mathrm{Ncells})/5$ and $z_2 = 2(\mathrm{Ncells})/3$. $c = 35.96$ is a constant that defines the exponential curves.

of 10^{14} cm, while the vertical axis shows number density in the left hand plots and temperature in the right hand plots. Table 4.1 gives the density formulae that are used to obtain the density profiles in the z direction that are plotted in Figure 4.1. The initial ambient number density and temperature are constant perpendicular to the jet axis. The jet is injected from the left hand side of the grid, so while the first profile is used to simulate a jet propagating into a uniform molecular cloud with an ambient number density of $1000\,\mathrm{cm}^{-3}$, the other four profiles are used to simulate jets propagating from a dense "core" with an ambient number density of $1000\,\mathrm{cm}^{-3}$ into gradually less dense parts of the molecular cloud until eventually the jet is propagating into a molecular cloud with an ambient number density of $10\,\mathrm{cm}^{-3}$, or in one case $1\,\mathrm{cm}^{-3}$.

The second profile in Figure 4.1 decreases linearly in z while the third and fourth profiles have an ambient number density of $1000\,\mathrm{cm}^{-3}$ near the core and decrease exponentially to an ambient number density of $10\,\mathrm{cm}^{-3}$ in the third profile and $1\,\mathrm{cm}^{-3}$ in the fourth. The exponential decrease occurs after 1800 (exp-10) or 1600

(exp-1) grid cells in the z direction. The fifth and final profile is motivated by the idea of a Bonnor-Ebert sphere, a sphere in hydrostatic equilibrium that is surrounded and confined by a pressurised external medium. In a Bonnor-Ebert sphere the density decreases with distance from the central source according to the following formula, $\rho \propto z^{-2}$, where ρ is the density and z is the distance from the centre.

In the four simulations that have decreasing density, the initial ambient molecular fraction also decreases. Using the formula $n(H_2) = \chi_{\rm mol} n(H)$, where $\chi_{\rm mol}$ is given by the formulae in Table 4.2, we obtain the profiles of the molecular fraction in the z direction. It is noted that the molecular fraction decreases in the same way as the density from $n(H_2) = 9n(H)$ at $z = 0$ to being purely atomic at the point furthest from the centre. Therefore, we simulate jets that are exiting their molecular clouds. The initial temperature structure of the ambient medium is based on there being a constant pressure across the entire grid. The initial value for the pressure can be derived from the temperature and density at $z = 0$, 20 K and 1000 $\rm cm^{-3}$ respectively. All other initial temperatures are calculated based on the density and the constant pressure assumed above, resulting in increasing temperature with distance from the centre. In the four simulations that have decreasing density, furthest from the centre the initial temperature is 2000 K, except for the exp-1 simulation in which it is 15000 K. The high temperature in that simulation results in a partially ionised region, so we simulate a jet entering a hot HII region.

In order to ensure that the shock fronts and the cooling lengths are well resolved in each simulation, the maximum number density in the ambient medium is relatively low at 1000 $\rm cm^{-3}$. This is an essential condition for accurate treatment of H_2 dissociation and cooling. The reason for this follows from the fact that a higher ambient density will cause increased cooling in the shocks which means the cooling length will be reduced. If the cooling length is reduced, increased resolution will be necessary in order to still resolve this length. We can show this explicitly by noting that the approximate cooling timescale is

$$t_{\rm cool} \simeq \frac{nkT_{\rm shock}}{n^2 \Lambda(T)}, \tag{4.1}$$

Sim	Molecular Fraction Formula ($\chi_{\rm mol}$)	
Uniform	9	$\forall\, z$
Linear	$9 - \left(\dfrac{9z}{\rm Ncells}\right)$	$\forall\, z$
Exp-10	9 $9\left(\exp\left[-\dfrac{z-z_1}{\rm Ncells}/c\right]\right)$ 0	$z < z_1$ $z_1 \leqslant z < z_2$ $z \geqslant z_2$
Exp-1	9 $9\left(\exp\left[-\dfrac{z-z_1}{\rm Ncells}/c\right]\right)$ 0	$z < z_1$ $z_1 \leqslant z < z_2$ $z \geqslant z_2$
Bonnor	$\left[1000\left(\dfrac{1000}{1000+z}\right)^2 - 10\right]/110$	$\forall\, z$

Table 4.2: The formulae for $\chi_{\rm mol}$ which can each be substituted into the formula $n(H_2) = \chi_{\rm mol} n(H)$ to obtain the profile of the molecular fraction for each simulation. The remaining variables are defined as in Table 4.1.

where $n^2\Lambda(T)$ is the cooling rate of the gas at the shock temperature, $T_{\rm shock}$, and n is the ambient number density including electrons (Sutherland & Dopita, 1993). The cooling length, $d_{\rm cool}$, can be expressed approximately as

$$d_{\rm cool} \simeq \frac{v_{\rm shock} t_{\rm cool}}{4}, \tag{4.2}$$

$$\simeq \frac{v_{\rm shock} k T_{\rm shock}}{4 n \Lambda(T)}, \tag{4.3}$$

where $v_{\rm shock}$ is the shock velocity. Therefore, $d_{\rm cool} \propto n^{-1}$. Thus, an increase in the ambient density by a factor of 10 will require a corresponding factor of 10 increase in the resolution in order for the cooling length to remain resolved. Therefore, as mentioned above, the resolution that is chosen will limit the maximum ambient number density.

4.2 Analysis

As discussed in the introduction, one important property of a molecular outflow is its age. Once known, the age can then be used to determine other key parameters of the system such as the momentum injection rate. There are several standard techniques that have been popular with observers for calculating the age of an outflow. Three of those methods will be discussed in this section along with an improved method for estimating the age that was proposed in Downes & Cabrit (2007).

Ideally an accurate age estimate could be achieved by taking the length of the outflow in the outflow direction and dividing it by the time-averaged bowshock velocity at the tip of the bowshock. Several different methods have commonly been used for estimating this average velocity. In general, observations are typically only carried out at one particular point in time thereby making it impossible to obtain the time-averaged velocities required above and so introducing errors in the resulting estimated outflow ages. In each of the methods below a characteristic length is divided by a corresponding characteristic velocity to obtain an age estimate.

Each method utilises the CO spectra of an outflow which, as in Downes & Cabrit (2003), are observed using the NLTE emission formula of McKee et al. (1982) for the CO(2-1) line, assuming optically thin emission. In this way, CO emission spectra are constructed for various assumed viewing angles, in $1\,\mathrm{km\,s^{-1}}$ velocity bins, at each location on the plane of the sky. From these CO spectra, CO emission maps can be constructed in $1\,\mathrm{km\,s^{-1}}$ velocity intervals. These CO emission maps are then convolved with a gaussian psf that is based on the assumption of a telescope or interferometer with a FWHM of $1.5''$ and a distance to the emission source of $400\,\mathrm{pc}$. The resulting convolved CO emission maps are used to derive observed outflow mass, momentum, kinetic energy, and age in the same way as usually done by observers. Two sets of results are obtained, one set is based on the assumption that all emission is observable while the second set assumes that emission below a particular noise level, L_{noise}, is unobservable. As in Downes & Cabrit (2007) and for obvious symmetry reasons, we conduct our analysis only on a single lobe of the outflow (that tilted towards the observer). We also exclude any molecular

material originating from the jet, as in reality this contribution would depend on the atomic/molecular fraction in Class 0 jets, which is ill-known at present. For each simulation, both sets of results are then compared with the actual parameters obtained directly from the simulated outflow.

4.2.1 Global Method

One of the most commonly used ways of calculating the age and hence the thrust of molecular outflows from observations is to calculate the intensity-weighted velocity averaged over the entire flow and divide this into the overall length of the flow to infer an age:

$$t_{\rm g} = \frac{L_{\rm flow}}{< v >_{\rm flow}}, \tag{4.4}$$

where $L_{\rm flow}$ is the observed length of the outflow and

$$< v >_{\rm flow} = \frac{P_{\rm blue} + P_{\rm red}}{m_{\rm blue} + m_{\rm red}} \tag{4.5}$$

is the intensity-weighted average line-of-sight velocity. $m_{\rm blue}$ and $m_{\rm red}$ are values for the amount of mass in the blue and red shifted material, obtained from the CO emission using the following equation

$$m_{\rm blue} = C(n) \sum_{\rm pts.} \sum_{-U}^{-L} T(v)\, \Delta v, \tag{4.6}$$

$$m_{\rm red} = C(n) \sum_{\rm pts.} \sum_{U}^{L} T(v)\, \Delta v, \tag{4.7}$$

where $T(v)$ is the intensity of CO emission travelling at a particular velocity v, $\sum T(v)\, \Delta v$ is the integrated CO intensity that is observed at each location in the flow, $\sum_{\rm pts.}$ is the sum over all locations observed in the flow, $C(n)$ is an appropriate scaling constant that scales from integrated intensity to a molecular hydrogen mass density (see the appendix in Lada & Fich, 1996) and U and L are observationally determined lower and upper velocity limits. The lower velocity limit is often chosen in order to exclude ambient material from the calculations, while the upper velocity limit is a result of instrument sensitivity. $P_{\rm blue}$ and $P_{\rm red}$ are the absolute values of

the line-of-sight momentum in the blue and red shifted material, obtained from the CO emission using the following equations

$$P_{\rm blue} = C(n) \sum_{\rm pts.} \sum_{-U}^{-L} T(v) \, |v| \, \Delta v, \tag{4.8}$$

$$P_{\rm red} = C(n) \sum_{\rm pts.} \sum_{U}^{L} T(v) \, |v| \, \Delta v. \tag{4.9}$$

Consequently, the intensity-weighted average line-of-sight velocity defined in Equation (4.5) is

$$< v >_{\rm flow} = \sum_{\rm pts.} \frac{\sum_{-U}^{-L} T(v) \, |v| \, \Delta v + \sum_{L}^{U} T(v) \, |v| \, \Delta v}{\sum_{-U}^{-L} T(v) \, \Delta v + \sum_{L}^{U} T(v) \, \Delta v} \tag{4.10}$$

4.2.2 Local Method

A second "local" method introduced by Lada & Fich (1996) instead derives local age estimates or timescales along each line-of-sight by using local lengthscales and local characteristic velocities. Then a histogram of the frequency distribution of these local dynamical timescales is created. The peak of this distribution is taken as the inferred age of the outflow.

The local dynamical timescales along each line-of-sight are obtained in a similar manner to the global method above except that the lengthscale used is the projected distance from the point being sampled back to the source. The characteristic velocity that is used is also slightly different, it is the local intensity-weighted velocity derived using equation 4.10 at only one location in the flow, i.e. not summed over the entire flow. At each location in the flow, i.e. for each line-of-sight, we obtain

$$t_{\rm l} = \frac{r_{\rm proj}}{< v >_{r_{\rm proj}}} \tag{4.11}$$

where $r_{\rm proj}$ is the projected distance of that particular line-of-sight from the central source and $< v >_{r_{\rm proj}}$ is the local intensity-weighted velocity, obtained from the CO spectrum along that line-of-sight. This "local" method could be expected to be

more accurate since it uses local information and hence includes more detail about the kinematic structure of the flow in the calculations.

4.2.3 $v_{\max}$ Method

A third "$v_{\max}$" method, discussed by Lada (1985) and Cabrit & Bertout (1992) uses

$$t_{v_{\max}} = \frac{L_{\text{flow}}}{< v >_{\max}} \tag{4.12}$$

where $v_{\max}$ is the maximum radial velocity observed in CO profiles. This method would be expected to give a more accurate age estimate than the global method , since the characteristic velocity it uses will be closer to the time-averaged bowshock velocity at the tip of the bowshock, which determines the flow length.

4.2.4 Perpendicular Method

The final method is a new method which was outlined in Downes & Cabrit (2007). The authors point out that from observations of molecular outflows it is clear that a very large amount of the material in the outflow is moving rather slowly. Further evidence of this phenomenon, obtained from the simulations carried out here, is presented in Section 4.3.2. Assuming a jet-driven model for molecular outflows, the majority of this slow moving material will be found along the wings of the bowshock, and will have predominantly transverse motions. Supporting evidence for this transverse motion, from the simulations carried out, is also presented in Section 4.3.2 which describes Figure 4.4. Accepting that the majority of material in a molecular outflow can be found in the bowshock wings, one realises that any intensity-weighted average velocity, and hence mass-weighted average velocity, will be more indicative of velocities found in the bowshock wings as opposed to the time-averaged bowshock velocity at the tip of the bowshock. As a result a more appropriate lengthscale to use, to corresponds with the intensity-weighted average velocity, is the perpendicular distance from the jet axis, R_{flow}, rather than the length

sim	length	width	avg. density	min. density
Uniform	5326	420	1000	1000
Linear	6154	414	661	322
Exp-10	6833	824	307	10
Exp-1	6988	1112	262	1
Bonnor	7095	785	123	15.2

Table 4.3: The length and width of each outflow assuming the outflows are in the plane of the sky. The lengths and widths are given in grid cells or units of 10^{14} cm and correspond to the maximum distance the outflow has propagated into the ambient medium in the z and r directions respectively. Also shown are the average and minimum densties of the ambient medium calculated over the region into which each outflow has propagated.

of the outflow. The age estimate would then be calculated using

$$t_{\perp} = \frac{1}{3}\frac{R_{\rm flow}}{< v >_{\rm flow}}, \tag{4.13}$$

where $R_{\rm flow}$ is the maximum outflow radius, measured perpendicular from the jet axis. The coefficient of 1/3 is due to the bow being younger than one would calculate from its current rate of expansion and width (Masson & Chernin, 1993; Wilkin, 1996; Ostriker et al., 2001; Downes & Cabrit, 2007).

4.3 Results

We examine our five simulations at an age of $t = 1500$ years. As noted in Keegan & Downes (2005) this ensures that the system has overcome initial transients and that characteristics such as the mass-velocity relations have reached a quasi-steady state.

4.3.1 Density Plots

Density plots for each simulation are given in Figure 4.2. Each outflow has propagated a different distance into the ambient medium and those distances are shown in the first column of Table 4.3 along with the widths to which the outflows have expanded in the second column. Also shown in this table, for each simulation, are the average and minimum densities of the ambient medium over the region into which

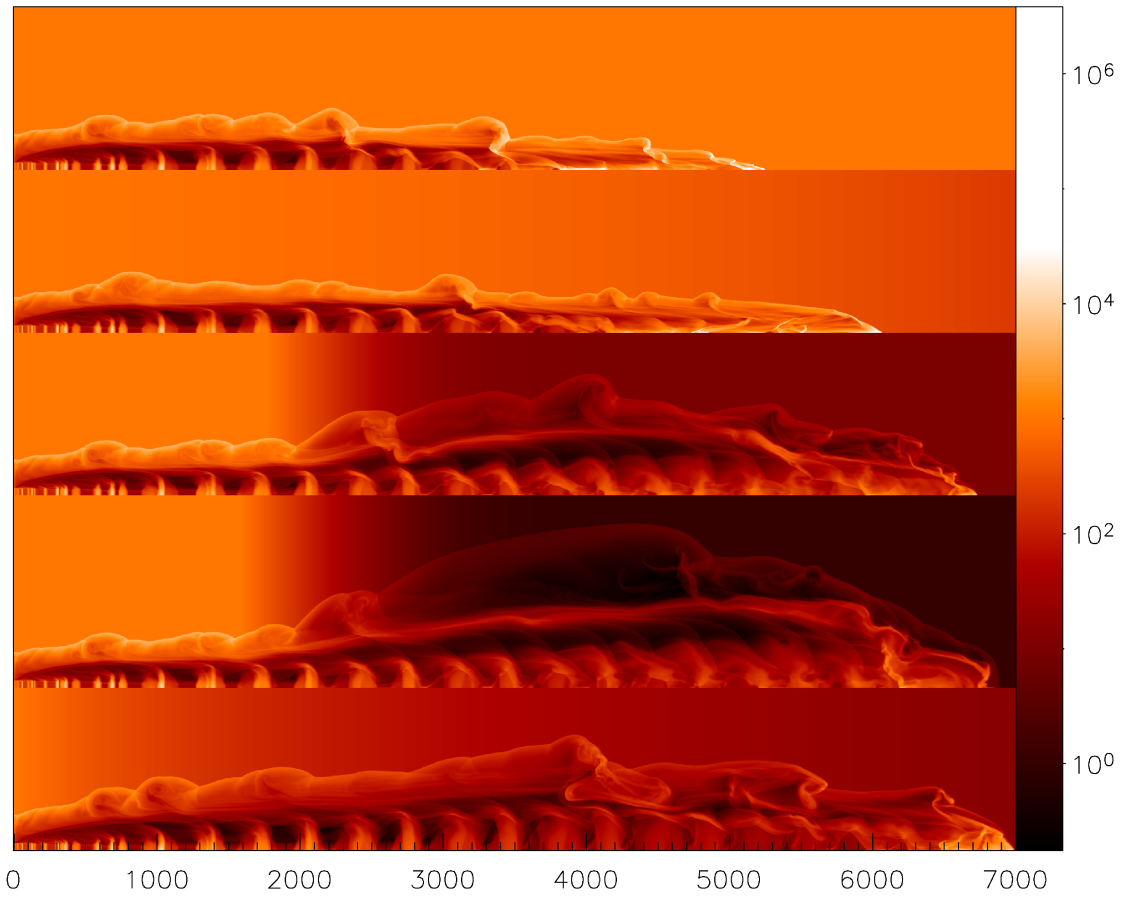

Figure 4.2: Density plots for each simulation, brighter regions indicate higher densities and vice-versa. From top to bottom the plots show the uniform, linear, exp-10, exp-1 and bonnor simulations at time $t = 1500$ years. Only the first 7100 cells in the z direction are shown in each plot since the outflows do not occupy the entire grid.

each outflow has propagated. From the density plots one notices that the simulated outflows propagating into a less dense medium have expanded in both the z and r directions by a larger amount than those propagating into a denser medium. The outflows that have propagated the longest distances are those that are propagating into the media with the lowest average densities (see column 3 of Table 4.3). This is what one would expect as the velocity of the bowshock, at the tip of an outflow, depends heavily on the density of material into which it is travelling. In the case of the exponential and bonnor simulations their expansion is quite dramatic when compared to the other simulations. Their sideways expansion can be explained by the fact that these outflows are propagating into the media with the lowest minimum densities (see column 4 of Table 4.3). When comparing these simulations, a simulation with a lower minimum ambient density will also have lower densities at the head of it's bowshock. These lower densities result in a lower amount of cooling and hence less of a reduction in temperature. Less of a reduction in temperature ultimately results in increased pressure gradients in the r direction. Material at the head of the bowshock spreads outwards at a faster rate due to this increased pressure gradient, therefore increasing the cross-sectional surface area that is ploughing into the ambient medium and giving the bowshock a blunter profile.

4.3.2 Velocity Structure

From observations it has been found, in many sources, that the velocities in a molecular outflow increase with distance from the source. In particular, Lada & Fich (1996) noted that the velocity field of an outflow is well described by a single such "Hubble" law as described in Section 1.8. Figure 4.3 shows CO emission maps for the uniform simulation in different velocity intervals. It shows that at consecutively higher velocities the majority of emission is observed to be further and further from the central source, thus confirming the "Hubble" law.

Figure 4.4 shows the normalised frequency distribution of a sample of grid cells, all taken from the 2D grid of the exp-10 simulation, that satisfy the condition that they correspond to regions in the molecular outflow. Cells with a velocity of close

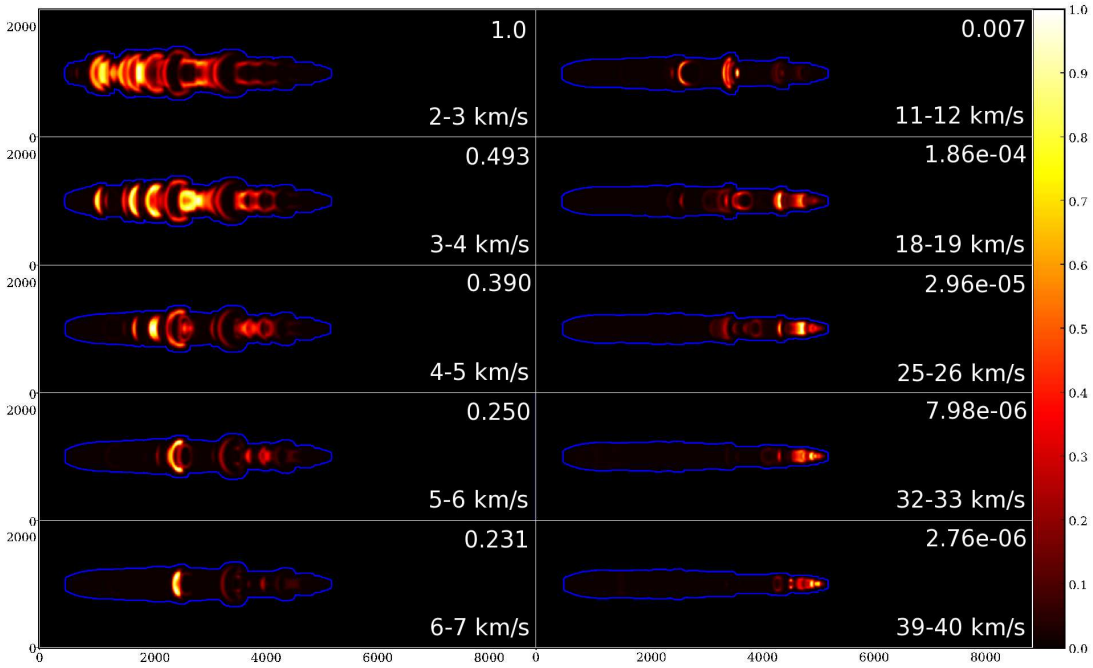

Figure 4.3: CO emission maps for the uniform simulation at time $t = 1500$ years. Each emission map shows only emission from material that is travelling with line-of-sight velocities within a particular $1\,\mathrm{km\,s^{-1}}$ interval, the range of which is given in the bottom right hand corner of each panel. The blue contours separate emitting regions from those with no emission. Each emission map is normalised by the maximum intensity in that particular map. The maximum intensity relative to the maximum intensity in the 2-3 $\mathrm{km\,s^{-1}}$ map is given in the top right hand corner of each panel.

to zero are excluded with the result that the ambient medium is not counted. Cells along the jet are also not counted by excluding those cells where 0.1% or more of the material in the cell originated as jet material, as determined via the jet tracer variable discussed in Section 2.5.1. The selected sample of grid cells is then divided into two categories, those cells in which the material is travelling with a velocity of *less* than $5\,\mathrm{km\,s^{-1}}$ are included in the top histogram while those in which the material is travelling with a velocity of *greater* than $5\,\mathrm{km\,s^{-1}}$ are included in the bottom histogram. These two samples are then subdivided with cells being assigned to one of the 18 different 5° angle bins based on the angle between the velocity vector and the jet axis. All frequencies are normalised by the overall sample size, i.e. the total number of cells that satisfied the condition that they correspond to regions in the molecular outflow. Therefore, the histograms illustrate the distribution of cells in the molecular outflow that are travelling at particular angles to the jet axis.

Examining the histograms we note that a large proportion of the cells, approxi-

mately 50%, contain material travelling at low velocities and moving perpendicular to the jet axis at an angle of 80°-90°. From examination of the data we find that this material corresponds to material in the wings of the bowshock close to its base.

Column 4 in Figure 4.4 gives the total amount of mass ($m_{\rm total}$) in the outflow while column 5 gives the line-of-sight velocity ($v_{\rm below}$) below which 90% of material is travelling. Once again jet material has been excluded from the calculations and one can see that in the uniform simulation the majority of material, 90%, is travelling with low line-of-sight velocities of below $6\,{\rm km\,s^{-1}}$.

4.3.3 Mass-Velocity Relations

Various authors have noted that the intensity-velocity relation observed in low-J CO lines in molecular outflows tends to follow a broken power-law $I_{\rm CO}(v) \propto v^{-\gamma}$, with $\gamma \approx 1.8 \pm 0.5$ up to line-of-sight velocities $v_{\rm break} \approx 10$ - $30\,{\rm km\,s^{-1}}$ and $\gamma \approx 3$ - 7 at higher velocities (e.g. Kuiper et al., 1981; Rodríguez et al., 1982; Masson & Chernin, 1993; Stahler, 1994; Lada & Fich, 1996; Richer et al., 2000). This property is an important test for proposed mechanisms of molecular outflow acceleration. More recently, similar behaviour has been observed in observations of the H_2 S(1) 1-0 line in various outflows (Salas & Cruz-González, 2002). These authors also suggested that $v_{\rm break}$ may be lower for $I_{\rm H_2}(v)$ than for $I_{\rm CO}(v)$ but it is difficult to be certain of this due to the relatively low spectral resolution of their observations ($25\,{\rm km\,s^{-1}}$). In their simulations of jet driven molecular outflows, Keegan & Downes (2005) found that the intensity-velocity relation for the CO J=2-1 line compares remarkably well with observations of molecular outflows (see also Rosen & Smith, 2004). In particular, it does have a break in slope around $10\,{\rm km\,s^{-1}}$. The break is found to result from molecular dissociation near the bow apex.

Figure 4.5 shows the CO intensity-velocity relations and the mass-velocity relations for all swept-up material in each simulation, where an angle of inclination of 30° to the plane of the sky is assumed. The relations include only swept up material. Also shown on these figures are the power-law slopes for each relation. The top panel shows the CO intensity-velocity relations which are all quite similar. One

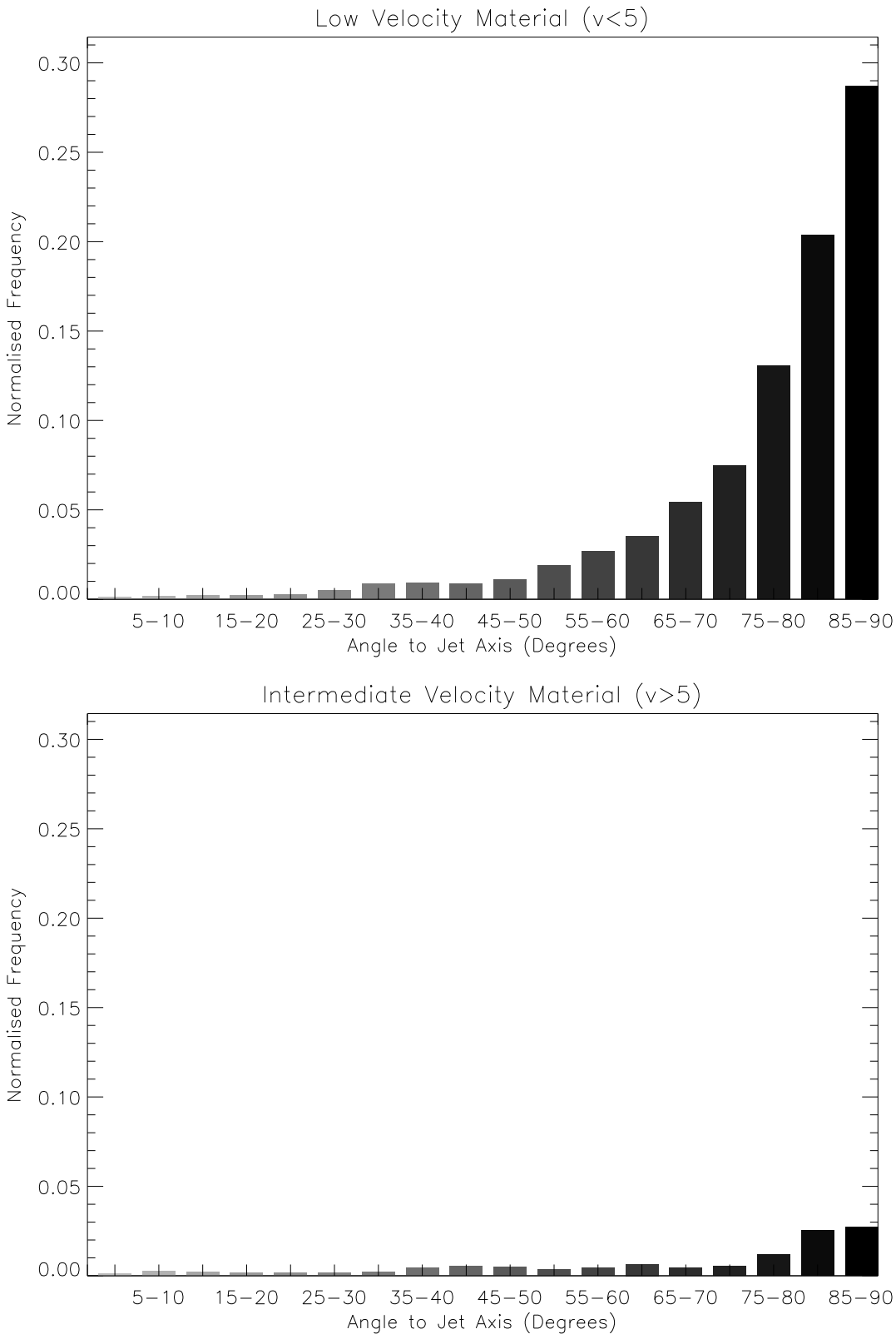

Figure 4.4: The horizontal axis in each histogram shows the angle between the velocity vector and the jet axis while the vertical axis shows the frequency which is given as the normalised number of grid points. The top histogram includes points on the grid that are travelling with a velocity of less than $5\,\mathrm{km\,s^{-1}}$ while the bottom histogram includes points with a velocity of greater than $5\,\mathrm{km\,s^{-1}}$.

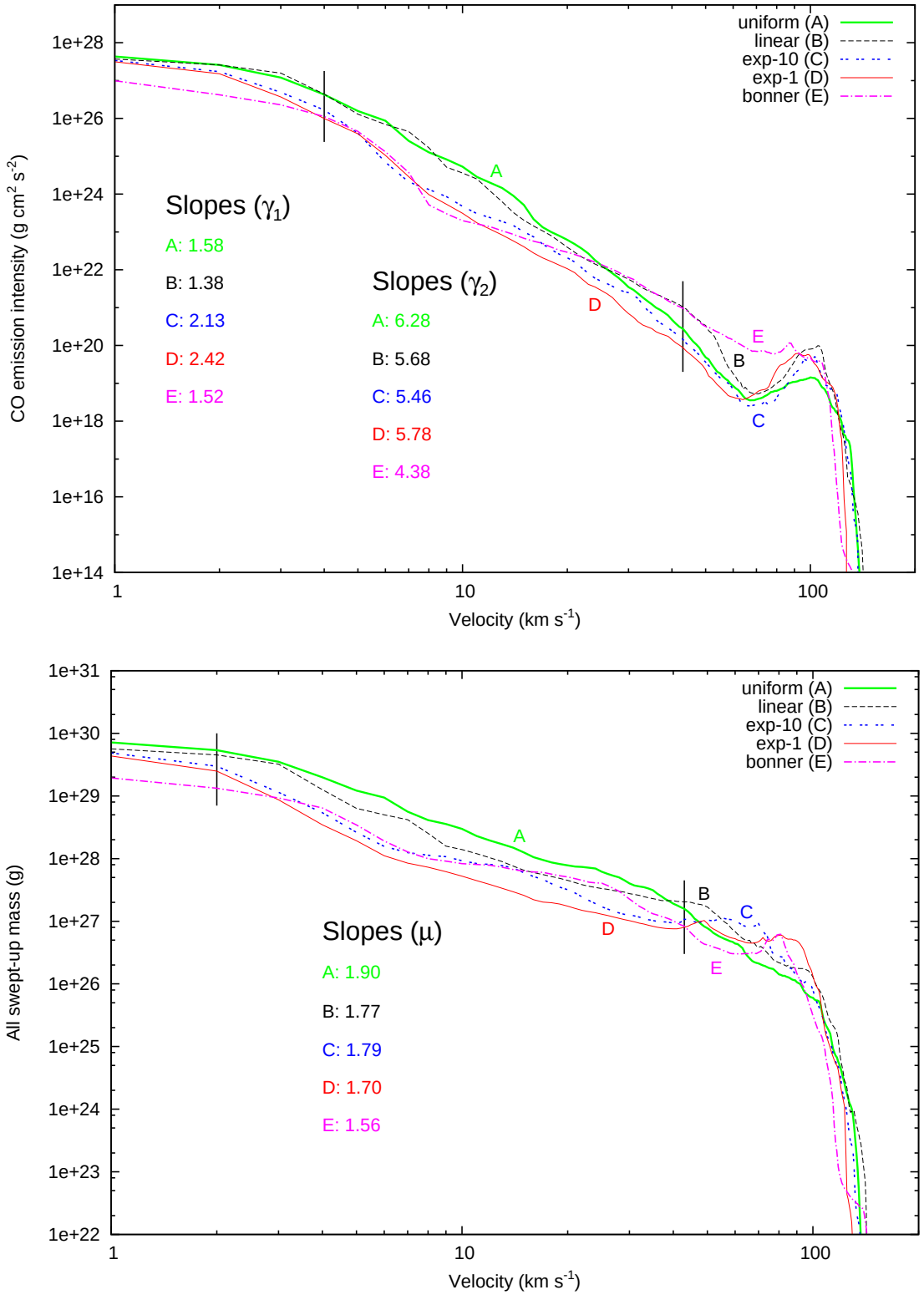

Figure 4.5: Plots of the CO intensity-velocity and mass-velocity relations for all swept-up material in each simulation. An angle of 30° to the plane of the sky is assumed. Also shown are the power-law slopes for both relations.

can see from this figure that the break in the power-law occurs at a low velocity of $v_{\rm break} \approx 4\,{\rm km\,s^{-1}}$, this is due to the use of a new cooling function as discussed in Chapter 3. The first and second columns of Table 4.4 show the power-law slopes of the CO intensity-velocity relations for material travelling slower than $v_{\rm break}$, γ_1, and faster than $v_{\rm break}$, γ_2, respectively. That is

$$\begin{aligned} I_{\rm CO}(v) &\propto v^{-\gamma_1} \quad \text{for} \quad 1 \leqslant v \leqslant v_{\rm break}, \\ I_{\rm CO}(v) &\propto v^{-\gamma_2} \quad \text{for} \quad v_{\rm break} \leqslant v \leqslant 43. \end{aligned} \tag{4.14}$$

The values in Table 4.4 are consistent with the observations mentioned above and tend to follow a broken power-law with γ within the range 1.5 - 2.4 up to line-of-sight velocities $v_{\rm break}$ and γ within the range 4 - 6 at higher velocities.

As can be seen in the bottom panel of Figure 4.5 the mass-velocity relations are surprisingly similar for each simulation. A significant feature is that $m(v)$, the mass-velocity relation for all swept up material, follows an approximate power-law $m(v) = v^{-\mu}$, with exponent μ between 1.5 and 1.9 at intermediate line-of-sight velocities. This power-law slope agrees quite well with the simple analytic bowshock model with no mixing discussed in Downes & Cabrit (2003) which predicts an exponent of the mass-velocity relation in the range $\mu = 1.5$ - 1.7. It also agrees with the simulations of jet driven molecular outflows by Keegan & Downes (2005) who found that the mass-velocity relation was a shallow power-law of exponent $\mu \simeq$ -1.6. Shown in Figure 4.5, and also in the third column of Table 4.4, is the power-law slope of the mass-velocity relation for each outflow. The slopes are calculated based on the mass and velocity of material travelling at intermediate line-of-sight velocities of between $2\,{\rm km\,s^{-1}}$ and $43\,{\rm km\,s^{-1}}$. The restricted range of μ, the slope of the power-law, would suggest that regardless of the conditions that exist in the ambient medium the slope of the mass-velocity plots for each of the outflows remains relatively constant. This, along with the overall similarity in the CO intensity-velocity and mass-velocity relations would suggest the existence of universal slopes and shapes for the relations where only small variations to these shapes are encountered due to changes in the ambient conditions.

sim	slope (μ)	slope (γ_1)	slope (γ_2)	$m_{\rm total}$ (10^{30} g)	$v_{\rm below}$	$v_{\rm g}$	$v_{\rm max}$
Uniform	1.90	1.58	6.28	5.50	6	3.05	7.5
Linear	1.77	1.38	5.68	4.40	5	3.08	8.5
Exp-10	1.79	2.13	5.46	2.96	4	2.78	6.5
Exp-1	1.70	2.42	5.78	2.47	3	2.75	6.5
Bonnor	1.56	1.52	4.38	1.65	9	3.13	7.5

Table 4.4: The power-law slope of the mass-velocity relations (μ), the two power-law slopes of the CO intensity-velocity relations (γ_2 & γ_1), the total mass of the swept up material ($m_{\rm total}$), the line-of-sight velocity in $\mathrm{km\,s^{-1}}$, below which over 90% of the mass is travelling ($v_{\rm below}$), and two characteristic velocity estimates ($v_{\rm g}$ the intensity-weighted velocity averaged over the entire flow and $v_{\rm max}$ the maximum radial velocity observed in CO profiles). These two characteristic velocity estimates are calculated based on lower and upper line-of-sight velocity limits of $2\,\mathrm{km\,s^{-1}}$ and $40\,\mathrm{km\,s^{-1}}$ respectively, as described in Section 4.2. The data for all columns is obtained by assuming a 30° angle of inclination to the plane of the sky.

4.3.4 Age and Velocity Estimates

As discussed in the introduction, an important property of a molecular outflow is the age of that outflow. Once known, the age can then be used to determine other key parameters of the system such as the momentum injection rate. Three of the standard techniques that have been popular with observers for calculating the age of an outflow, along with a fourth improved method, were outlined in Section 4.2. In each of these methods a characteristic length is divided by a corresponding characteristic velocity to obtain an age estimate.

Tables 4.5 and 4.6 show the ratio of the inferred age to the true age of the outflow using the global method, local method, $v_{\rm max}$ method and perpendicular method for each simulation, each calculated using the velocity ranges 2 – $40\,\mathrm{km\,s^{-1}}$ and 7 – $40\,\mathrm{km\,s^{-1}}$. The set of results in Table 4.5 is obtained based on the assumption that all emission is observable while the set in Table 4.6 is based on the assumption that emission below a particular noise level, $L_{\rm noise}$, is unobservable. The noise level, $L_{\rm noise}$, was assumed to be the same for all the simulations. It was set to equal the maximum level of CO emission in the convolved emission map for material travelling with line-of-sight velocities of between 35 -36 $\mathrm{km\,s^{-1}}$ in the uniform simulation and assuming an angle of 30° to the plane of the sky. This level was chosen as a result of instrument sensitivity, since emission from material travelling with line-of-sight

Sim	α	$\frac{t_g}{\text{True age}}$		$\frac{t_l}{\text{True age}}$		$\frac{t_{v_{max}}}{\text{True age}}$		$\frac{t_\perp}{\text{True age}}$	
		v_L=2	v_L=7	v_L=2	v_L=7	v_L=2	v_L=7	v_L=2	v_L=7
Uniform	0°	36.9	13.7	17.5	7.5	17.6	9.1	2.14	0.71
	30°	33.0	11.1	10.5	10.5	13.4	6.1	2.16	0.66
	60°	18.3	6.2	4.5	4.5	5.7	3.1	2.02	0.61
	90°	5.0	1.7	3.5	1.5	1.5	0.8	1.68	0.57
Linear	0°	40.6	15.3	16.5	12.5	17.5	9.1	1.95	0.66
	30°	37.6	13.8	14.5	11.5	13.6	8.0	2.06	0.67
	60°	22.8	7.3	5.5	4.5	8.1	3.4	2.10	0.60
	90°	4.9	1.6	1.5	0.5	1.8	0.7	1.65	0.53
Exp-10	0°	51.9	16.6	8.5	15.5	26.5	10.0	4.42	1.40
	30°	45.4	13.7	7.5	6.5	19.5	6.2	4.45	1.33
	60°	24.9	7.4	7.5	2.5	11.6	3.7	4.10	1.21
	90°	12.1	3.6	4.5	1.5	4.4	1.7	4.02	1.19
Exp-1	0°	53.2	17.7	6.5	8.5	26.8	10.2	5.94	1.92
	30°	43.3	13.6	3.5	3.5	18.4	7.2	5.98	1.84
	60°	25.1	7.5	6.5	4.5	11.4	3.6	5.59	1.63
	90°	15.8	4.8	7.5	2.5	5.8	2.2	5.26	1.59
Bonner	0°	46.6	17.3	8.5	13.5	20.2	9.2	3.64	1.33
	30°	42.4	14.7	10.5	5.5	17.7	7.2	3.77	1.29
	60°	27.7	6.8	10.5	3.5	12.4	2.4	4.05	0.99
	90°	12.0	2.9	3.5	1.5	5.5	1.0	4.00	0.95

Table 4.5: Ratio of the inferred age to the true age of the outflow using the global method, local method, $v_{\max}$ method and perpendicular method for each simulation, each calculated using the velocity ranges 2 – 40 $\mathrm{km\,s^{-1}}$ and 7 – 40 $\mathrm{km\,s^{-1}}$. This set of results is obtained based on the assumption that all emission is observable.

Sim	α	$t_{\rm g}$		$t_{\rm l}$		$t_{v_{\rm max}}$		$t_{\perp}$	
		True age		True age		True age		True age	
		v_L=2	v_L=7	v_L=2	v_L=7	v_L=2	v_L=7	v_L=2	v_L=7
Uniform	0°	36.0	8.0	17.5	27.5	17.1	5.3	2.14	0.68
	30°	32.5	9.8	11.5	10.5	13.2	5.4	2.16	0.63
	60°	18.0	5.7	4.5	6.5	5.6	2.8	2.02	0.58
	90°	5.0	1.6	3.5	1.5	1.5	0.8	1.68	0.54
Linear	0°	39.6	7.9	16.5	38.5	17.1	4.7	1.95	0.64
	30°	37.0	12.2	14.5	7.5	13.4	7.0	2.06	0.66
	60°	22.3	6.8	5.5	2.5	7.9	3.1	2.10	0.58
	90°	4.9	1.6	1.5	0.5	1.8	0.7	1.65	0.52
Exp-10	0°	25.8	3.3	8.5	18.5	13.2	2.0	3.47	0.94
	30°	25.8	6.8	8.5	6.5	11.1	3.2	3.49	0.90
	60°	17.0	3.6	8.5	2.5	7.9	1.8	3.21	0.81
	90°	9.5	2.4	5.5	1.5	3.4	1.1	3.16	0.80
Exp-1	0°	21.6	2.5	9.5	16.5	10.9	1.5	3.96	1.10
	30°	21.8	5.8	8.5	6.5	9.2	3.0	3.99	1.06
	60°	15.3	4.3	8.5	3.5	6.9	2.2	3.73	0.94
	90°	10.5	2.7	3.5	2.5	3.9	1.3	3.51	0.92
Bonner	0°	41.6	9.5	8.5	26.5	18.0	5.2	3.52	1.30
	30°	38.3	13.3	11.5	20.5	16.0	7.2	3.65	1.32
	60°	26.5	7.4	11.5	2.5	11.9	3.3	3.92	1.08
	90°	11.7	2.9	3.5	1.5	5.3	1.2	3.89	0.97

Table 4.6: Ratio of the inferred age to the true age of the outflow using the global method, local method, $v_{\rm max}$ method and perpendicular method for each simulation, each calculated using the velocity ranges $2 - 40\,{\rm km\,s^{-1}}$ and $7 - 40\,{\rm km\,s^{-1}}$. This set of results is obtained based on the assumption that emission below a particular noise level, $L_{\rm noise}$, is unobservable.

velocities of above $35\,\mathrm{km\,s^{-1}}$ or $40\,\mathrm{km\,s^{-1}}$ is often very difficult to distinguish from system noise and background noise, due to its low intensity levels.

Downes & Cabrit (2007) concluded that the usual estimates of outflow dynamical ages using mass- or intensity-weighted velocities are likely to exceed the true flow age by at least an order of magnitude. This is true whether the age analysis is performed globally over the whole flow, or locally (as in Lada & Fich, 1996). They also found that the method proposed by Cabrit & Bertout (1992), which uses the maximum velocity in CO profiles as a characteristic speed, performs better, though it still tends to overestimate the age by an average factor of 2 - 8. They proposed a new perpendicular method which results in much more accurate estimates of the age of a given jet-driven outflow than any other method.

For each method, global, local, v_{max} and perpendicular methods, we obtain the average factor by which that method overestimates the true flow age using the values in Table 4.5. This is done for each method by considering only the values obtained assuming a 30° inclination to the plane of the sky, and then averaging over all five simulations, i.e 10 different values. This results in an average overestimate of the true flow,

- by a factor of 27 for the global method,
- by a factor of 8 for the local method,
- by a factor of 12 for the $\mathrm{v_{max}}$ method and
- by a little over a factor of 2 for the perpendicular method.

When these average values are compared to the results in Downes & Cabrit (2007), for a density matched simulation, they are extremely similar, with the largest differences found for the v_{max} method. Therefore, the conclusions given in the previous paragraph also apply to the simulations carried out for this work. The age estimates shown in Table 4.5 for the perpendicular method are closest to the true flow age and give consistent estimates regardless of angle of inclination. This is a particularly attractive aspect of this method since no information about the inclination of the flow to the plane of the sky is needed.

Each of the methods outlined in Section 4.2 involves the calculation of a characteristic velocity. Two of the methods use a global intensity-weighted velocity ($v_{\rm g}$), while another method uses the maximum observed radial velocity in CO profiles ($v_{\rm max}$). The values of these characteristic velocities, that were calculated for each simulated outflow, are given in columns 6 and 7 of Table 4.4. Only those values calculated assuming the outflows are inclined at an angle of 30° to the plane of the sky and using the velocity range 2 - 40 $\rm km\,s^{-1}$ are shown. From the table one sees that the global intensity-weighted velocities are almost identical in each simulation with a range of only 2.75 $\rm km\,s^{-1}$ to 3.13 $\rm km\,s^{-1}$. The reason these values are almost identical follows from the fact that the mass-velocity plots and hence the power-law slopes for each simulation are very similar (see Section 4.3.3). Following from this, one should also note that since the majority of the material in each simulation is travelling at low velocity, any intensity-weighted or mass-weighted velocity calculation will be biased towards lower velocities. This can be verified by noting that the intensity-weighted velocities in table 4.4 are all within 1 $\rm km\,s^{-1}$ of the minimum velocity of the material included in the calculations (2 $\rm km\,s^{-1}$). The same global method, limited to the velocity range 7 - 40 $\rm km\,s^{-1}$, results in intensity-weighted velocities with a range of 8.4 $\rm km\,s^{-1}$ to 9.25 $\rm km\,s^{-1}$ (i.e. within 3 $\rm km\,s^{-1}$ of the minimum velocity of the material included in the calculations). Therefore one can conclude that the global velocity method is much more dependent on the minimum velocity of the material included in the calculations than on the state of the ambient medium.

While the characteristic velocities obtained using the $v_{\rm max}$ method vary slightly more than those obtained using the global method they are still quite similar ranging from 6.5 $\rm km\,s^{-1}$ to 8.5 $\rm km\,s^{-1}$. Regardless of the conditions that exist in the ambient medium the velocity estimates calculated using the commonly used global method and the $v_{\rm max}$ method are almost identical. This tells us that the current methods of obtaining velocity estimates operate independent of the ambient conditions and are quite consistent, i.e. consistently underestimating the time-averaged bowshock velocity we would ideally like to obtain.

Comparing the ratios in Table 4.5 that were calculated using the velocity range

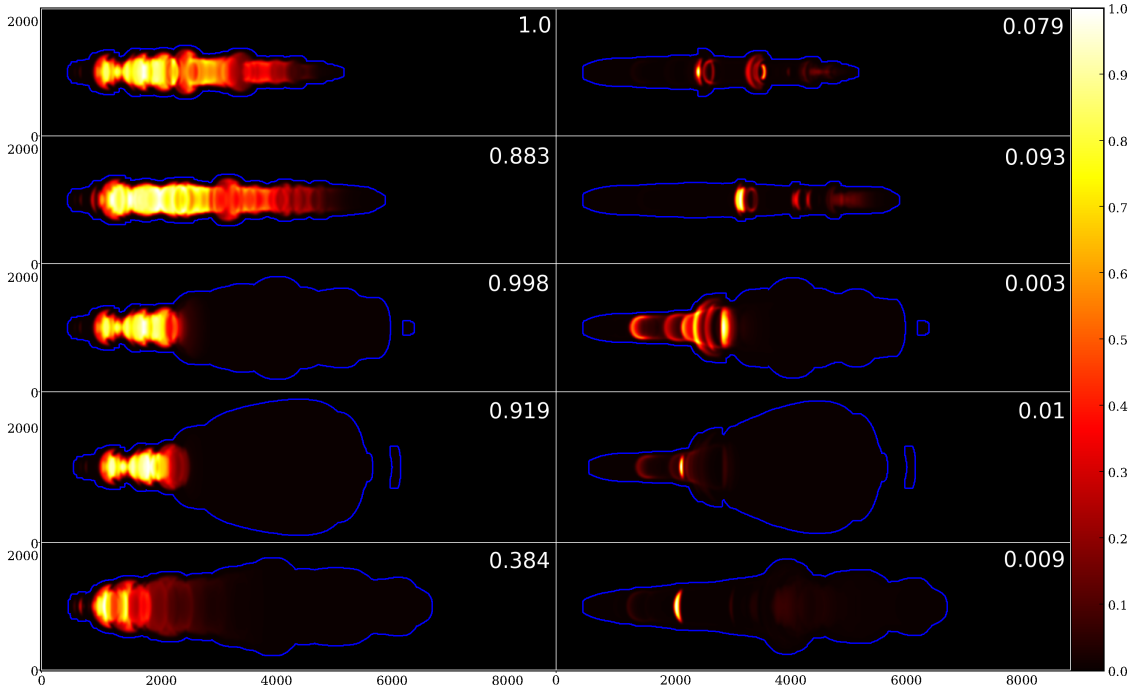

Figure 4.6: CO emission maps for each simulation. The maps on the left hand side use lower and upper velocity limits of $v_L = 2\,\mathrm{km\,s^{-1}}$ and $v_U = 40\,\mathrm{km\,s^{-1}}$ respectively, while those on the right hand side use $v_L = 7\,\mathrm{km\,s^{-1}}$ and $v_U = 40\,\mathrm{km\,s^{-1}}$. From top to bottom the plots show the uniform, linear, exp-10, exp-1 and bonnor simulations at time $t = 1500$ years. It is assumed that even regions with the lowest intensity emission are observed. The blue contours separate emitting regions from those with no emission. Each emission map is normalised by the maximum intensity in that particular map. The maximum intensity relative to the maximum intensity in the uniform (2-40 $\mathrm{km\,s^{-1}}$) map is given in the top right hand corner of each panel.

2 - 40 $\mathrm{km\,s^{-1}}$ one finds that, even though there is no large variation in the characteristic velocities that are calculated, there is still a large amount of variation in the age estimates. Looking at the variation in the range of the age estimates, considering only those values obtained assuming a 30° inclination to the plane of the sky, the range of the overestimation is a factor of 33 - 45.4 using the global method, 3.5 - 14.5 using the local method, 13.4 - 19.5 using the v_{max} method and 2.1 - 5.9 using the perpendicular method. The variation follows from the fact that in order to obtain an age estimate a characteristic length is divided by a corresponding characteristic velocity. As a result of the characteristic velocities being almost identical, the variations in the estimated ages depend more on the differences in the lengths of the simulated outflows than on their velocity differences.

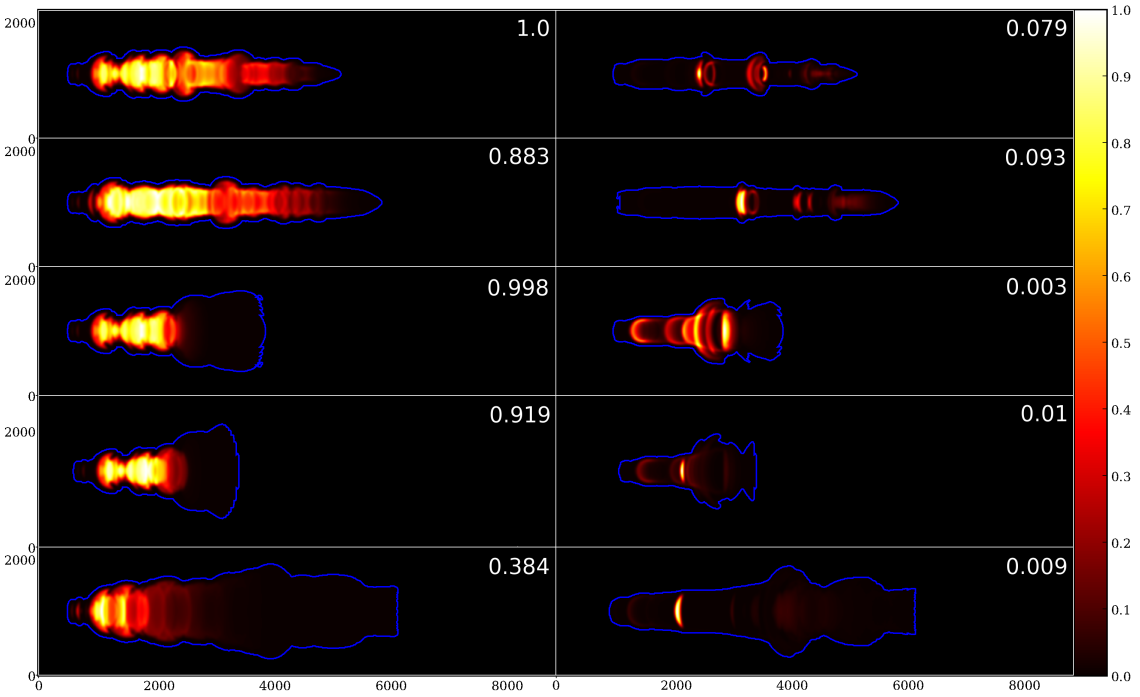

Figure 4.7: CO emission maps similar to the maps in Figure 4.6 but under the assumption that emission is unobservable if its intensity is below a particular noise level, $L_{\rm noise}$.

4.3.5 Detectable Limits

The age estimates in Table 4.5 above assume that the extent of an outflow can be accurately measured. The actual extents of the outflows obtained directly from density and temperature data are given in Table 4.3. Clearly an observer would be unable to obtain outflow extents in this manner! One method observers use to obtain the length of an outflow is to examine CO emission maps and hence determine the maximum radial distance that the outflow extends from its source. As in Section 4.2 which details how we obtain the CO emission spectra, we produce emission maps using the NLTE emission formula of McKee et al. (1982) for the CO(2-1) line, assuming optically thin emission. When creating these maps, emission is excluded if the line-of-sight velocity of the emitting material is below or above observationally determined lower and upper velocity limits. We employed two lower velocity limits, resulting in two emission maps for each simulation at a 30° inclination to the plane of the sky. As previously discussed the lower velocity limits are often chosen in order to exclude ambient material from the calculations, while the upper velocity limit is a result of instrument sensitivity.

Figure 4.6 shows CO emission maps for each simulation. The maps on the left hand side use lower and upper velocity limits of $v_L = 2\,\mathrm{km\,s^{-1}}$ and $v_U = 40\,\mathrm{km\,s^{-1}}$ respectively, while those on the right hand side use $v_L = 7\,\mathrm{km\,s^{-1}}$ and $v_U = 40\,\mathrm{km\,s^{-1}}$. In this figure it is assumed that even regions with the lowest intensity emission are observed. The blue contour separates emitting regions from those with no emission. In reality there is a certain amount of noise detected during observations, with the consequence that emission from some regions is indistinguishable from the noise. Figure 4.7 shows the CO emission map for each simulation with the same lower and upper velocity limits as in Figure 4.6 but under the assumption that emission is unobservable if its intensity is below a particular noise level, L_{noise}.

In Section 4.3.2 we noted that a large percentage of the mass in each outflow is travelling at low velocities in the bowshock wings and in a direction perpendicular to the jet. Resultingly a larger amount of emission is expected to be found in the wing regions which means that the CO emission observations are biased towards these regions. We would suspect this bias towards emission at the base of outflows to lead to an underestimate in the extent of molecular outflows, or at the very least jet-driven molecular outflows. The surprising conclusion that one reaches when comparing Figures 4.6 and 4.7 is that the exclusion of emission below a particular noise level does not result in a substantial underestimate in the outflow lengths observed for the simulations that are still propagating into a partially molecular ambient medium, i.e. the uniform, linear and bonnor simulations. On the other hand the observed outflow lengths of the outflows that have exited their parent molecular cloud and are propagating into HI and HII regions, the exp-1 and exp-10 outflows, are underestimated. So, whether or not an outflow has broken out of its molecular cloud seems to be a more important factor in the underestimation of the outflow extent than the sensitivity of the observations.

Outflow extents obtained from the convolved CO emission maps are shown in the columns of Table 4.7. The lengths in column A and C are based on the assumption that all CO emission is observable, the results were the same regardless of whether a lower velocity limit of $v_L = 2\,\mathrm{km\,s^{-1}}$ (column A) or $v_L = 7\,\mathrm{km\,s^{-1}}$ (column C) was

Sim	Length A	Length B (X_1)	Length C	Length D (X_2)
Uniform	4770	4700 (0.99)	4760	4190 (0.88)
Linear	5490	5400 (0.98)	5470	4830 (0.88)
Exp-10	5990	3400 (0.57)	5980	2920 (0.49)
Exp-1	5650	2840 (0.50)	5640	2360 (0.42)
Bonnor	6290	5680 (0.90)	6290	5260 (0.84)

Table 4.7: The extents of the outflows obtained from the convolved CO emission maps assuming a 30° inclination to the plane of the sky. The lengths in column A and C are based on the assumption that all CO emission is observable, the results were the same regardless of whether a lower velocity limit of $v_L = 2\,\mathrm{km\,s^{-1}}$ (column A) or $v_L = 7\,\mathrm{km\,s^{-1}}$ (column C) was chosen. Those in column B and D are based on the assumption that emission below a particular noise level, L_{noise}, is unobservable. Column B uses a lower velocity limit of $v_L = 2\,\mathrm{km\,s^{-1}}$ while column D uses a lower velocity limit of $v_L = 7\,\mathrm{km\,s^{-1}}$. Shown in parentheses in columns B and D, is the ratio of each length to its corresponding length in column A or C, i.e. $X_1 = B/A$ and $X_2 = D/C$.

chosen. Those in column B and D are based on the assumption that emission below a particular noise level, L_{noise}, is unobservable. Column B uses a lower velocity limit of $v_L = 2\,\mathrm{km\,s^{-1}}$ while column D uses a lower velocity limit of $v_L = 7\,\mathrm{km\,s^{-1}}$. Shown in parentheses in columns B and D, is the ratio of each length to its corresponding length in column A or C, i.e. $X_1 = B/A$ and $X_2 = D/C$. These ratios indicate the amount by which the observed lengths are reduced when emission below a particular noise level is excluded. In the two exponential simulations the observed extents are reduced by approximately a factor of 2. This is as we would expect since these outflows propagate into purely atomic material sooner, and for a much larger section of the grid, than all of the other simulations.

The age estimates corresponding to these lengths, taken from Tables 4.5 and 4.6, are repeated in Table 4.8 for the global method and in Table 4.9 for the $\mathrm{v_{max}}$ method. The fraction in parentheses indicates the amount by which the age is reduced when emission below a particular noise level is excluded, i.e. $X_1 = B/A$ and $X_2 = D/C$. Comparing these fractions to those in Table 4.7, we conclude that any reduction in the observed extent of an outflow leads to an identical reduction in its estimated age, when either the global method or the $\mathrm{v_{max}}$ method are used. Therefore, a reduction in the observed length of an outflow by a factor of 2 results in a corresponding factor of 2 reduction in the outflows' estimated age.

Sim	Age A	Age B (X_1)	Age C	Age D (X_2)
Uniform	33.0	32.5 (0.98)	11.1	9.8 (0.88)
Linear	37.6	37.0 (0.98)	13.8	12.2 (0.88)
Exp-10	45.4	25.8 (0.57)	13.7	6.8 (0.50)
Exp-1	43.3	21.8 (0.50)	13.6	5.8 (0.43)
Bonnor	42.4	38.3 (0.90)	14.7	13.3 (0.90)

Table 4.8: The age estimates for the global method corresponding to the lengths in Table 4.7. The values in columns A and C are taken from Table 4.5 while the values in columns B and D are taken from Table 4.6. The fractions in parentheses, X_1 and X_2, indicate the amount by which the age estimates are reduced when emission below a particular noise level is excluded, i.e. X_1 = Column B/Column A and X_2 = Column D/Column C.

Sim	Age A	Age B (X_1)	Age C	Age D (X_2)
Uniform	13.4	13.2 (0.99)	6.1	5.4 (0.89)
Linear	13.6	13.4 (0.99)	8.0	7.0 (0.88)
Exp-10	19.4	11.1 (0.57)	6.2	3.2 (0.52)
Exp-1	18.4	9.2 (0.50)	7.2	3.0 (0.42)
Bonnor	17.7	16.0 (0.90)	7.2	7.2 (1.00)

Table 4.9: The same as Table 4.8 above but for the v_{max} method.

On the other hand, similar reductions are *not* found for the local method since this method calculates local timescales, that are based on local lengths, at each location in the flow. The situation is also different for the perpendicular method since the only length that needs to be observed is the width of the outflow which is independent of the angle of inclination. Reductions in the estimated ages for this method are virtually non-existant for the uniform, linear and bonnor outflows and are of a smaller magnitude for the exp-1 and exp-10 outflows. The unexpected reductions in the estimated ages for the exp-1 and exp-10 outflows occur because the largest widths in these outflows are located in HI/HII regions and are therefore unobservable in molecular emission.

Extreme examples of star formation are taking place within 0.1 pc of θ Ori C, a massive star in the heart of the Trapezium cluster that lies within the Orion Nebula. According to Bally et al. (2000) over 80% of the YSOs in this region are surrounded by bright ionization fronts with radii of order 100 AU. They found 21 jets, with very small lengths ranging between 500 AU and 3000 AU, powered by young stars embedded in what the authors call proplyds. Indirect evidence suggest

Sim	Ratio A	Ratio B	Ratio C	Ratio D
Uniform	5.07	5.00	5.67	5.24
Linear	6.10	6.00	6.84	6.19
Exp-10	3.40	2.46	3.44	2.52
Exp-1	2.41	1.82	2.47	1.82
Bonnor	3.74	3.5	3.79	3.37

Table 4.10: The length-to-width ratios, corresponding to the lengths in Table 4.7, derived from the CO emission maps shown in Figures 4.6 and 4.7.

all of these proplyds contain evaporating circumstellar disks. Assuming that no molecular emission is observable in the ionised HII region outside of these proplyds, i.e outside of a radius of 100 AU, any CO observations would underestimate the lengths of these outflows by at least a factor of between 5 and 30. Hence, following on from the analysis above, the age of the outflow would also be underestimated by a factor of between 5 and 30.

Reipurth & Bally (2001) noted that parsec-scale flows have sizes about an order of magnitude larger than the typical cloud cores from which they originate. Thus, many giant flows have punched completely out of their parent molecular clouds and as a result any CO observations would underestimate the lengths of these outflows by at least an order of magnitude. Underestimates of the associated dynamical ages on a similar scale would reconcile these age estimates with the conclusions of Parker et al. (1991) who, based on a statistical approach, suggest that true outflow lifetimes are an order of magnitude larger than current dynamical ages.

4.3.6 Length-to-width Ratios

The collimation factor of CO outflows, as derived from single-dish studies, range from 3 to >20 (Arce et al., 2007). Outflow collimation and morphology is thought to change over time with the youngest outflows being highly collimated. Older outflows appear to have lower collimation factors which, it has been suggested, is due to the presence of wide-angle-winds (see Lee et al., 2001). In this section we propose an alternative explanation.

Table 4.10 gives the length-to-width ratios or collimation factors for each of the simulations, derived from the CO emission maps shown in Figures 4.6 and 4.7.

Once again, columns A and C are based on the assumption that all CO emission is observable while columns B and D are based on the assumption that emission below a particular noise level is unobservable. The length-to-width ratios shown range from 1.82 to 6.84. Therefore by simulating jets propagating into molecular clouds of decreasing density we have shown that it is possible to observe low collimation factors in the resulting *jet-driven* CO outflows. In particular, the exponential simulations have expanded sideways due to the lower densities and hence lower levels of cooling that can be found further from the centre of their molecular clouds. These lower levels of cooling result in a much larger sideways pressure gradient thus creating wider outflows. The lower level of cooling is also due to the lack of molecules in the ambient material once the outflow has exited the molecular cloud.

Also, comparing the length-to-width ratios from the CO emission maps in columns A or C with those in columns B or D, one notices that the outflows which have left the molecular cloud completely have lower collimation factors when emission below a particular noise level is considered to be unobservable. In the exp-1 simulation the collimation factor lowers from between 2.4 and 2.5 down to 1.8. This is a consequence of its length being underestimated.

An older outflow will usually be longer than a younger outflow, and therefore it will have a higher probability of breaking out of its molecular cloud. Thus, older outflows are more likely to have their lengths underestimated resulting in lower collimation factors. If the lengths of older molecular outflows are currently being systematically underestimated it would no longer be necessary to invoke the superposition of both a jet and a wide-angle-wind component, with a variation in time of the relative weight between these two components, in order to reconcile the range of the observed length-to-width ratios.

Chapter 5

Conclusions and Future Work

5.1 Conclusions

We have investigated the effect the use of various prescriptions for inhomogeneous ambient media has on simulated outflows. In particular, an analysis was carried out on the outflow mass-velocity relations and power-law slopes, outflow lengths, average velocities and inferred outflow ages. The most important conclusions are the following:

- The simulation carried out using the improved cooling function of Le Bourlot et al. (1999) resulted in less molecular cooling taking place in the jet. The outcome of less molecular cooling on the shape of the jet is an overall increase in the width of the bow shock.

- The break in the molecular mass-velocity relations occur at a much lower velocity for the simulation run using the new cooling function. The reason for this is the much higher level of dissociation that is found in this simulation as a result of the lower cooling rate and hence higher temperatures.

- Based on the assumption of an inhomogeneous ambient medium, the simulated outflows which are propagating into the lowest density ambient media display the greatest amount of sideways expansion. The sideways expansion is a consequence of the lower densities at the heads of their bowshocks. These lower densities result in lower amounts of cooling and hence increased pressure gra-

dients in the r direction. At the heads of these bowshocks, material spreads outwards at a faster rate due to the increased pressure gradients, therefore increasing the width of the outflows.

- The "Hubble" law describing the velocity field of an outflow was confirmed. We showed that at consecutively higher velocities the majority of emission is observed to be further and further from the central source.

- On average the majority of swept up material in the simulations, 90%, is travelling with low line-of-sight velocities of below $6\,\mathrm{km\,s^{-1}}$.

- Approximately 50% of the volume of the exponential ($10\,\mathrm{cm^{-3}}$) molecular outflow, contains material travelling at low velocity, less than $5\,\mathrm{km\,s^{-1}}$, and moving perpendicular to the jet axis at an angle of 80°-90°. From examination of the data this material was found to correspond to material in the wings of the bowshock close to its base.

- The values for the slopes in the CO intensity-velocity plots are consistent with observations and follow a broken power-law with γ within the range 1.5 - 2.4 for line-of-sight velocities below the break velocity and γ within the range 4 - 6 at higher velocities.

- The mass-velocity relations are strikingly similar for each simulation, suggesting the existence of a universal shape for the mass-velocity relations where only small variations to this shape are encountered due to changes in the ambient medium.

- The mass-velocity relations for all swept up material follow an approximate power-law $m(v) = v^{-\mu}$, with exponent μ between 1.5 and 1.9 at intermediate line-of-sight velocities. This power-law slope agrees quite well with the simple analytic bowshock model with no mixing discussed in Downes & Cabrit (2003) which predicts an exponent of the mass-velocity relation in the range $\mu = 1.5$ - 1.7. The restricted range in the slopes would suggest that regardless of what conditions exist in the ambient medium the slope of the mass-velocity plots

for each of the outflows remains relatively constant.

- The results of Downes & Cabrit (2007) were verified for each simulated outflow. One of their most important conclusions was that the usual estimates of outflow dynamical ages using mass or intensity-weighted velocities are likely to exceed the true flow age by an order of magnitude.

- Since the majority of the material in each simulation is travelling at low velocity, any intensity-weighted or mass-weighted velocity calculation will be biased towards lower velocities. As a result the global velocity method was found to be much more dependent on the minimum velocity of the material included in the calculations than on the state of the ambient medium.

- Regardless of the conditions that exist in the ambient medium the velocity estimates calculated using the commonly used global method and the $v_{\max}$ method are almost identical. This tells us that the current methods of obtaining velocity estimates operate independent of the ambient conditions and are quite consistent, i.e. consistently underestimating the time-averaged bowshock velocity we would ideally like to obtain.

- Since the velocity estimates calculated using the commonly used global method and the $v_{\max}$ method are almost identical, any variations in the resulting estimated ages for each outflow depend more on the variations in their observed lengths than on velocity differences.

- The exclusion of emission below a particular noise level in the emission maps of each simulation, results in a reduction in the observed extents of some of the outflows. In the two exponential simulations the observed extents are reduced by approximately a factor of 2. This is as we would expect since these outflows propagate into purely atomic material sooner, and for a much larger section of the grid, than all of the other simulations.

- Any reduction in the observed extent of an outflow leads to an identical reduction in its estimated age. This is true for each method studied with the

exception of the local method of Lada & Fich (1996). This exception stems from the fact that this method calculates local timescales, that are based on local lengths, at each location in the flow

- Reipurth & Bally (2001) noted that parsec-scale flows have sizes about an order of magnitude larger than the typical cloud cores from which they originate. Thus, many giant flows have punched completely out of their parent molecular clouds and as a result any CO observations would underestimate the lengths of these outflows by at least an order of magnitude. Underestimates of the associated dynamical ages on a similar scale would reconcile these age estimates with the conclusions of Parker et al. (1991) who, based on a statistical approach, suggest that true outflow lifetimes are an order of magnitude larger than current dynamical ages.

- Older outflows appear to have lower collimation factors which, it has been suggested, is due to the presence of wide-angle-winds (see Lee et al., 2001). An older outflow will usually be longer than a younger outflow, and therefore it will have a higher probability of breaking out of its molecular cloud. Thus, older outflows are more likely to have their lengths underestimated resulting in lower collimation factors. This alternate explanation would no longer require the invocation of the superposition of both a jet and a wide-angle-wind component, with a variation in time of the relative weight between these two components, in order to reconcile the observed collimation factors.

5.2 Future Work

As mentioned at the end of section 4.1.2, for the simulations carried out in this work, the maximum number density of the ambient medium is relatively low at $1000\,\mathrm{cm}^{-3}$. The reason for these low densities is to ensure that the shock fronts and the cooling lengths are well resolved which is an essential condition for accurate treatment of H_2 dissociation and cooling. Future proposed work will simulate higher more realistic densities using a higher resolution grid along with some lower density simulations

for comparison. The aim will be to ascertain the effects of higher densities on the properties of molecular outflows, while still resolving shock fronts and cooling lengths.

Bibliography

Ambartsumian, V. A. 1957, in IAU Symposium, Vol. 3, Non-stable stars, ed. G. H. Herbig, 177–+

Arce, H. G., Shepherd, D., Gueth, F., Lee, C.-F., Bachiller, R., Rosen, A., & Beuther, H. 2007, in Protostars and Planets V, ed. B. Reipurth, D. Jewitt, & K. Keil, 245–260

Bacciotti, F., Ray, T. P., Mundt, R., Eislöffel, J., & Solf, J. 2002, ApJ, 576, 222

Bachiller, R. 1996, ARA&A, 34, 111

Bachiller, R., & Cernicharo, J. 1990, A&A, 239, 276

Bachiller, R., & Perez Gutierrez, M. 1997, in IAU Symposium, Vol. 182, Herbig-Haro Flows and the Birth of Stars, ed. B. Reipurth & C. Bertout, 153–162

Bally, J., & Devine, D. 1994, ApJ, 428, L65

Bally, J., Licht, D., Smith, N., & Walawender, J. 2006, AJ, 131, 473

Bally, J., O'Dell, C. R., & McCaughrean, M. J. 2000, AJ, 119, 2919

Bally, J., & Reipurth, B. 2001, ApJ, 546, 299

Barral, J. F., & Canto, J. 1981, Revista Mexicana de Astronomia y Astrofisica, 5, 101

Beichman, C. A., Myers, P. C., Emerson, J. P., Harris, S., Mathieu, R., Benson, P. J., & Jennings, R. E. 1986, ApJ, 307, 337

Bence, S. J., Padman, R., Isaak, K. G., Wiedner, M. C., & Wright, G. S. 1998, MNRAS, 299, 965

Blandford, R. D., & Payne, D. G. 1982, MNRAS, 199, 883

Boehm, K. H. 1978, A&A, 64, 115

Boehm, K. H., Mannery, E., & Brugel, E. W. 1980, ApJ, 235, L137

Bohm, K.-H., Schwartz, R. D., & Siegmund, W. A. 1974, ApJ, 193, 353

Bok, B. J., & Reilly, E. F. 1947, ApJ, 105, 255

Bonnor, W. B. 1956, MNRAS, 116, 351

Boris, J. P., & Book, D. L. 1973, Journal of Computational Physics, 11, 38

Cabrit, S. 2007, in Lecture Notes in Physics, Berlin Springer Verlag, Vol. 723, Lecture Notes in Physics, Berlin Springer Verlag, ed. J. Ferreira, C. Dougados, & E. Whelan, 21–+

Cabrit, S., & Bertout, C. 1992, A&A, 261, 274

Cabrit, S., Raga, A., & Gueth, F. 1997, in IAU Symposium, Vol. 182, Herbig-Haro Flows and the Birth of Stars, ed. B. Reipurth & C. Bertout, 163–180

Canto, J., & Raga, A. C. 1991, ApJ, 372, 646

Cantó, J., Raga, A. C., & D'Alessio, P. 2000, MNRAS, 313, 656

Cardelli, J. A., Clayton, G. C., & Mathis, J. S. 1988, ApJ, 329, L33

Cernicharo, J., Lefloch, B., Cox, P., Cesarsky, D., Esteban, C., Yusef-Zadeh, F., Mendez, D. I., Acosta-Pulido, J., Lopez, R. J. G., & Heras, A. 1998, Science, 282, 462

Cernicharo, J., & Reipurth, B. 1996, ApJ, 460, L57+

Chernin, L., Masson, C., Gouveia dal Pino, E. M., & Benz, W. 1994, ApJ, 426, 204

Coppin, K. E. K., Davis, C. J., & Micono, M. 1998, MNRAS, 301, L10

Cox, D. P. 1972, ApJ, 178, 143

Crutcher, R. M., Hartkopf, W. I., & Giguere, P. T. 1978, ApJ, 226, 839

Cudworth, K. M., & Herbig, G. 1979, AJ, 84, 548

de Gouveia Dal Pino, E. M. 1999, ApJ, 526, 862

de Gouveia dal Pino, E. M., Birkinshaw, M., & Benz, W. 1996, ApJ, 460, L111+

De Young, D. S. 1986, ApJ, 307, 62

Decampli, W. M. 1981, ApJ, 244, 124

Dopita, M. A. 1978, ApJS, 37, 117

Dopita, M. A., Binette, L., & Schwartz, R. D. 1982a, ApJ, 261, 183

Dopita, M. A., Evans, I., & Schwartz, R. D. 1982b, ApJ, 263, L73

Dove, J. E., & Mandy, M. E. 1986, ApJ, 311, L93

Downes, T. P., & Cabrit, S. 2003, A&A, 403, 135

—. 2007, A&A, 471, 873

Downes, T. P., & Ray, T. P. 1999, A&A, 345, 977

Draine, B. T. 1980, ApJ, 241, 1021

Draine, B. T., Roberge, W. G., & Dalgarno, A. 1983, ApJ, 264, 485

Ebert, R. 1957, Zeitschrift fur Astrophysik, 42, 263

Elias, J. H. 1980, ApJ, 241, 728

Elmegreen, B. G. 1993, ApJ, 419, L29+

Falgarone, E., Phillips, T. G., & Walker, C. K. 1991, ApJ, 378, 186

Falle, S. A. E. G. 1991, MNRAS, 250, 581

Falle, S. A. E. G., & Raga, A. C. 1995, MNRAS, 272, 785

Favata, F., Fridlund, C. V. M., Micela, G., Sciortino, S., & Kaas, A. A. 2002, A&A, 386, 204

Godunov, S. K. 1959, Mat. Sb., 47, 271

Gomez, M., Kenyon, S. J., & Whitney, B. A. 1997, AJ, 114, 265

Gullbring, E., Hartmann, L., Briceno, C., & Calvet, N. 1998, ApJ, 492, 323

Haro, G. 1952, ApJ, 115, 572

Harten, A. 1983, Journal of Computational Physics, 49, 357

Hartigan, P., Bally, J., Reipurth, B., & Morse, J. A. 2000, Protostars and Planets IV, 841

Hartigan, P., Morse, J. A., & Raymond, J. 1994, ApJ, 436, 125

Heathcote, S., Morse, J. A., Hartigan, P., Reipurth, B., Schwartz, R. D., Bally, J., & Stone, J. M. 1996, AJ, 112, 1141

Herbig, G. H. 1951, ApJ, 113, 697

Herbig, G. H. 1969, in Non-Periodic Phenomena in Variable Stars, 75–83

—. 1973, Information Bulletin on Variable Stars, 832, 1

Herbig, G. H., & Jones, B. F. 1981, AJ, 86, 1232

Herschel, W. 1786, Philosophical Transactions Series I, 76, 457

Hollenbach, D. 1997, in IAU Symposium, Vol. 182, Herbig-Haro Flows and the Birth of Stars, ed. B. Reipurth & C. Bertout, 181–198

Hollenbach, D., & McKee, C. F. 1979, ApJS, 41, 555

Hoyle, F. 1953, ApJ, 118, 513

Jeans, J. H. 1902, Phil. Trans. R. Soc. Lond. A, 199, 1

—. 1928, Astronomy and cosmogony (Cambridge [Eng.] The University press, 1928.)

Keegan, R., & Downes, T. P. 2005, A&A, 437, 517

Kenyon, S. J., & Hartmann, L. 1995, ApJS, 101, 117

Königl, A. 1982, ApJ, 261, 115

Kuiper, T. B. H., Zuckerman, B., & Rodríguez Kuiper, E. N. 1981, ApJ, 251, 88

Lada, C. J. 1985, ARA&A, 23, 267

Lada, C. J., & Fich, M. 1996, ApJ, 459, 638

Ladd, E. F., Adams, F. C., Fuller, G. A., Myers, P. C., Casey, S., Davidson, J. A., Harper, D. A., & Padman, R. 1991, ApJ, 382, 555

Larson, R. B. 1973, ARA&A, 11, 219

—. 1981, MNRAS, 194, 809

—. 2003, Reports of Progress in Physics, 66, 1651

Le Bourlot, J., Pineau des Forêts, G., & Flower, D. R. 1999, MNRAS, 305, 802

Lee, C.-F., Mundy, L. G., Reipurth, B., Ostriker, E. C., & Stone, J. M. 2000, ApJ, 542, 925

Lee, C.-F., Stone, J. M., Ostriker, E. C., & Mundy, L. G. 2001, ApJ, 557, 429

Lepp, S., & Shull, J. M. 1983, ApJ, 270, 578

Li, Z.-Y., & Shu, F. H. 1996, ApJ, 472, 211

Liou, M.-S., & Steffen, C. J. 1993, Journal of Computational Physics, 107, 23

Lizano, S., & Giovanardi, C. 1995, ApJ, 447, 742

Lizano, S., Heiles, C., Rodríguez, L. F., Koo, B.-C., Shu, F. H., Hasegawa, T., Hayashi, S., & Mirabel, I. F. 1988, ApJ, 328, 763

Marti, J., Rodríguez, L. F., & Reipurth, B. 1993, ApJ, 416, 208

Masson, C. R., & Chernin, L. M. 1993, ApJ, 414, 230

McGroarty, F., Ray, T. P., & Bally, J. 2004, A&A, 415, 189

McKee, C. F., & Hollenbach, D. J. 1980, ARA&A, 18, 219

McKee, C. F., Storey, J. W. V., Watson, D. M., & Green, S. 1982, ApJ, 259, 647

Meyers-Rice, B. A., & Lada, C. J. 1991, ApJ, 368, 445

Micono, M., Davis, C. J., Ray, T. P., Eisloeffel, J., & Shetrone, M. D. 1998, ApJ, 494, L227+

Moriarty-Schieven, G. H., & Snell, R. L. 1988, ApJ, 332, 364

Morse, J. A., Hartigan, P., Cecil, G., Raymond, J. C., & Heathcote, S. 1992, ApJ, 399, 231

Mundt, R., Brugel, E. W., & Buehrke, T. 1987, ApJ, 319, 275

Mundt, R., & Fried, J. W. 1983, ApJ, 274, L83

Myers, P. C., Fuller, G. A., Mathieu, R. D., Beichman, C. A., Benson, P. J., Schild, R. E., & Emerson, J. P. 1987, ApJ, 319, 340

Myers, P. C., Ho, P. T. P., Schneps, M. H., Chin, G., Pankonin, V., & Winnberg, A. 1978, ApJ, 220, 864

Norman, C., & Silk, J. 1980, ApJ, 238, 158

Ogura, K. 1995, ApJ, 450, L23+

Ortolani, S., & Dodorico, S. 1980, A&A, 83, L8+

Osterbrock, D. E. 1958, PASP, 70, 399

Ostriker, E. C., Lee, C.-F., Stone, J. M., & Mundy, L. G. 2001, ApJ, 557, 443

O'Sullivan, S., & Lery, T. 2002, in Revista Mexicana de Astronomia y Astrofisica, vol. 27, Vol. 13, Revista Mexicana de Astronomia y Astrofisica Conference Series, ed. W. J. Henney, W. Steffen, L. Binette, & A. Raga, 98–102

Parker, N. D. 1991, MNRAS, 251, 63

Parker, N. D., Padman, R., & Scott, P. F. 1991, MNRAS, 252, 442

Pelletier, G., & Pudritz, R. E. 1992, ApJ, 394, 117

Pravdo, S. H., Feigelson, E. D., Garmire, G., Maeda, Y., Tsuboi, Y., & Bally, J. 2001, Nature, 413, 708

Pravdo, S. H., & Tsuboi, Y. 2005, ApJ, 626, 272

Pudritz, R. E., & Norman, C. A. 1983, ApJ, 274, 677

—. 1986, ApJ, 301, 571

Raga, A., & Cabrit, S. 1993, A&A, 278, 267

Raga, A. C. 1991, AJ, 101, 1472

Raga, A. C., Binette, L., Canto, J., & Calvet, N. 1990, ApJ, 364, 601

Raga, A. C., Canto, J., Calvet, N., Rodríguez, L. F., & Torrelles, J. M. 1993, A&A, 276, 539

Raga, A. C., Williams, D. A., & Lim, A. J. 2005, Revista Mexicana de Astronomia y Astrofisica, 41, 137

Ray, T. P. 1987, A&A, 171, 145

Ray, T. P., Mundt, R., Dyson, J. E., Falle, S. A. E. G., & Raga, A. C. 1996, ApJ, 468, L103+

Reipurth, B., & Bally, J. 2001, ARA&A, 39, 403

Reipurth, B., Bally, J., & Devine, D. 1997a, AJ, 114, 2708

Reipurth, B., Bally, J., Fesen, R. A., & Devine, D. 1998a, Nature, 396, 343

Reipurth, B., Devine, D., & Bally, J. 1998b, AJ, 116, 1396

Reipurth, B., Hartigan, P., Heathcote, S., Morse, J. A., & Bally, J. 1997b, AJ, 114, 757

Reipurth, B., Yu, K. C., Rodríguez, L. F., Heathcote, S., & Bally, J. 1999, A&A, 352, L83

Richer, J. S., Hills, R. E., & Padman, R. 1992, MNRAS, 254, 525

Richer, J. S., Shepherd, D. S., Cabrit, S., Bachiller, R., & Churchwell, E. 2000, Protostars and Planets IV, 867

Rodríguez, L. F., Carral, P., Moran, J. M., & Ho, P. T. P. 1982, ApJ, 260, 635

Rosen, A., & Smith, M. D. 2004, A&A, 413, 593

Salas, L., & Cruz-González, I. 2002, ApJ, 572, 227

Sanders, D. B., Scoville, N. Z., & Solomon, P. M. 1985, ApJ, 289, 373

Schwartz, R. D. 1975, ApJ, 195, 631

—. 1978, ApJ, 223, 884

Shu, F., Najita, J., Ostriker, E., Wilkin, F., Ruden, S., & Lizano, S. 1994, ApJ, 429, 781

Shu, F. H., Adams, F. C., & Lizano, S. 1987, ARA&A, 25, 23

Shu, F. H., Lizano, S., Ruden, S. P., & Najita, J. 1988, ApJ, 328, L19

Shu, F. H., Ruden, S. P., Lada, C. J., & Lizano, S. 1991, ApJ, 370, L31

Smith, M. D., Khanzadyan, T., & Davis, C. J. 2003, MNRAS, 339, 524

Smith, M. D., & Mac Low, M.-M. 1997, A&A, 326, 801

Smith, M. D., Suttner, G., & Yorke, H. W. 1997, A&A, 323, 223

Snell, R. L., Loren, R. B., & Plambeck, R. L. 1980, ApJ, 239, L17

Snell, R. L., Scoville, N. Z., Sanders, D. B., & Erickson, N. R. 1984, ApJ, 284, 176

Spitzer, L. J. 1941, ApJ, 94, 232

Stahler, S. W. 1994, ApJ, 422, 616

Stanke, T., McCaughrean, M. J., & Zinnecker, H. 1998, A&A, 332, 307

Steger, J. L., & Warming, R. F. 1981, Journal of Computational Physics, 40, 263

Stone, J. M., & Norman, M. L. 1993a, ApJ, 413, 198

—. 1993b, ApJ, 413, 210

—. 1994, ApJ, 420, 237

Sutherland, R. S., Bicknell, G. V., & Dopita, M. A. 1993, ApJ, 414, 510

Sutherland, R. S., & Dopita, M. A. 1993, ApJS, 88, 253

Suttner, G., Smith, M. D., Yorke, H. W., & Zinnecker, H. 1997, A&A, 318, 595

Terebey, S., Vogel, S. N., & Myers, P. C. 1989, ApJ, 340, 472

Umebayashi, T., & Nakano, T. 1988, Progress of Theoretical Physics Supplement, 96, 151

van Leer, B. 1977, Journal of Computational Physics, 23, 276

Vogel, S. N., & Kuhi, L. V. 1981, ApJ, 245, 960

Whipple, F. L. 1946, ApJ, 104, 1

Wilkin, F. P. 1996, ApJ, 459, L31+

Williams, J. P., Blitz, L., & McKee, C. F. 2000, Protostars and Planets IV, 97

Wolf, G. A., Lada, C. J., & Bally, J. 1990, AJ, 100, 1892

Yamashita, T., Suzuki, H., Kaifu, N., Tamura, M., Mountain, C. M., & Moore, T. J. T. 1989, ApJ, 347, 894

Yirak, K., Frank, A., Cunningham, A., & Mitran, S. 2008, ApJ, 672, 996